Future Abrupt Changes in Winter Barents Sea Ice Area

Ole Rieke

June 2021

A Thesis Presented for the Degree of
Master of Science in Physical Oceanography

supervised by
Marius Årthun & Jakob Simon Dörr

Geophysical Institute
Faculty of Mathematics and Natural Sciences
University of Bergen

Future Abrupt Changes in Winter Barents Sea Ice Area

Ole Rieke

Abstract

The Barents Sea is an area of strong anthropogenic winter sea ice loss that is superimposed by pronounced internal variability on interannual to multidecadal timescales. This internal variability represents a source of large uncertainty in future climate projections in the Barents Sea. This study aims to investigate internal variability of Barents Sea ice area and its driving mechanisms in future climate simulations of the Community Earth System Model Large Ensemble under the RCP8.5 climate scenario. We find that although sea ice area is projected to decline towards ice-free conditions, internal variability remains strong until late in the 21st century. A substantial part of this variability is expressed as events of abrupt change in the sea ice cover. These internally-driven events with a duration of 5-9 years can mask or enhance the anthropogenically-forced sea ice trend and lead to substantial ice growth or ice loss. Abrupt sea ice trends are a common feature of the Barents Sea in the future until the region becomes close to ice-free. Interannual variability in general, and in form of these sub-decadal events specifically, is forced by a combination of ocean heat transport, meridional winds and ice import, with ocean heat transport as the most dominant contributor. Our analysis shows that the influence of these mechanisms remains largely unchanged throughout the simulation. Investigation of a simulation from the same model where global warming is limited to 2°C shows that both mean and variability of sea ice area in the Barents Sea can be sustained at a substantial level in the future, and that abrupt changes can continue to occur frequently and produce sea ice cover of similar extent to present day climate. This highlights that future emissions play an essential role in the further decline of the Barents Sea winter sea ice cover. The results of this thesis contribute to a better understanding of Arctic sea ice variability on different time scales, and especially on the role of internal variability which is important in order to predict future sea ice changes under anthropogenic warming.

Contents

1 Introduction

Laudrum and Holland (2020) argue that global warming will drive the Arctic Ocean towards a "New Arctic" state, with a transition in temperature, precipitation and sea ice conditions. The Arctic is the region of most intense warming on the planet, with atmospheric temperatures being 2.5°C higher than in the pre-industrial era (Overland et al., 2018). This phenomenon, called Arctic Amplification potentially has strong implications on mid-latitude and polar climate (Serreze and Barry, 2011; Cohen et al., 2020). The strong temperature increase is accompanied by a decline in sea ice thickness and extent, and currently the Arctic is loosing sea ice in all regions and all seasons (Onarheim et al., 2018), with large impacts on the climate system (Ogawa et al., 2018; Sévellec et al., 2017) and ecosystem (Arrigo and van Dijken, 2011). Although the strong summer ice loss has received most attention, strong declines occur also in winter, but have so far been confined to the outer shelf seas of the Arctic (Onarheim et al., 2018). With sea ice cover decreasing to a low level in summer, future Arctic ice loss will then be dominated by the winter season (Onarheim et al., 2018).

Future climate simulations project the strong sea ice decline to continue, lading to seasonally ice-free conditions in the Arctic as early as the middle of the 21st century (Wang and Overland, 2009; Notz and Community, 2020; Årthun et al., 2021). The timing of ice-free conditions is, however, associated with large uncertainty due to the sensitivity to future emission scenarios, but also due to internal variability (Jahn et al., 2016). Internal variability is superimposed on the externally-forced sea ice decline, enhancing it at times and masking it at others. Previous studies emphasized the importance of internal variability as a major source of uncertainty in future Arctic sea ice simulations amidst emission scenario and model uncertainty, especially in the first half of the 21st century (Swart et al., 2015; Bonan et al., 2021). Mioduszewski et al. (2019) have furthermore argued that internal variability in Arctic sea ice concentration might become more pronounced in the future. The importance of internal variability on the sea ice decline is very variable throughout the Arctic. Whereas internal variability accounts for less than 10% of the recent summer ice loss in the East Siberian Sea, it is considered responsible for more than 60% in the Kara and Barents Sea (England et al., 2019).

The Barents Sea (Figure 1) is the area of most intense winter ice loss (Onarheim and Årthun, 2017). Located between the temperate Nordic Seas and the cold Arctic Ocean, it plays an important role in the Arctic climate system that will be laid out in more detail in Section 2. Sea ice in the Barents Sea has experienced an accelerated decline in recent decades, and is on track to ice-free conditions in the second half of the 21st century (Onarheim and Årthun, 2017). A part of this decline can be related to internal variability (England et al., 2019) that is particularly strong in the Barents Sea and a major source of uncertainty in future sea ice projections (Bonan et al., 2021).

In the Arctic climate system, the Barents Sea is of particular importance as a main pathway of heat into the Arctic (Smedsrud et al., 2010) and for deep water formation (Årthun et al., 2011). Global warming could lead to significant changes in these processes. Future ice retreat could for example lead to increased heat transport through the Barents Sea into the Arctic, causing accelerated sea ice melting there (Årthun et al., 2019; Sandø et al., 2014). The Barents Sea is also an area that hosts several large oil reservoirs that captures the interest of economic stakeholders. Norwegian authorities have related the distribution of licenses for exploitation based on the location of the oil

fields and the ice edge. In order to ensure a safe and sustainable use of natural resources, an understanding of the processes influencing Barents Sea ice conditions in the future, is of high importance.

The internal variability of Arctic Sea ice conditions is affected by a large range of processes, including surface albedo, clouds, water vapour, winds and energy transport in ocean and atmosphere (Olonscheck et al., 2019). Whereas their influence adds up to around 25% of the sea ice variability, Olonscheck et al. (2019) found the largest contribution to come directly from atmospheric temperature fluctuations. In the winter season Årthun et al. (2019) found ocean heat transport to be a main contributor to future Arctic sea ice loss. This is in agreement with the influence of the Atlantic Meridional Overturning Circulation on temperature and sea ice variability that was found by several studies (Mahajan et al., 2011; Zhang, 2015) and is also more pronounced in winter than in summer. Mioduszewski et al. (2019) find thermodynamical melting and freezing to be more important for Arctic sea ice variability than dynamical processes. Many of these processes also account for a large part of sea ice variability in the Barents Sea. Previous studies showed a strong influence of ocean heat transport (Årthun et al., 2012), atmospheric circulation (Herbaut et al., 2015) and ice import (Kwok, 2009).

Holland et al. (2006) suggested that future summer sea ice decline could occur in events of abrupt reductions. These are a common feature of 21st century simulations and are mainly triggered by rapid increases in ocean heat transport and reductions in surface albedo as a result of increased open water area. Investigation of different emission scenarios suggests that the frequency of these abrupt declines can directly be reduced by reduced greenhouse gas emissions. Similar rapid declines were investigated by Auclair and Tremblay (2018) who found more than half of them linked to northward ocean heat transport anomalies through the Barents Sea Opening, the Bering Strait and the Fram Strait. They find ocean heat transport to be especially linked to sea ice decline on the continental shelves whereas ice loss over the deep basins is primarily driven by the atmosphere.

In order to predict future sea ice changes under anthropogenic warming, disentangling the effects of internal variability and external forcing is crucial. For this purpose, the analysis presented here makes use of a multi-member large ensemble that produces several trajectories of the same climate model under the same external forcing and only slightly adapted initial conditions. A split of the signal into a common part of all simulations (the ensemble mean - representing the externally forced signal) and an individual part (the ensemble spread - representing internal variability) allows for the investigation of internal variability under future conditions (Section 3.2.1; Deser et al., 2012, 2014, 2020). Large ensembles have already proven to be of high value for the analysis of Arctic sea ice variability (Auclair and Tremblay, 2018; Årthun et al., 2019; England et al., 2019).

A special focus of this thesis will be on abrupt changes on sub-decadal timescales in a similar way as they were defined by Holland et al. (2006) and Auclair and Tremblay (2018). Those events can be of particular importance for the Barents Sea, where variability is large compared to the total sea ice area and rather short events can lead to a loss of half of the ice area as observed between 2004 and 2009 (Figure 2). Trends with a duration of 5-9 years will be calculated to define abrupt changes for both ice loss and growth events, and it will be assessed how these events and their driving mecha-

nisms might change under future warming. Although many previous studies have been conducted investigating the drivers of internal variability in the Barents Sea, none has focused particularly on rapid changes under future warming. In addition, we will make use of a sea ice concentration budget that relates any change in sea ice concentration to a dynamical and a thermodynamical contribution (Holland and Kimura, 2016; Uotila et al., 2014).

To test the sensitivity of these results to the influence of anthropogenic ice decline, a 11-member ensemble simulation of the same model under a climate scenario that limits global warming to 2°C will be investigated and the results compared to the large ensemble simulation that uses an RCP8.5 emission pathway.

The remainder of this study is organised as follows: Section 2 gives an overview of the relevant processes that influence ocean climate and sea ice conditions in the Barents Sea, including internal variability and possible changes in a warming world. Section 3 contains an overview of the used datasets, model configurations and methods. Results from the study are presented in Section 4 which is followed by a discussion (Section 5) and conclusion (Section 6).

2 The Barents Sea

As the largest outer shelf sea of the Arctic Ocean, the Barents Sea plays an important role in northern polar climate. It is located between the Nordic Seas in the west, the Central Arctic Ocean in the north and the Kara Sea in the east (Figure 1), roughly limited by the Norwegian Coast, Svalbard, Franz Josef Land and Novaya Zemlya.

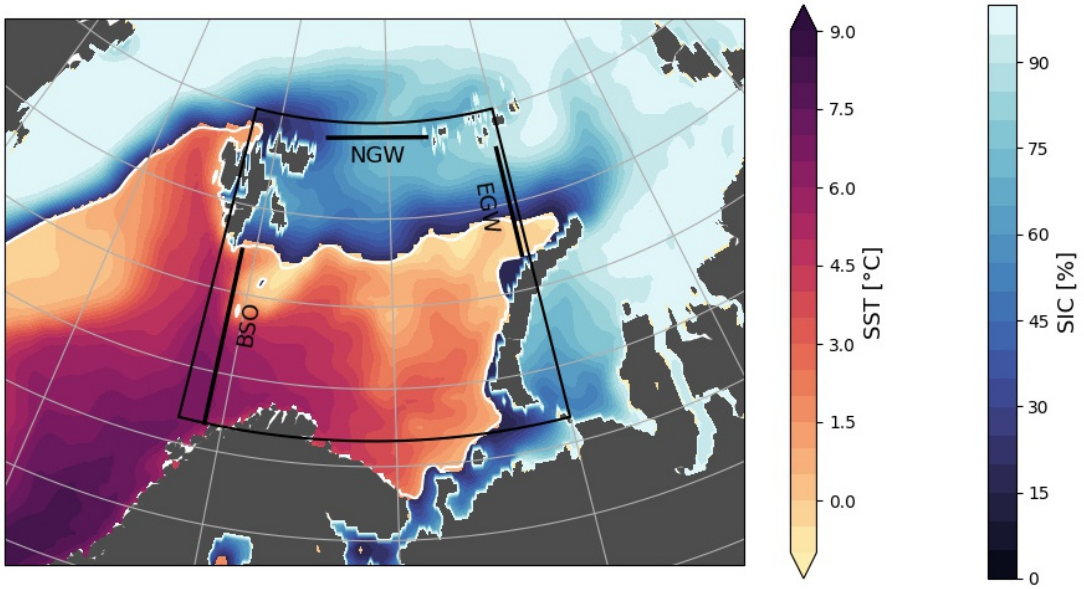

Figure 1: The Barents Sea. Blue shading indicates winter (November - April) mean sea ice concentration (SIC) from satellite observations 2013-2017, yellow-red-purple shading indicates winter sea surface temperatures from ERA-5 reanalysis data over the same time. The white line indicates the location of the 15%-SIC. The black box covers the area between 15°E-60°E, 70°N-81°N that will be used as a simplified boundary of the Barents Sea in the following analysis. The black lines indicate the main gateways of the Barents Sea: The Barents Sea Opening (BSO) in the west connects it to the Norwegian Sea, the northern gateway (NGW) leads into the Central Arctic Ocean, and the eastern gateway (EGW) into the Kara Sea.

Although only accounting for 10% of the Arctic Ocean surface area, the Barents Sea holds a key position in the Arctic climate due to its location along the main pathways of heat in atmosphere (Sorokina and Esau, 2011) and ocean (Smedsrud et al., 2010). The ocean climate in the Barents Sea is determined by strong ocean heat import and heat exchange with the atmosphere. The Norwegian Atlantic Current brings warm Atlantic Water from the south northwards along the Norwegian coast. Part of this water turns eastwards into the Barents Sea via the Barents Sea Opening (BSO) between Norway and Svalbard, bringing 2Sv (1Sv=$10^6 \frac{m^3}{s}$) of warm and salty Atlantic Water and around 70TW of heat into the Barents Sea (Smedsrud et al., 2010; Skagseth et al., 2008). A smaller inflow of submerged Atlantic Water occurs between Svalbard and Franz-Josef-Land (Lind and Ingvaldsen, 2012), but is of minor importance to the Barents Sea heat budget (less than 1TW according to Aksenov et al. (2010)). As a result of low atmospheric temperatures and strong winds in winter, the water loses all this heat to the atmosphere before exiting

into the Arctic Ocean (Gammelsrød et al., 2009). Ice production and the associated brine release result in further densification of the water. The resulting cold deep water exits through the eastern gateway and may contribute to the densest part of the North Atlantic Deep Water that overflows the Greenland-Scotland ridge (Mauritzen, 1996).

Seasonality in the Barents Sea is strong. In summer, when the atmosphere is warm, solar radiation is melting all the sea ice from the previous winter and the ocean stabilizes the atmospheric boundary layer, resulting in limited heat exchange between ocean and atmosphere (Smedsrud et al., 2013). In winter, the cold atmosphere extracts heat from the ocean. Over open water, this results in convective instability of the lower atmosphere and correspondingly strong turbulent heat fluxes. Of particular importance for this heat exchange are fractures in the thin and patchy ice cover and cold air outbreaks, when cold air from continents and ice-covered areas is advected onto open ocean, leading to intense turbulent heat loss of up to 500W/m^2 (Ivanov et al., 2003). Over ice-covered areas, the heat exchange is limited due to the insulating characteristics of sea ice. Figure 1 shows the 2013-2017 mean winter sea ice concentration and sea surface temperature in the area. In winter, the ice edge (white contour line shows a SIC of 15%) is located in the Barents Sea, the southwest being ice-free and SIC gradually increasing from the ice edge towards the eastern gateway. Sea surface temperatures (SST; yellow-red-purple shading in Figure 1) increase very quickly from freezing point at the ice edge towards 8°C along the Norwegian coast. The SST signal resembles the pathway of the inflowing Atlantic Water along Svalbard in the West Spitsbergen Current and into the Barents Sea.

Interannual and multidecadal variability are very pronounced in the Barents Sea. Observational data shows a change between warmer periods like the 1930s to 1950s, when temperatures are higher and the ice cover reduced, and cooler periods like the 1970s, with larger ice cover and colder temperatures. The variability of sea ice cover, ocean and atmospheric temperatures are clearly coupled in the Barents Sea, and also in agreement with overall Arctic variability, suggesting common forcing mechanisms (Smedsrud et al., 2013). Smedsrud et al. (2013) suggested a possible self-maintaining feedback mechanism in ocean and atmosphere that contributes to the stability of the cooler and warmer phases.

Årthun et al. (2012) found that ocean heat transport plays a major role in driving interannual variability of sea ice in the Barents Sea. A similar finding was made by Efstathiou et al. (2021) who conducted prinicipal component analysis of Barents Sea ice concentration using satellite observations in ERA-5 from 1979 onwards. The first mode of sea ice variability explaining 45% of the interannual variance that they refer to as "net-change-mode", resembles variations in total Barents Sea ice cover and shows a strong relation to ocean temperature and salinity in BSO. They also find an influence from northerly winds. The second and third mode of their analysis do not add to total sea ice area changes, but are "redistribution modes" characterised by a northwestern - southeastern dipole and a northwestern - central - southeastern tripole, respectively. These modes exhibit a relation to winds and ice import rather than ocean temperature.

Another study conducted by Herbaut et al. (2015) identifies two independently varying modes of sea ice variability with changes in the northern and eastern part of the Barents Sea, respectively. Both modes are found to be closely related to surface winds and their relation to ice import. They argue that winds also lead to a delayed response of sea ice on the wind-driven inflow of Atlantic Water. Their findings are based on the satellite

observations from 1979 to 2004 and they suggest a change in mechanisms following the rapid ice decline after 2004. Based on the retreating ice edge, they argue that the delayed impact of Atlantic Water may become less important.

Since the 1980s, winter Barents Sea ice area has experienced an intense decline from $8 * 10^5 km^2$ in 1980 to $4 * 10^5 km^2$ in 2016, that has accelerated in the last decade (Figure 2). This decline has been caused by a combination of increased ocean heat transport due to both, a strengthening of the inflow and an increase in Atlantic Water temperature (Årthun et al., 2012), and changes in atmospheric circulation and temperature (Woods and Caballero, 2016; Skagseth et al., 2020). With more heat entering through the BSO, more heat is accumulated over the year resulting in a higher heat content in autumn. The atmospheric cooling takes longer to extract this heat from the ocean, resulting in a delay of the start of the freezing season and a reduction in ice cover. Along with this retreat of sea ice goes what has recently been called "Atlantification" of the Barents Sea: Hydrographic properties of the Barents Sea become more similar to the inflowing Atlantic Water (Årthun et al., 2012).

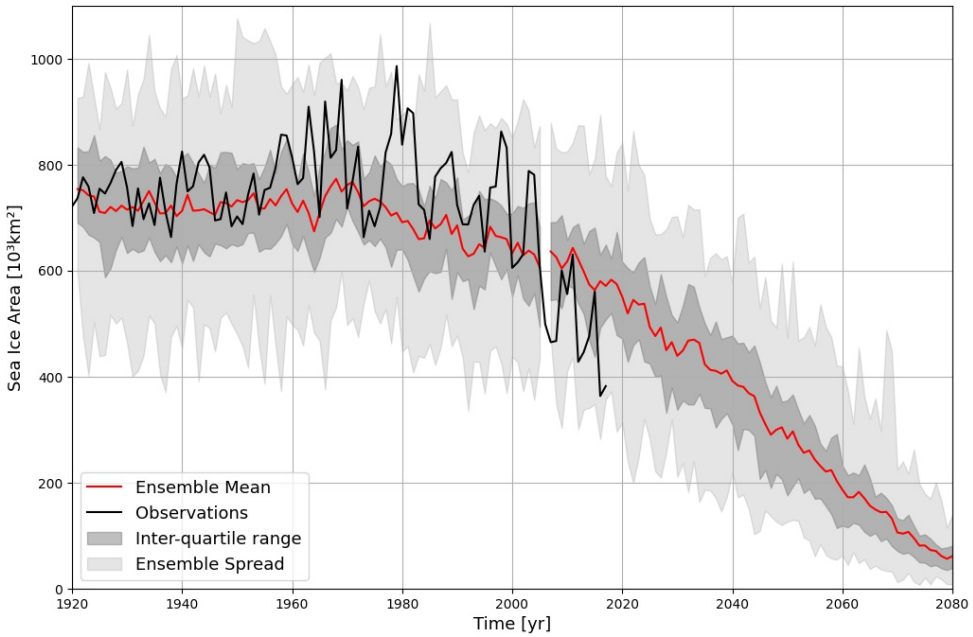

Figure 2: Winter (November-April) mean sea ice area in the Barents Sea as defined by the black box in Figure 1. The black line indicates data from the observational dataset by Walsh et al. (2017) that is based on satellite observations after 1979. The red line indicates the ensemble mean of CESM-LE historical (until 2005) and future (RCP8.5; from 2006) simulations. Grey shading represents the inter-quartile range (dark) and the ensemble spread (light).

Climate simulations project a continuation of the ongoing sea ice decline for the future (Figure 2). Under the RCP8.5 climate scenario, the Barents Sea is aiming towards year-round ice-free conditions by the end of the century (Onarheim and Årthun, 2017). This would have strong influences on the Arctic climate system by affecting atmospheric

conditions (Liptak and Strong, 2014) and opening the Central Arctic to the inflowing Atlantic Water (Årthun et al., 2019). A decreased ice cover in the Barents Sea could also influence the variability of sea ice itself. A simple conceptual model by Smedsrud et al. (2013) investigating the relative importance of atmospheric and oceanic forcing on sea ice variability found that oceanic forcing dominates when the sea ice cover is large, whereas atmospheric forcing becomes more and more important as the ice retreats.

Ice exchange between the Barents Sea and the adjacent seas is dominant by the northern gateway to the Central Arctic and the eastern gateway to the Kara Sea, both areas of large ice cover in winter (Figure 1). The Barents Sea imports large amounts of sea ice in winter, with the majority occurring via the eastern gateway (Lind et al., 2018; Kwok, 2009). This ice import peaked at $3*10^5$km^2/year in 2004, but has been declining along with the sea ice area in the Barents Sea down to under $1*10^5$km^2/year between 2011 and 2017. Ice transport across the northern gateway shows a smaller amplitude and larger variability, yet no trend, changing between ice import and ice export of less than $1*10^5$km^2/year. Lind et al. (2018) also find that the decline in ice import and the corresponding freshwater loss contribute to the recent warming hotspot that has developed in the northern Barents Sea, and might accelerate the future Atlantification of the Barents Sea.

3 Data and Methods

3.1 Data

3.1.1 Observational Data

Observational sea ice data in this study is based on the dataset provided by Walsh et al. (2017). This product contains monthly means of sea ice concentration (SIC) for the northern hemisphere on a regular grid with 0.25° horizontal resolution. Version 2 of the dataset that was used in this study, spans the time from 1850 to 2017, and has improved data coverage compared to the first version, especially in coastal areas. In consistency with the historical model simulations, only the data from 1920 onwards was used in this study. Between 1920 and 1979, the SIC data is based on several observational data sources, including ship and coastal observations that were inter- and extrapolated to the grid. With beginning of the satellite era in 1979, SIC data from remote sensing is embedded in the dataset. Due to the immensely improved data coverage from 1979, these data can be considered far more reliable.

Additionally, sea surface temperature data from the ERA-5 reanalysis product from the European Centre for Medium-Range Weather Forecasts was used (Hersbach et al., 2019). ERA-5 covers the period from 1950 onwards, but for this study, only 5 years of data between 2013 and 2017 were used to describe the current state of the Barents Sea in winter as it is shown in Figure 1.

3.1.2 Model Simulations

The main part of this study is focussing on internal variability in future climate simulations. For this purpose, future simulations under the RCP8.5 climate scenario from the Community Earth System Model Large Ensemble (CESM-LE) were used (Kay et al., 2015). Additional information on the sensitivity of these results to the climate scenario were obtained by applying a similar analysis to a smaller ensemble of future runs of the same model under a limited warming scenario. Historical simulations were used for comparison with observations and model evaluation.

Simulations are based on the Community Earth System Model Version 1 with the Community Atmosphere Model (CESM1 CAM; Hurrell et al., 2013), a fully coupled climate model of the Coupled Model Intercomparison Project Phase 5 (CMIP5; Taylor et al., 2012) and the successor of the Community Climate System Model Version 4 (CCSM4) at a horizontal resolution of approximately 1° in all model components. The atmospheric component is given by the Community Atmosphere Model Version 5 (Neale et al., 2012), run at 1° horizontal resolution on 30 vertical levels. The ocean component is the Parallel Ocean Program Version 2 (POP2; Smith et al., 2010), which is based on a curvilinear grid and 60 vertical levels of varying thickness from 10m near the surface to 250m at depth. The same grid is used by the Los Alamos Sea Ice Model (CICE4; Hunke and Lipscomb, 2008), which performs the sea ice simulations. The Community Land Model Version 4 (CLM4; Oleson et al., 2010) is used as the land component. All different components are coupled using the CPL7 (Craig et al., 2012). Whereas the atmospheric component was run on a regular latitude-longitude at a 1°-resolution, the ocean and atmosphere component are using a curvilinear grid, corresponding to a horizontal resolution of approximately 1°. The North Pole is shifted to Greenland to avoid the merging of

meridians in the ocean (Figure 3a). The grid is staggered as an Arakawa-B-grid with the tracer parameters being located in the centre of each grid cell and the velocity points located at the northeastern corner (Figure 3b). Tuning of the model was applied to adapt sea ice albedo and cloud parameters to improve the simulation of Arctic sea ice thickness and radiation balance, respectively.

The Large Ensemble experiment simulates 40 different climate trajectories over the period between 1920 and 2100 (this study uses data until 2080). A multi-member ensemble simulation offers strong advantages in the distinction of external forcing and internal variability (Section 3.2.1; Deser et al., 2012). Whereas the external forcing remains the same for all ensemble members, their differences result from slightly perturbed atmospheric initial conditions, and can hence be solely related to internal climate variability. The simulations are based on historical external forcing between 1920 and 2005 (Lamarque et al., 2010), and on future forcing following the representative concentration pathway 8.5 (RCP8.5) from 2006 onwards. All outputs from the simulations are freely available via the Earth System Grid (www.earthsystemgrid.org).

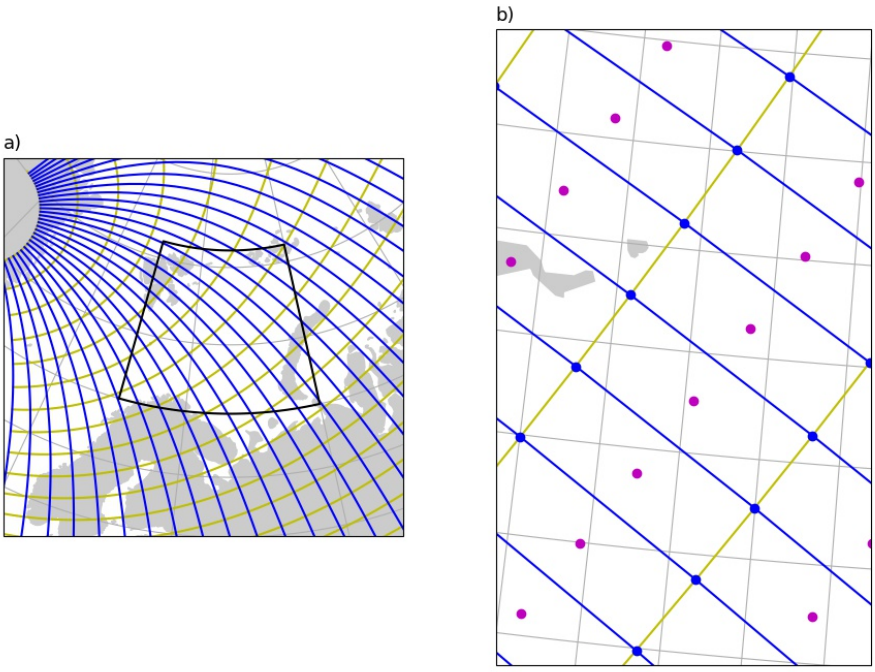

Figure 3: a) Layout of the curvilinear sea ice grid. Yellow lines indicate the x-direction of the grid and blue lines the y-direction. Every 4th grid line is shown. b) As left panel, but with every grid line shown. The magenta dots indicate the location of the tracer parameters in the centre of each grid cell, and the blue dots the location of the velocity points at the northeastern corner (in native grid direction).

This analysis is based on post-processed monthly means from the simulations. An overview of the analysed variables can be found in Table 1.

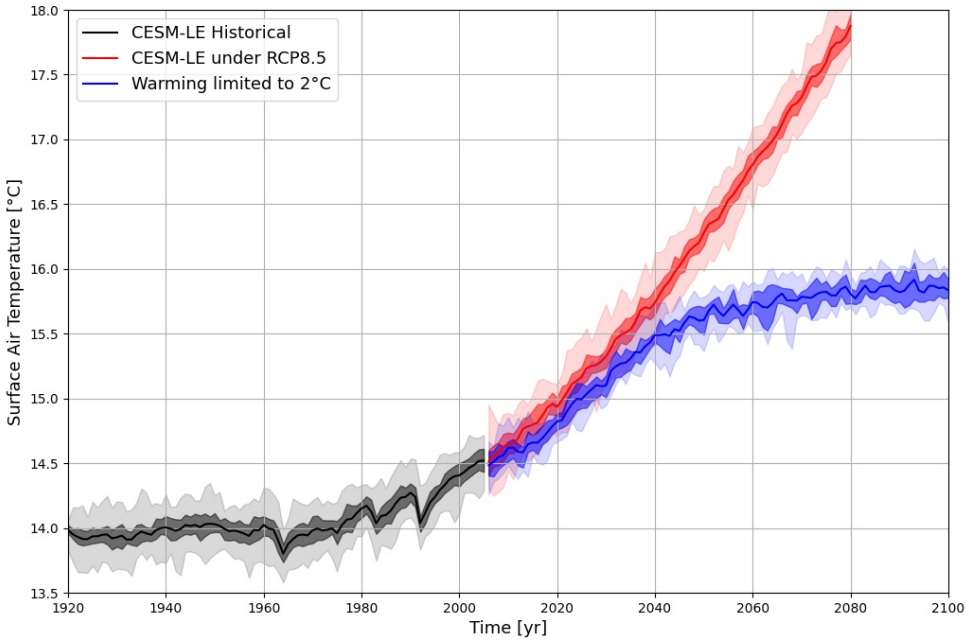

Figure 4: Global mean surface air temperature in the CESM simulations. Results for the large ensemble simulation are shown in black (historical) and red (future simulations under RCP8.5). Results from the limited warming simulations are shown in blue. The solid lines indicate the ensemble mean, the dark shading the inter-quartile range of the ensemble and the light shading the ensemble spread. Note that the amount of ensemble members differs from 40 in CESM-LE to 11 in the low warming simulations.

Another set of experiments from the Community Earth System Model was conducted using emission pathways that lead to a limitation global warming (Sanderson et al., 2017). This study uses the experiments where global warming was limited to 2°C compared to the pre-industrial level. In contrast, the global mean temperature increases to 4°C over the pre-industrial average in the CESM-LE in 2080 (Figure 4). The simulations contain 11 ensemble members from the time period of 2006-2100. Apart from the external forcing, the model setup remains the same as for the large ensemble simulations in order to enable direct comparison. From these simulations sea ice concentration, ice drift velocity and surface winds were used in the analysis.

3.2 Methods

The following chapter will contain an overview of the methods used for analysing the data described above. Since this study aims to investigate interannual variability of winter sea ice, winter means were calculated from the monthly output values. In alignment with previous studies (Årthun et al., 2012; Onarheim and Årthun, 2017), winter was hereby chosen to be represented by the months of November to April, which covers the freezing season up to the maximum ice cover which is reached in March/April. The results are not sensitive to the exact definition of winter means. The winter means are labelled with the year of January-April, meaning that winter 2007 refers to the mean of November

2006 to April 2007. Following previous studies we will define the location of the Barents Sea simplified as the area between 15°E and 60°E and 70°N and 81°N (black box in Figures 1, 3).

Variable	Codename	Grid
Sea ice concentration	aice	Curvilinear ice grid
Sea ice velocity in x-direction	uvel	Curvilinear ice grid
Sea ice velocity in y-direction	vvel	Curvilinear ice grid
Sea surface temperature	SST	Curvilinear ocean grid
Sea level pressure	PSL	Regular atmosphere grid
Meridional surface winds	VBOT	Regular atmosphere grid
Ocean heat flux in x-direction	UET	Curvilinear ocean grid
Dynamic ice concentration tendency	daidtd	Curvilinear ice grid
Thermodynamic ice concentration tendency	daidtt	Curvilinear ice grid

Table 1: Overview of the used variables from the model simulations.

A central concept for the analysis of internal variability in a multi-member ensemble simulation is the distinction of internal variability and externally-forced signal which is in detail described in Section 3.2.1. An overview of the definition and calculation of the different sea ice variables and ocean heat transport can be found in sections 3.2.2 and 3.2.3. Section 3.2.9 will describe the idea and calculation of the SIC budget The remainder of this chapter will describe the calculation of several statistical tools that were used for the analysis, including linear trends, correlation, area averaging, principal component analysis, regression and frequency analysis.

3.2.1 Separating External and Internal Variability

Multi-member ensembles are characterised by several simulations under identical forcing that only differ from small perturbations in their initial state. The results from the simulations can then be separated into a mean state that all members have in common, and a spread, that is the range of different outcomes between the members.

Here, the mean state is referred to as the ensemble mean. The ensemble mean of the simulations is simply the mean over all N simulations of any variable A:

$$\overline{A} = \frac{1}{N} \sum_{i=1}^{N} A_i \tag{1}$$

The remaining variability, that is all differences from this mean can be understood as a measure of the internal variability of the system. These deviations from the ensemble mean will be of fundamental importance in this study, as it will concentrate on internal variability in climate simulations. It is therefore convenient to define an anomaly A_a of any variable A as the deviation from the ensemble mean at any given point and time-step:

$$A_{a,i} = A_i - \overline{A} \tag{2}$$

3.2.2 Sea Ice Variables

The datasets used in this study provide sea ice concentration, which refers to the percentage of a grid cell that is covered with sea ice. Integration of the sea ice concentration C over the surface area of the domain of interest results in the sea ice area (SIA):

$$SIA = \int_A CdA \tag{3}$$

Another variable that is often used for analytical purposes is sea ice extent. In contrast to sea ice area this does not take the exact area covered by sea ice into account but rather evaluates the grid cell as a whole determining whether it is to be considered covered by sea ice or not. The usual threshold for this evaluation is a sea ice concentration of 15%. Hence, the location of the 15% SIC becomes dominant in determining the sea ice extent. The Barents Sea is rather sensitive to changes in the 15% SIC isoline and we have therefore chosen to use sea ice area instead of sea ice extent as the area-integrated value in this study.

Sea ice velocities from the model simulations were used to calculate ice transport. Ice transport IT is calculated as the product of sea ice concentration, velocity and width of a section:

$$IT = uCx \tag{4}$$

With respect to the staggered grid (Figure 3), the ice transport across a section was discretized as

$$IT = \sum_{i=1}^{d} \frac{u_{i,j} + u_{i,j-1}}{2} C_{i,j} \Delta x_{i,j} \tag{5}$$

3.2.3 Ocean Heat Transport

Ocean heat transport describes the amount of heat that is transported by the ocean current and is usually defined as the product of temperature anomaly and volume transport, multiplied by a factor of specific heat capacity and density of seawater:

$$OHT = \int_{-H}^{0} \int_{x} \rho_{sw} c_{p,sw} v (T - T_{ref}) dx dz \tag{6}$$

Here, T_{ref} describes the reference temperature of the surrounding water.

In this study, the ocean heat flux UET, given in $\frac{K}{s}$, is an output file of the model that was calculated assuming a reference temperature of 0°C which has been common practice in previous studies (Årthun et al., 2012; Smedsrud et al., 2010). Multiplication with the specific heat capacity and density, and integration over the volume of the grid cells of a section results in the desired ocean heat transport. In this case, ocean heat transport into the Barents Sea via the Barents Sea Opening was calculated as

$$OHT_{BSO} = \int_{-H}^{0} \int_{y} \rho_{sw} c_{p,sw} UET \Delta_x dy dz \tag{7}$$

3.2.4 Linear Trend

The linear trend is defined as the slope of the linear regression line that fits the data best according to a least-square-fit. The data is split into a linear relation and a residual:

$$Y = a * x + b + \epsilon \tag{8}$$

That pair of parameters a, b that fits the data Y, x in a way that minimizes the sum of squared ϵ is selected to give the best fit. a then represents the slope of the regression line and is the value of the linear trend. The resulting value of a will be in units of the ratio of the units of the two variables Y and x.

In this study, linear trends of sea ice concentration and sea ice area over time were calculated. Additionally, the linear relationship between several parameters were calculated using linear trends in Section 4.7.

3.2.5 Regression Maps

Regression maps are the result of spatial variables being related to a timeseries. The regression maps express the co-variability between each grid point and that timeseries. Assuming we have a one-dimensional time-series T of length N and a spatial dataset $\boldsymbol{X}$ of dimensions MxN where M is the spatial dimension. After the time means have been subtracted from both variables, the regression map can be calculated via simple matrix multiplication:

$$X_{reg} = \boldsymbol{X} T N^{-1} \tag{9}$$

The result is a regression map of dimension M in units of the product of both individual units. In this study, regression maps of different spatial variables on the principal component timeseries of SIC variability (see section 3.2.8) were calculated. The principal component timeseries were normalised (that is, divided by the standard deviation) prior to the calculation, resulting in regression maps that contain amplitude information in the units of the original parameters.

3.2.6 Correlation

The measure of linear correlation was used to quantify the linear relationship between two variables. The linear correlation coefficient $r_{x,y}$ of two variables x and y is defined as

$$r_{x,y} = \frac{\sigma_{x,y}}{\sigma_x \sigma_y} \tag{10}$$

with $\sigma_{x,y}$ the covariance of the variables x and y calculated as

$$\sigma_{x,y} = \frac{1}{N} \sum_{i=1}^{N} (x_i - \overline{x})(y_i - \overline{y}) \tag{11}$$

and σ_x and σ_y the individual variance of the variables x and y respectively calculated as

$$\sigma_x = \frac{1}{N} \sum_{i=1}^{N} (x_i - \overline{x})^2 \tag{12}$$

The correlation coefficient has a range of outcome between -1 and 1, where 1 indicates perfect positive correlation, -1 perfect anti-correlation and 0 no linear relationship between the variables.

3.2.7 Field Means

Field means were calculated with respect to the area of a grid cell that was represented by a value. The area-weighted field mean x_{mean} of any variable x over J gridpoints is then defined as

$$x_{mean} = \frac{\sum_{i=1}^{J} A_i x_i}{\sum_{i=1}^{J} A_i} \tag{13}$$

where x_i and A_i are the value of the variable and the area of the grid cell at gridpoint i.

3.2.8 Principal Component Analysis

Geophysical data usually consists of reoccurring spatial patterns. The principal component analysis (PCA) aims to identify those that explain the largest amount of variability by reconstructing the base of a dataset. The resulting base vectors are called empirical orthogonal functions (EOFs) and in geophysical applications the first few of them can often directly be attributed to physical mechanisms and explain most of the variability in a dataset. Together with the principal components (PCs) that describe the temporal structure of each EOF, they form a compressed representation of the dataset.

An important variable for the concept of PCA is the covariance matrix $\boldsymbol{C}$ of the data matrix $\boldsymbol{X}$. It describes the interrelation of the different spatial points over time and is defined as

$$\boldsymbol{C} = \boldsymbol{X}\boldsymbol{X}^{\boldsymbol{T}} N^{-1} \tag{14}$$

N is the length of the dataset in sampling direction. The EOFs $\boldsymbol{e}$ are given as the eigenvectors of this covariance matrix

$$\boldsymbol{C}\boldsymbol{e} = \boldsymbol{e}\lambda \tag{15}$$

with λ their corresponding eigenvalues. The original dataset can then be reconstructed from the EOFs, the eigenvalues and the principal components.

In this study we made use of the singular vector decomposition (SVD) of the covariance matrix to calculate the EOFs and PCs simultaneously. The SVD finds the structures that best represent covariance between the spatial and temporal dimension. The SVD of a matrix is defined as

$$\boldsymbol{X} = \boldsymbol{U} \sum \boldsymbol{V}^{\boldsymbol{T}} \tag{16}$$

with $\boldsymbol{U}$ and $\boldsymbol{V}$ orthogonal matrices and $\sum$ diagonal. The columns of $\boldsymbol{U}$ contain the eigenvectors of the covariance matrix $\boldsymbol{X}\boldsymbol{X}^{\boldsymbol{T}}$ which are the normalized EOFs, and $\boldsymbol{V}$ contains the eigenvectors of the covariance matrix $\boldsymbol{X}^{\boldsymbol{T}}\boldsymbol{X}$ which are the respective PCs, as columns.

In this study, PCA was performed to find the dominant patterns of sea ice concentration variability over time. In order to identify these, the dataset was transformed to be two-dimensional, with one dimension representing the pattern (space) and one representing the variability (time). The anomalies of sea ice concentration (deviation from the ensemble mean) from each member were concatenated to create a single two-dimensional matrix containing all ensemble members.

It is important to note here that the PCA is a mathematical decomposition of a matrix. It will always find dominant modes in a dataset, even if there is no physical evidence

for the existence of such a mode, and should therefore be interpreted with caution (Dommenget and Latif, 2002). To avoid the possible problem of resampling, North et al. (1982) introduced a criterion of only using those EOFs whose eigenvalues are clearly distinct from another by at least their own value. Applying this criterion usually leads to only a few EOFs representing physical modes in geophysical datasets. In this study, the produced EOFs are tested for this criterion and compared to the literature to ensure that they are indeed representing physical modes.

3.2.9 Sea Ice Concentration Budget

Any local change of sea ice concentration must be a result of mechanical redistribution or a local source/sink. This can be formulated as

$$\frac{\partial C}{\partial t} + \nabla(\mathbf{u}C) = f - r \tag{17}$$

Here, $\frac{\partial C}{\partial t}$ refers to the local change in SIC, and will hereafter be referred to as the tendency term. $\nabla(\mathbf{u}C)$ is the ice flux divergence which is the sum of advection and divergence of ice, and will be referred to as the dynamical tendency term. The residual explaining the sources and sinks of sea ice concentration is $f - r$ with f representing thermodynamical change, meaning local freezing and melting, and r representing other mechanical redistribution terms, mainly ridging, which is a sink term, where sea ice concentration is transformed to ice thickness. Following previous studies, and in particular due to the location of the domain of study in seasonally ice-covered areas, these other mechanical redistribution processes can be neglected compared to the thermodynamical term and will hence not be considered.

The CESM provides output data of dynamical and thermodynamical sea ice change. The total ice tendency is then given as the sum of both individual terms:

$$\frac{dC}{dt} = \frac{dC}{dt}_{dynamical} + \frac{dC}{dt}_{thermodynamical} \tag{18}$$

It is important to note here, that both individual ice tendency terms are not independently contributing to ice change. Instead, they are highly related, as ice formation is often related to a divergent ice flux and ice melting to a convergence of sea ice. This inverse relation is of high importance when interpreting results of the SIC budget.

3.2.10 Frequency Analysis

The frequency analysis aims to transform a dataset from time space into frequency space to obtain information about the different timescales involved and the energy that can be associated with these timescales. The analysis is based on the theorem that each timeseries $s(x)$ can be decomposed into the sum of harmonics of different frequencies:

$$s_K(x) = \sum_{k=1}^{K} (A_k cos(\frac{2\pi}{N} kx) + B_k sin(\frac{2\pi}{N} kx)) \tag{19}$$

Here, N refers to the length of the timeseries. A_k and B_k are the fourier coefficients which describe the amount of energy that is associated with the frequency $\frac{2\pi}{N}k$. The

total energy associated with that frequency is the squared sum of the coefficients $C_k^2 = A_k^2 + B_k^2$. A calculation of these coefficients results then in the power spectrum, which is the plot of C_k^2 versus k. A normalisation by the frequency results in the power spectral density. In this study, the power spectral density of the PC timeseries (Section 3.2.8) was calculated with the periodogram method, separately for each ensemble member with zero-padding to a length of 128 years, and then averaged over all members. The results are not sensitive to the method or used adjustments as calculations with the welch method (Welch, 1967) result in similar spectra.

As a comparison to the power spectrum of the dataset, a red spectrum C_r^2 was calculated. In a red spectrum, most energy is concentrated on short frequencies or longer timescales. It is defined as:

$$C_r^2 = \frac{1 - r^2}{\pi(1 + r^2 - 2rcos(r\pi f))} \tag{20}$$

Here, r represents the autocorrelation of the timeseries, which is the correlation with itself at a lag of one timestep, and f is the frequency. This red spectrum is then fitted to the calculated power spectrum as a comparison. A confidence interval is defined as two times the standard deviation of the residual between the calculated spectrum and the red spectrum.

4 Results

4.1 Barents Sea Ice Area

Sea ice area (SIA) in the Barents Sea has experienced an intensifying decline in the recent decades. The observed winter mean (November-April) sea ice area is shown in black in Figure 2. Whereas SIA remained rather constant in the first half of the 20th century, a rapid ice loss started to take place in the late 20th and the beginning of the 21st century, resulting in a minimum sea ice area of $4*10^5$km² in 2017 which is only half of the 20th century mean. Historical simulations of the Community Earth System Model Large Ensemble (CESM-LE; red in Figure 2, until 2005) are generally in good agreement with observations, simulating a consistent decline in the ensemble mean after the 1970s, although of a weaker extent than observational values. The observations are nevertheless within the ensemble spread of the simulations. Future simulations under the assumption of the RCP8.5 climate scenario project a continuation of this decline towards an entirely ice-free Barents Sea by the end of this century. Onarheim and Årthun (2017) defined the term "ice-free" by 10% of the pre-industrial SIA average, which would correspond to $8 * 10^4$km² in the Barents Sea. The ensemble mean of the CESM-LE reaches this threshold in 2075.

Strong fluctuations in the observations suggest strong internal variability, both on a year-to-year basis and on longer timescales. The ensemble spread in the simulations is comparatively large with $\pm 3 * 10^5$km², suggesting strong variability in the system. Variability decreases towards the end of the simulations when sea ice area becomes very small. Although the overall trend of SIA in the Barents Sea seems relatively constant, the strong internal variability adds on to it, leading to possible pauses in the ice decline or even ice growths at times in the individual trajectories, and very rapid ice loss at others, as it was likely the case in the previous decade (Figure 2). Understanding the internal variability on different time scales is therefore crucial to understand future developments in Barents Sea ice conditions.

The simulated ensemble mean sea ice concentration (SIC) in the Barents Sea is shown for different time periods in Figure 5. Whereas at present (panel a) only the southwest of the Barents Sea is ice-free in winter, sea ice retreats during the time of the simulations, leaving more and more of the Barents Sea open. At the end of the simulations (2067-2080), almost the entire Barents Sea is ice-free in winter (Figure 5d). The decline in SIC also includes the Central Arctic north and the Kara Sea east of the Barents Sea. Although the tendency of a retreating ice edge holds for all ensemble members, there are also large differences between the individual simulations. The magenta line indicates the southernmost location of the ice edge (defined as 15% SIC) in any individual ensemble member and year during each time period, while the green line indicates the northernmost location. The discrepancy between both is very large, and remains so during the simulation. Both the southernmost and northernmost line retreat northward, with the southwest of Svalbard being ice-free in all ensemble members after 2026. The northernmost ice edge is moving out of the Barents Sea at the end of the simulations, leaving Franz Josef Land completely ice-free for that ensemble member in 2074 (Figure 5d). Still, as the magenta lines in the bottom panels indicate, ice conditions similar to the 2007-2026 mean state occur in individual members also in the second half of the simulations (panel c and d).

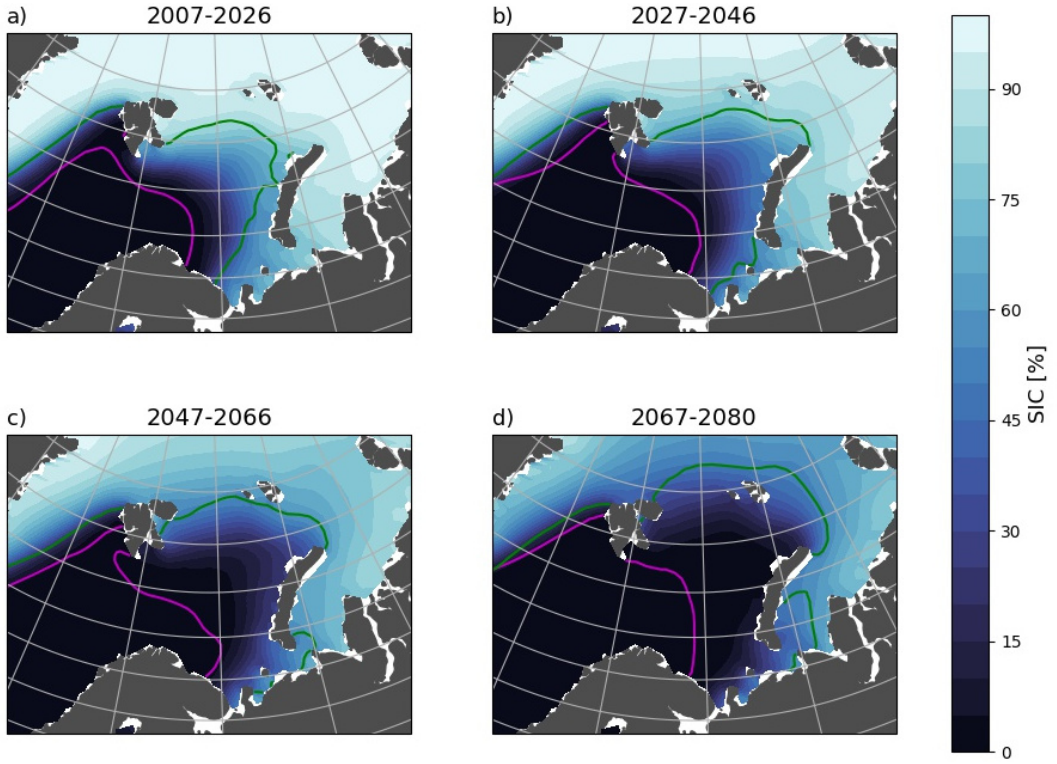

Figure 5: Winter ensemble mean sea ice concentration (shading) for different time periods of the future simulations of the CESM-LE. The coloured lines indicate the ice edge (defined as 15% SIC) of the individual ensemble member and year with the maximum (magenta) and minimum (green) sea ice area in the respective time window. The southernmost ice edge (magenta) is found in ensemble member 30 in 2016 (a), member 6 in 2032 (b), member 28 in 2051 (c) and member 14 in 2068 (d). The northernmost ice edge (green) is found in ensemble member 27 in 2022 (a), member 12 in 2044 (b), member 17 in 2065 (c) and member 20 in 2074 (d)

4.2 Interannual Variability

In order to analyse internal variability it is convenient to split the output of the individual members of the model simulations into a common part (the ensemble mean) that represents the response to external forcing and an individual part (the ensemble spread) representing internal variability, following the suggestion of Deser et al. (2012). These deviations from the ensemble mean will be referred to as anomalies, and they will be used primarily in this study (Section 3.2.1).

A powerful tool to find reoccurring patterns of variability in anomaly data is the principal component analysis (PCA; Section 3.2.8). By reconstructing a dataset, this method finds the patterns that represent the largest amount of variability in the dataset, the so-called empirical orthogonal functions (EOFs). Figure 6 shows the first 3 EOFs of Barents Sea SIC anomalies of the future simulations. Results are similar to what Efstathiou et al. (2021) find in observations. The first EOF explains 58% of the variance and represents a net-change in sea ice in the entire Barents Sea. This mode is correlated at -0.99 to Barents Sea ice area anomalies (anti-correlation because the EOF shows the negative phase, related to low sea ice conditions in the Barents Sea) and therefore well suited to

investigate net changes in the area. The net-change-mode is centred in the northeastern Barents Sea and covers the entire ice-covered area.

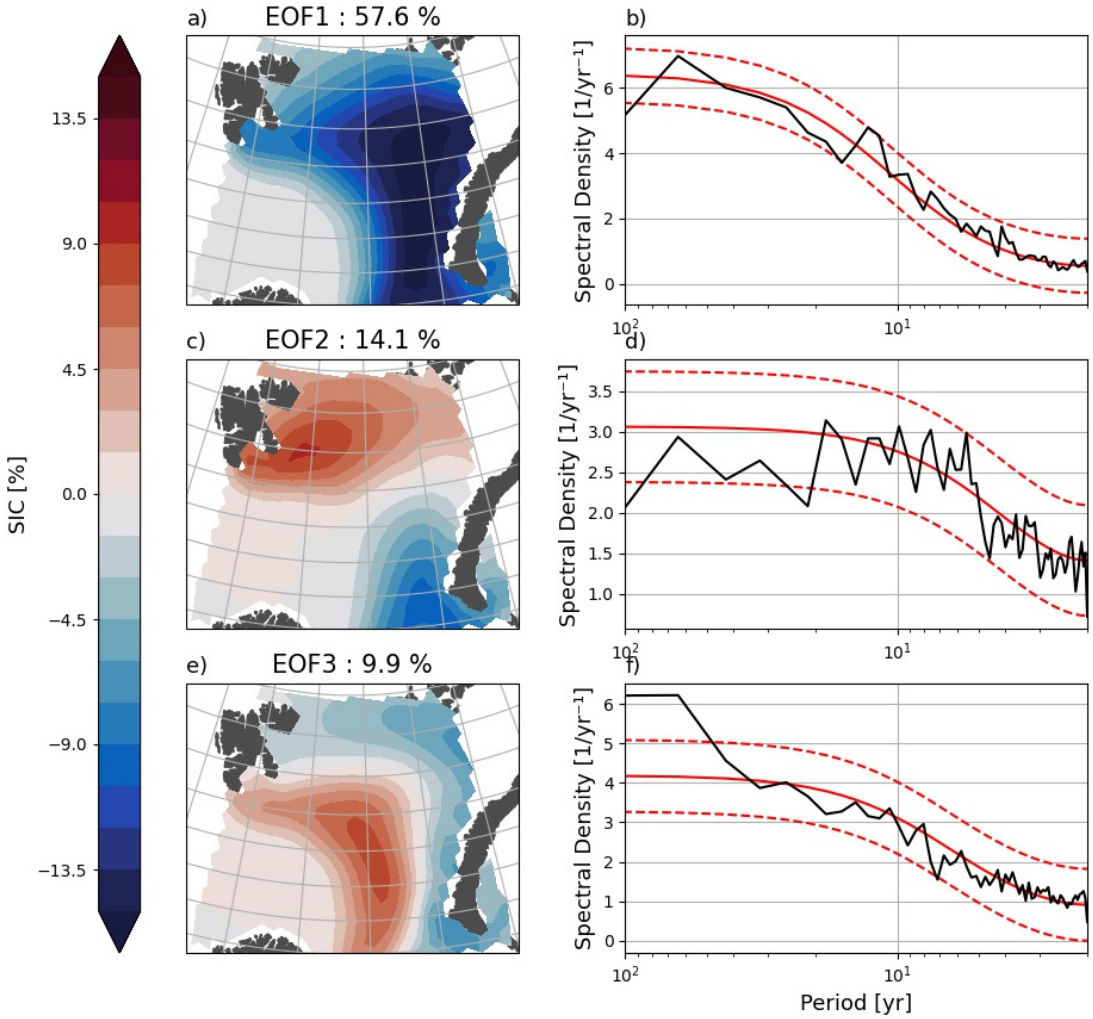

Figure 6: a),c),e): Spatial patterns of the first 3 EOFs of interannual variability of sea ice concentration in the Barents Sea. The numbers in the title represent the amount of interannual variance that is explained by each mode. b),d),f): The black lines indicate the power spectra of the principal component timeseries of these modes. The solid red lines indicate a perfectly red spectrum of the respective variability, and the dashed lines the 2-σ confidence interval around it.

The second and third mode represent what Efstathiou et al. (2021) referred to as "redistribution modes" that shift the location of the sea ice within the Barents Sea. They do not have a strong impact on net area changes over the entire domain, being correlated at 0.08 and 0.03 to Barents Sea ice area anomalies, but can represent local production and movement of sea ice. The second EOF (explaining 14% of the variance) shows a northwest - southeast redistribution, with ice production east of Svalbard and ice loss off the coast of Novaya Zemlya in its positive phase, and compares well to EOF2 of the observations (Efstathiou et al., 2021). The third mode (10% variance) shows a northeast - southwest redistribution, with the main centre of action in the central Barents Sea near the location of the ice edge. This is a little different from the redistribution-tripole that Efstathiou et al. (2021) found in EOF3, but the centre of action remains the same.

The panels on the right show the power spectra of the respective principal component timeseries associated with the EOFs. The first EOF that represents a net-change in sea ice shows a red spectrum, with more energy at longer timescales. An intensification is visible at a period of around 10-15 years that is significantly different from the red spectrum. This corresponds to a growing / decreasing branch of 5-8 years duration. This duration coincides with the length of the abrupt ice loss after 2004 visible in observations and the rapid ice declines that Holland et al. (2006) and Auclair and Tremblay (2018) find in future simulations of Arctic sea ice. The second mode has little energy at short timescales, but most energy is concentrated at periods of 5-20 years. Towards even longer timescales power decreases again. The third mode shows a red spectrum with an intensification at long timescales.

4.3 Drivers of Interannual Variability

Located between the Arctic Ocean and the temperate Nordic Seas, the Barents Sea is affected by many climate processes that possibly influence sea ice conditions. Many previous studies emphasize the strong influence of ocean heat transport (OHT; Årthun et al., 2012; Schlichtholz, 2011) and sea surface temperatures (SST; Efstathiou et al., 2021) in the Barents Sea Opening (BSO) on the sea ice, whereas other studies find wind (Herbaut et al., 2015; Nakanowatari et al., 2014) or ice import (Kwok, 2009) to be important. This section will hence investigate the influence that the different forcing mechanisms have on sea ice variability.

Figure 7 shows the regression of sea ice concentration, sea surface temperature and sea level pressure (SLP) anomalies on the PC timeseries of the EOFs in Figure 6. The panels on the left show the regression for the most dominant mode of interannual variability (EOF 1). The regression of sea ice concentration shows that the modes also reflect variability outside the boundaries of the Barents Sea. The signal related to the net-change-mode (panel a) extends into the Kara Sea and Nordic Seas, with a reversed signal near the southern tip of Greenland. There is no signal visible in the rest of the Arctic.

Regression of SST (panel d) indicates that low ice area in the Barents Sea is related to strong positive SST anomalies in the entire Barents Sea, but also in the Kara Sea. To the west, the signal extends through the Barents Sea Opening into the Nordic Seas, along the pathway of the inflowing Atlantic Water. This suggests that a large part of these SST anomalies and hence the sea ice conditions can be related to ocean heat transport through Barents Sea Opening, as already established in previous studies (Smedsrud et al., 2010; Årthun et al., 2012). The pattern also shows a negative SST anomaly between Iceland and Greenland and in the northern Labrador Sea, where the SIC response was reversed compared to the Barents Sea, but the amplitude is clearly reduced compared to the signal in the Barents Sea.

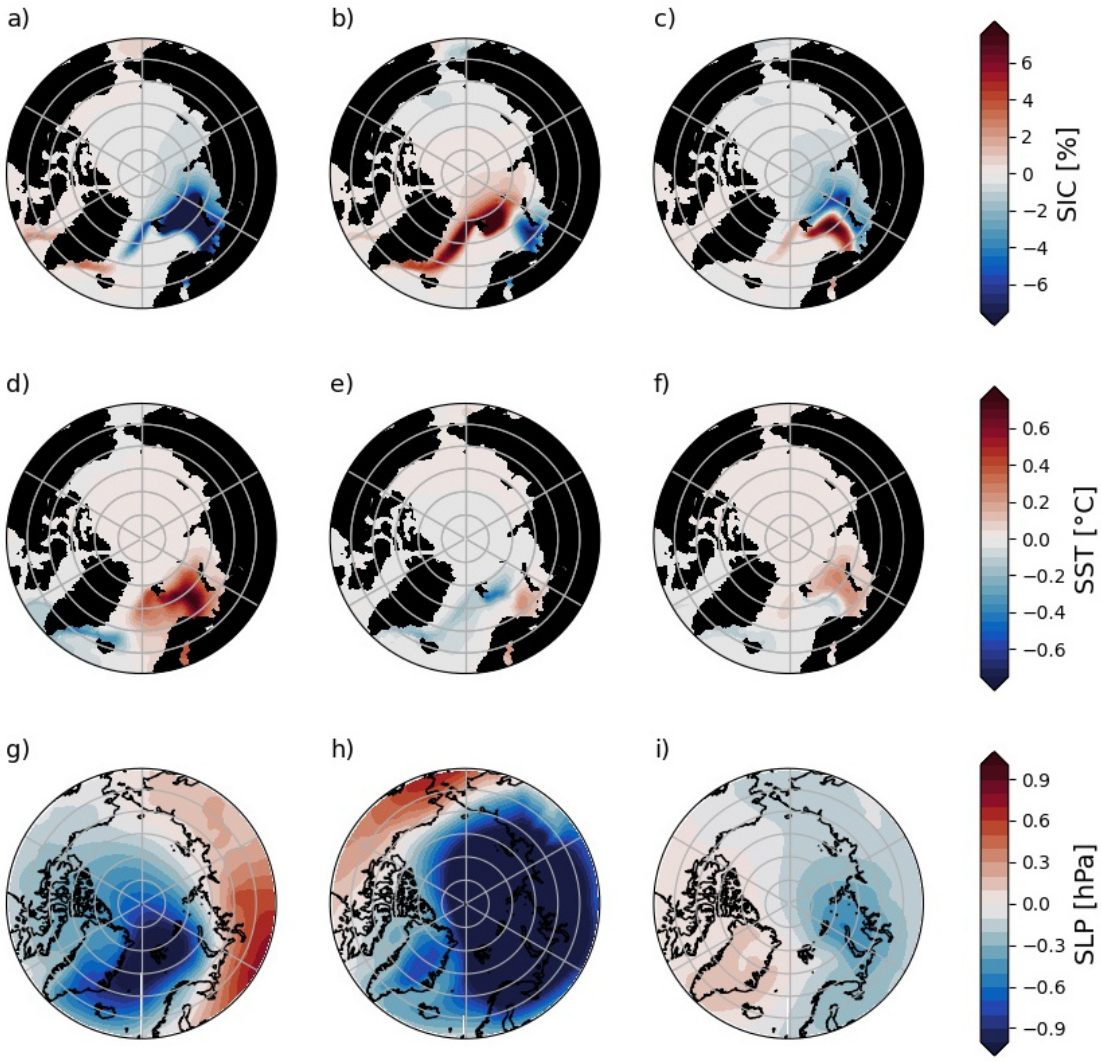

Figure 7: Regression of sea ice concentration (top), sea surface temperature (middle) and sea level pressure (bottom) anomalies on the PC timeseries of the first 3 EOFs (from left to right). The pattern shows conditions that are related to the same phase of the EOF that is shown in Figure 6. For the first EOF (left column) this means conditions that are related to small ice cover.

The pattern of sea level pressure (panel g) shows a clear dipole anomaly, with low pressure anomalies in the Nordic Seas, and the Canadian Basin of the Arctic, and high pressure anomalies over Russia during low ice conditions. This dipole pattern can directly be related to atmospheric circulation anomalies, indicating that a low ice area in the Barents Sea is related to southerly winds in the northern Barents Sea and southwesterly winds in the southern Barents Sea. In the following, this circulation anomaly will be represented by meridional winds averaged over the Barents Sea. Although the pattern indicates a more zonal component in the southern Barents Sea, area-averaged meridional winds over the full domain in Figure 1 show the highest correlation to sea ice area anomalies and serve therefore as a good proxy for this circulation pattern.

Both redistribution modes show anomalous sea ice concentration outside of the Barents Sea. The positive anomaly of redistribution mode one (panel b) extends widely into the

Nordic Seas, whereas redistribution mode two extends more into the Kara Sea (panel c). Concerning SST the first redistribution mode is related to warm temperatures in the southeastern Barents Sea, where the spatial pattern shows ice loss, and cold temperatures in the northwest (panel e) where the EOF shows ice increase. There are also cold SST anomalies visible in the western Nordic Seas along the location of the ice edge. The sea level pressure shows a strong negative anomaly across the entire Arctic Ocean (panel h). The second redistribution mode shows a relation to warm SST in the north-eastern Barents Sea (panel f), which is in agreement to the ice loss in that area. Small negative anomalies are visible in the southwestern Barents Sea. The SLP pattern is clearly reduced in amplitude compared to the other two modes. It shows a dipole anomaly between the Kara Sea and Greenland that can be associated with northward winds during the positive phase of the pattern (panel i). The driving mechanisms of the redistribution modes, are as the modes themselves in good agreement with what Efstathiou et al. (2021) found in observational data. They will not be subject to further analysis, as this study focuses on the total Barents Sea ice area, which is sufficiently represented by the first EOF.

To further investigate the relationship between Barents Sea ice area and the different driving mechanism, 21-year running correlations are calculated for each ensemble member. The ocean forcing that is shown by the SST regression in Figure 7d) is represented by ocean heat transport through the Barents Sea Opening, and the atmospheric forcing is represented by meridional winds averaged over the Barents Sea. In addition, ice transport across the northern gateway between Svalbard and Franz Josef Land and across the eastern gateway between Franz Josef Land and Novaya Zemlya will be analysed.

4.3.1 Ocean Heat Transport

Warm and salty Atlantic Water is predominantly brought into the Barents Sea via the Barents Sea Opening (Smedsrud et al., 2010). This inflowing water is the main supply of heat for the Barents Sea and has been shown to impact the sea ice area (Årthun et al., 2012). To analyse the relationship between this heat transport and sea ice area in the CESM future simulations, ocean heat transport across the Barents Sea Opening (section in Figure 8a) has been calculated. Although the year-round heat transport is important for the mechanism, this investigation focuses on winter (November - April) ocean heat transport as this captures most of the interannual variability (Dörr et al., 2021). Figure 8b) shows the simulated ocean heat transport over the 21st century. Starting from around 60 TW at present, which is slightly lower than observed values of 70TW (Smedsrud et al., 2013), the ensemble mean of OHT is projected to increase steadily during the simulation period up to 90 TW in 2080. This increase is quite robust across the ensemble members, with an inter-quartile range of ± 10TW and an ensemble spread of ± 30TW in 2006 that is increasing to ± 40TW in 2080. The increase in OHT is due to an increase in temperature of the inflowing Atlantic Water, whereas the volume transport remains relatively constant (Årthun et al., 2019).

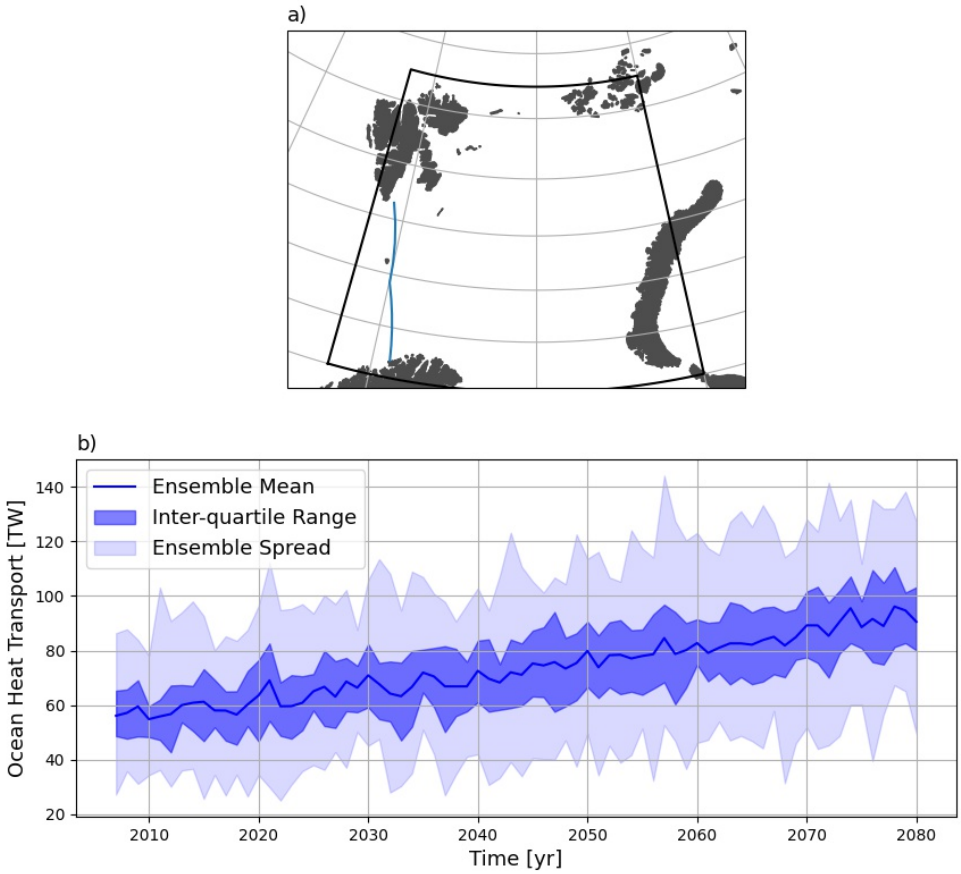

Figure 8: a): The blue line indicates the section on the native grid that represents the Barents Sea Opening. Ocean heat transport was calculated across this section. The black box indicates the extent of the Barents Sea that was used in this study. b): Timeseries of OHT through BSO during the simulation. The solid line indicates the ensemble mean, the dark shading the inter-quartile range and the light shading the ensemble spread.

Figure 9 shows the 21-year running correlation of Barents Sea ice area anomalies and OHT anomalies through BSO (blue). A clear anti-correlation of -0.7 is found that slowly, but constantly decays over time to -0.6. The inter-quartile range remains quite constant at ± 0.1. This relates to larger ocean heat transport leading to reduced ice cover and vice-versa. The anti-correlation is robust across all ensemble members. During the second half of the 21st century, the decrease in correlation can be related to the reduction of sea ice which moves the ice edge further away from the BSO. As the red line in Figure 9 indicates, OHT anomalies are also constantly related to anomalies in meridional winds with correlations of 0.4-0.5, which means a relation between northward winds and increased heat transport.

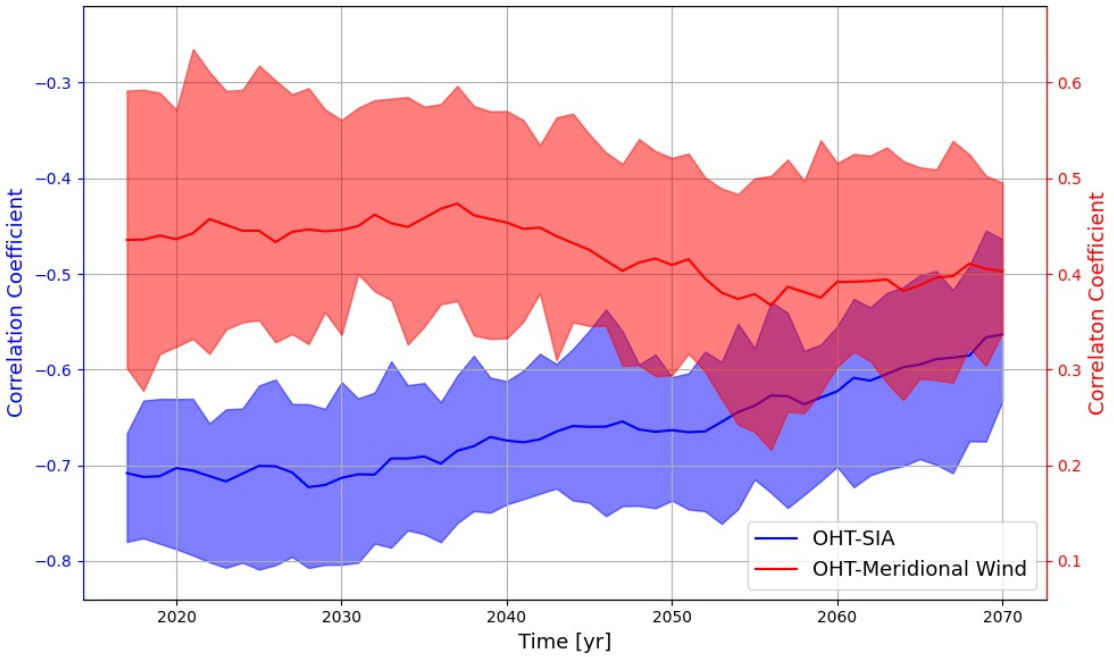

Figure 9: 21-year running correlation of anomalies of OHT via BSO and Barents Sea SIA (blue, refers to the left y-axis) and OHT and meridional winds (red, refers to the right y-axis). The solid lines indicate the average over all ensemble members, and the shading shows the inter-quartile range. Note the different y-axes.

4.3.2 Meridional Wind

A robust relationship is also found between anomalies of Barents Sea-averaged meridional winds and sea ice area (Figure 10). The running correlation shows a fairly stable anti-correlation, slightly decreasing from -0.45 to around -0.4. There is some variability between the different members, with an inter-quartile spread of ± 0.1, but the sign of the correlation remains robust for all individual ensemble members.

The correlation is of similar magnitude to the correlation of meridional winds and ocean heat transport (red line in Figure 9). Both running correlations also show a similar behaviour over time, with a small drop in the correlations between 2040 and 2060. It is therefore reasonable to assume an interdependence of these processes. Part of the correlation between winds and sea ice area might be a result of the influence of the winds on ocean heat transport, a relation that will be further investigated later (Section 4.7). The strong interdependency of circulation anomalies and ocean heat transport in influencing the internal variability of Barents Sea ice area has previously been emphasized by Herbaut et al. (2015).

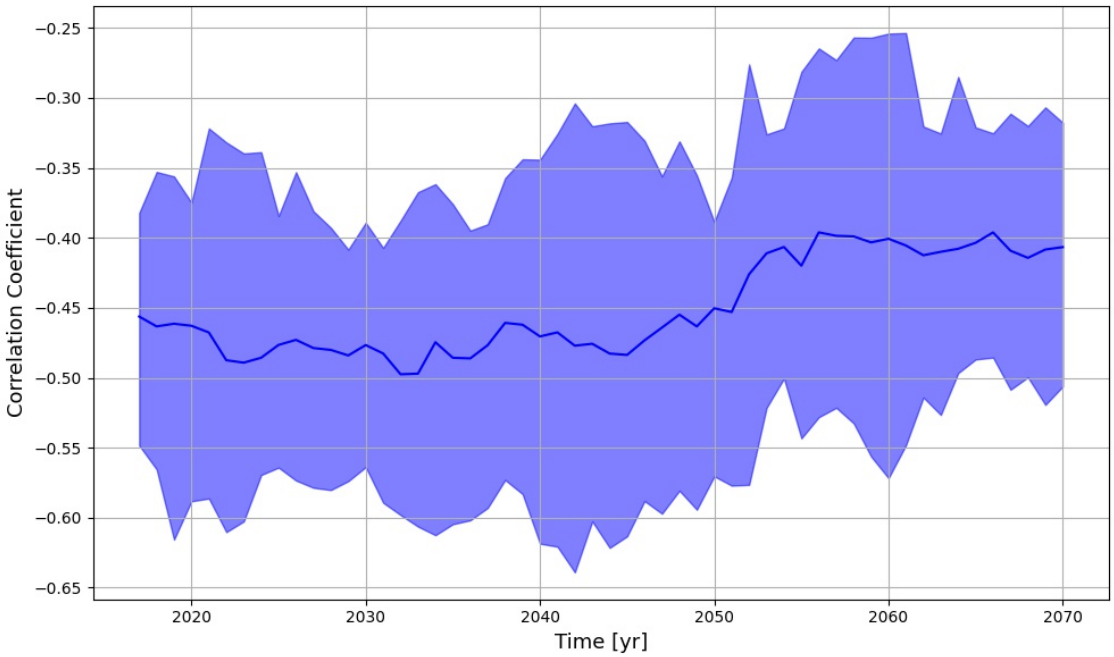

Figure 10: 21-year running correlation of anomalies of meridional wind, averaged over the Barents Sea and Barents Sea ice area. The solid line indicates the average over all ensemble members, and the shading shows the inter-quartile range.

4.3.3 Sea Ice Area Transport

Another important driver of sea ice variability is dynamical forcing via ice import (Kwok, 2009). The Barents Sea is connected to the Arctic Ocean via two main gateways through which ice is transported, a northern gateway (NGW) between Svalbard and Franz Josef Land and an eastern gateway (EGW) between Franz Josef Land and Novaya Zemlya. The location of these gateways is outlined in Figure 11a) and was chosen in alignment with the sea ice grid of the model to be able to calculate ice transport across them.

Ice transport across both gateways is shown in Figure 11b). The ensemble mean of ice transport across the northern gateway is positive during the first half of the simulations, indicating ice export out of the Barents Sea during that time. This is different from the variable transport that Lind et al. (2018) find to switch between import and export in observational data. During the 21st century the simulated ice export decreases from $2 * 10^5$ km²/year at the beginning, crosses the zero-line around 2065, and shows small southward transport and hence ice import thereafter. The variability of ice transport across the northern gateway is, however, large. The inter-quartile range spans a range of roughly $\pm 2 * 10^5$km²/year at the beginning, which is equal to the ensemble mean of that time. Over time the variability drops as the ice area decreases. In 2080, the inter-quartile range of $\pm 8 * 10^4$km²/year still suggests strong cross-member variability. From 2040 onwards, the inter-quartile range includes the zero-line, indicating substantial disagreement between ice import and ice export between the ensemble members.

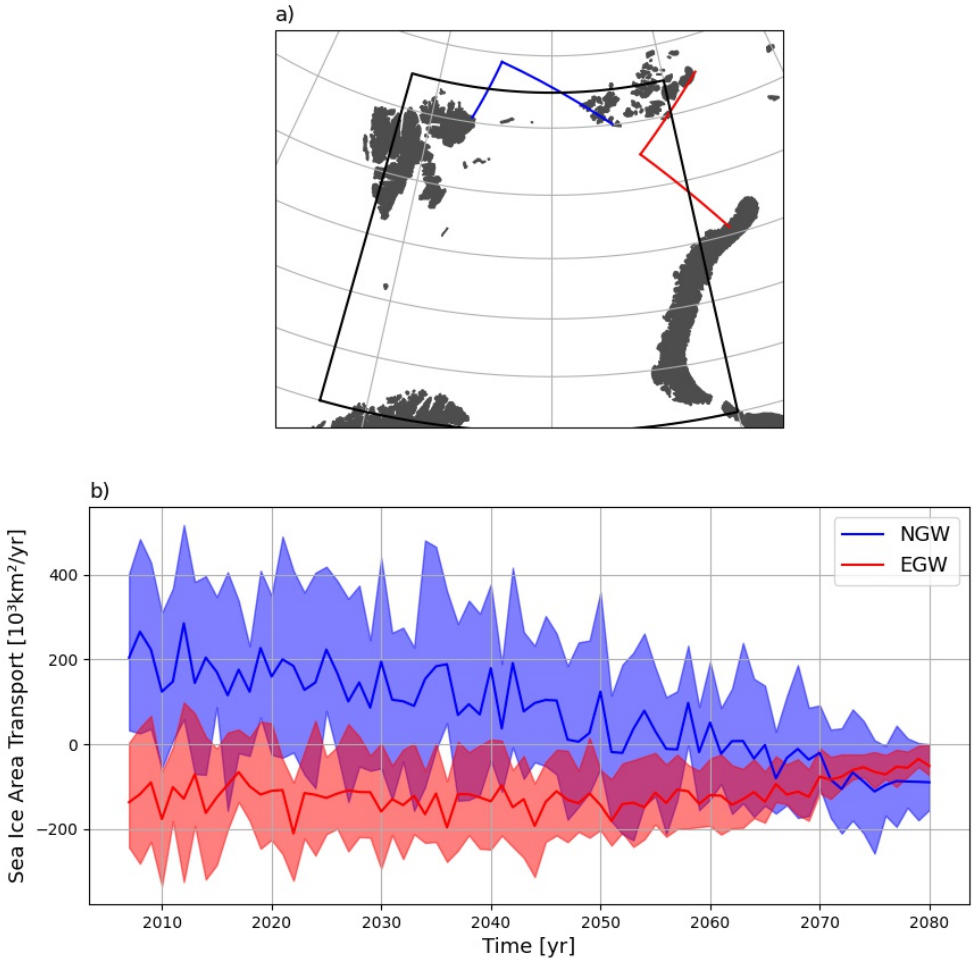

Figure 11: a) Location of the northern (NGW; blue) and eastern (EGW; red) gateway of the Barents Sea in the model grid. b) Winter mean ice transport across the sections. Positive values indicate ice export out of the Barents Sea. The solid lines indicate the ensemble mean and the shading the inter-quartile range of the large ensemble simulations.

Transport across the eastern section is negative, meaning that ice is imported into the Barents Sea which is in agreement with the observation-based findings of Lind et al. (2018). The ensemble mean is quite constant at around $-1 * 10^5 \text{km}^2$/year before it starts to drop towards zero after 2060. Also the variability is lower than for the northern gateway. The inter-quartile range spreads with $\pm 1 * 10^5 \text{km}^2$/year around the mean and decreases during the simulations. In 2080, ice transport through the eastern gateway is very small with little cross-member variability.

Running correlations of ice transport anomalies across both sections and sea ice area anomalies (blue) and meridional winds (red) are shown in Figure 12. At the northern gateway (panel a), ice transport is clearly correlated to meridional winds at 0.65 at present with little cross-member variability, meaning that the winds push ice into and out of the Barents Sea. This relation reduces towards the end of the simulation when

sea ice retreats and the ice transport is reduced, but remains above 0.4 on average. Correlation to SIA in the Barents Sea shows stronger variability, both across the members and in time. The ensemble mean shows an evolution from a slight anti-correlation (low SIA related to larger export / smaller import and vice-verse) to a positive correlation around 2050-2060 and back to no correlation in the 2070s. The mean values are small, and the inter-quartile range includes the zero crossing at all times, indicating that the relationship is not robust across the ensemble members. The positive maximum of this running correlation of 0.1 is reached around 2055 (corresponding to the window of 2045-2065), when the correlation between ice export and winds is reduced, and when the ensemble mean transport changes from ice export to ice import (Figure 11b)). The low values in correlation compared to ocean heat transport, winds and ice transport across the eastern gateway indicate a limited importance of ice transport through NGW in influencing Barents Sea ice conditions.

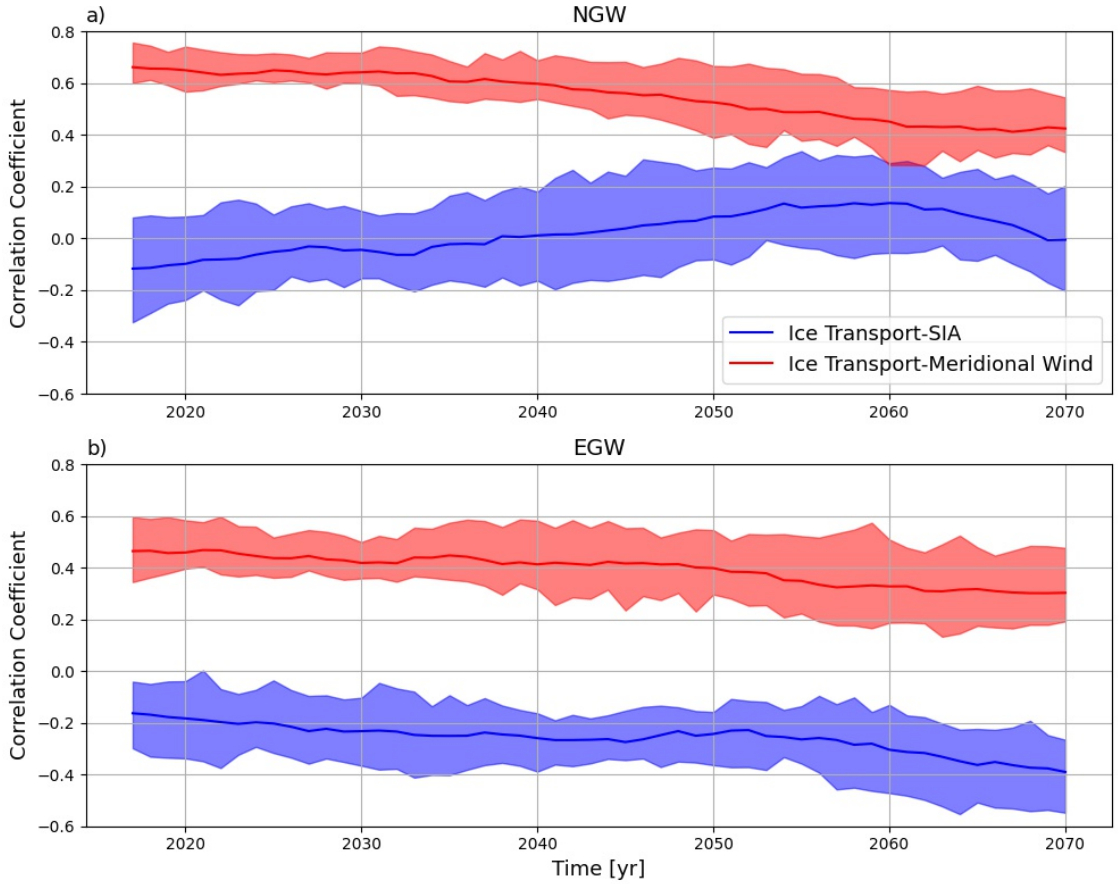

Figure 12: 21-year running correlation between ice export anomalies through the northern (a) and eastern (b) gateway and Barents Sea SIA (blue) and meridional wind anomalies (red). The solid lines indicate the average over all ensemble members, and the shading shows the inter-quartile range.

Ice transport across the eastern section has a lower, but robust correlation to meridional winds that decreases constantly from 0.45 to 0.3. The correlation to SIA is negative, indicating that stronger ice import is related to larger ice area. Whereas this relation is quite small at around -0.2 ± 0.1 during the first half of the simulation, an intensification after 2050 takes place, leading to an anti-correlation of -0.4 at the end of the simulation.

At this part of the simulation, both Barents Sea ice area and ice import via EGW are very small, possibly enhancing the sensitivity of their relationship. The cross-member spread is rather low for both ice transport related to both ice area and meridional winds, indicating that these relations are robust, despite their limited magnitude.

4.4 Abrupt Changes

The response of sea ice to anthropogenic climate change is superpositioned by internal variability, leading to times of ice growth and ice loss. Observational data shows that these fluctuations can occur on time scales of a few years. Between 2004 and 2009 Barents Sea ice area has decreased dramatically, most likely as the sum of the effects of climate change and natural variability (Figure 2). Frequency analysis of the most dominant mode of sea ice concentration variability in the Barents Sea exhibits a peak in the power spectrum at a period of 10-15 years which would be in agreement with sub-decadal trends with a duration of 5-10 years. Motivated by this peak, the presence of short change events in the observations and similar studies focusing on rapid ice loss in the Arctic (Holland et al., 2006; Auclair and Tremblay, 2018), this study will focus at trends with a duration of 5 to 10 years which is roughly half of the dominant period of the net-change mode. In the following part of the study, these trends will be investigated.

Figure 13 shows the distribution of 5-year trends of Barents Sea ice area in future simulations after the ensemble mean has been removed (blue), and in observations after a 4th-order polynomial (representing anthropogenic forcing, following Bonan et al. (2021)) has been removed (grey). Both the observations and model simulations show a normal distribution during the first part of the simulations, with mostly small trends and some larger trends. Trends of up to $1*10^5$km²/year are found in both, observations and model simulations. Comparison with the observational data indicates that the simulations tend to produce slightly stronger variability at the beginning of the simulations, with trends of $5 * 10^4$km²/yr and more occurring more frequently. Weaker trends are being simulated less frequently. The difference in calculating the anomalies has to be kept in mind here. Over time, this behaviour shifts as the trends in the future simulations become more confined to the centre of the histogram, and strong trends occur less often. Between 2047 and 2066 (panel c) the simulated trends resemble the distribution of observational trends very well. At the end of the simulations (2067-2080, panel d) the histogram is dominated by small trends of less than $1 * 10^4$km²/year that account for more than half of all calculated trends, whereas strong trends do no longer occur. This is a direct consequence of the small sea ice area at this time. All histograms are symmetric and not skewed, indicating the same probability of strong ice growth and ice loss, as we also find it in the observational data.

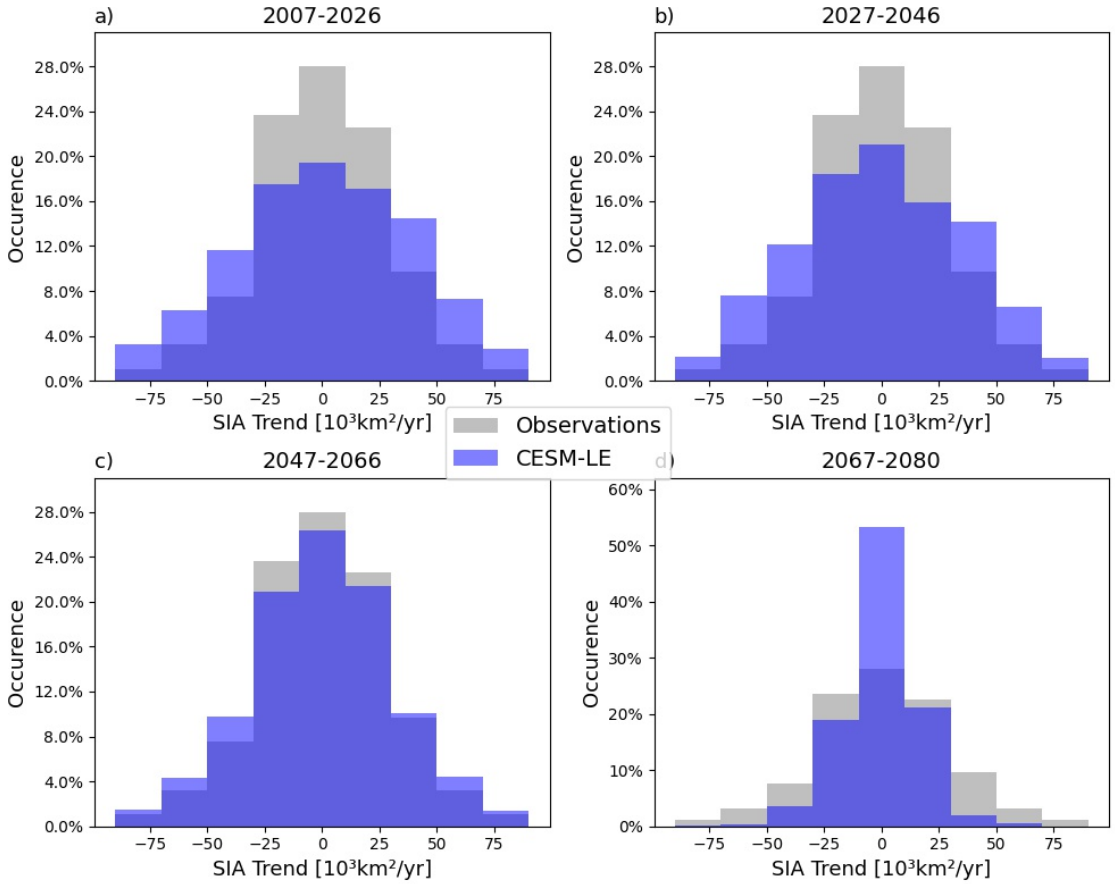

Figure 13: Distribution of 5-year trends of Barents Sea ice area anomalies for different time periods of the future simulations (blue) and the observations (grey). Observational anomalies were calculated by removing a 4th-order polynomial from the raw data that is supposed to represent the signal related to anthropogenic forcing, whereas the remainder represents internal variability. The future simulations are divided into 4 time frames, from 2007-2026 (a), 2027-2046 (b), 2047-2066 (c) and 2067-2080 (d). The date corresponds to the centre of any 5-year-episode. Note the different y-axis in 2067-2080. The histogram for the observations remains the same in every panel.

The spatial distribution of the trends is investigated in Figure 14. Red shading indicates the frequency of strong SIC trends (larger than 8% per year) occurring at each grid point in the respective time period. In the beginning of the simulations (panel a), strong trends are spread over most parts of the Barents Sea apart from the ice-free southwestern area and the gateways to the central Arctic Ocean and Kara Sea. Throughout the simulations, the area of strongest trends moves northeastward. Between 2047-2066 (panel c), this area is confined to the northern and eastern part of the Barents Sea and the frequency is clearly reduced compared to the beginning of the simulations. In the last part of the simulations (panel d), strong trends in SIC are limited to the northern and eastern gateway, and the area south of Novaya Zemlya. The central Barents Sea does no longer show any trends exceeding the threshold.

In combination, Figure 13 and Figure 14 demonstrate a decay and shift of strong short-term changes in sea ice cover in the Barents Sea. The area of largest variability moves northeastward during the simulations, and finally retreats past the boundaries of the

Barents Sea as it is defined in this study, resulting in a strong decrease in the occurrence of strong SIA trends towards the end of the simulations (Figure 13d). The areas of largest SIC trends highlighted in Figure 14 compare well with the retreat of the ice edge that is shown in Figure 5. Most sub-decadal variability is thus confined to the area of the marginal ice zone which is partly ice-free and partly ice-covered.

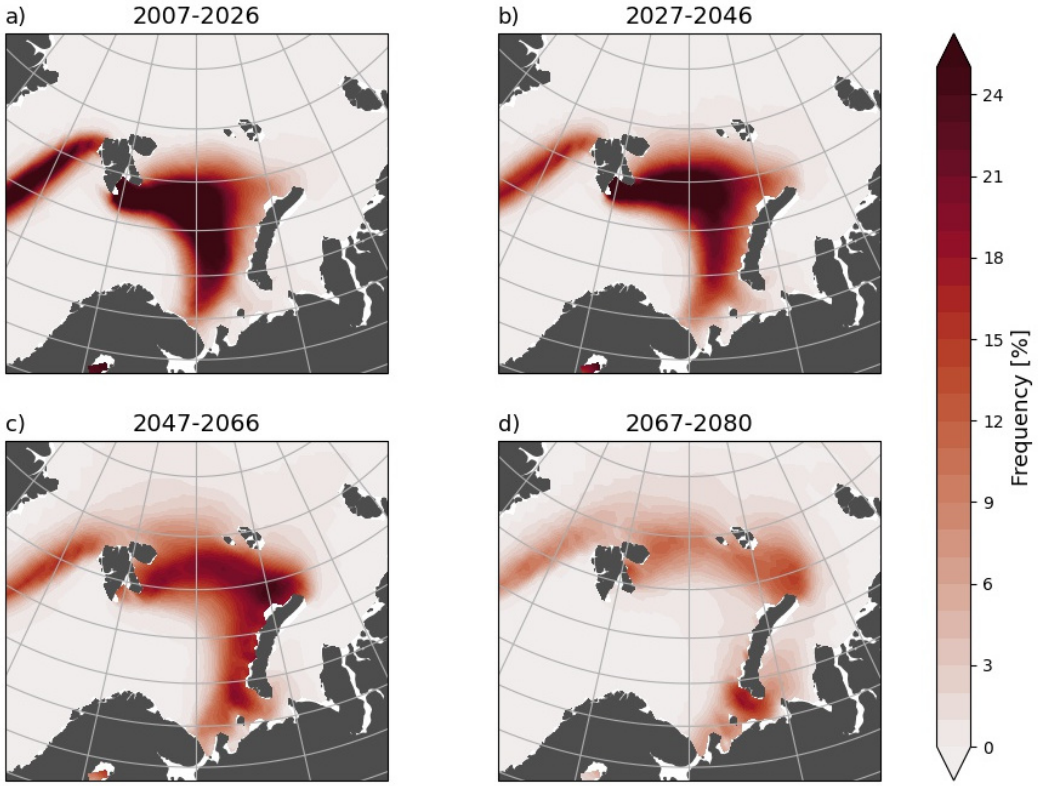

Figure 14: Frequency of occurrence of strong 5-year trends of winter sea ice concentration. A strong trend is defined as a linear trend over 5 years that is exceeding a threshold of 8% per year. The shading indicates the ratio of the number of trends that exceed this threshold to the total number of trends in each respective time period.

Based on the distributions shown in Figure 13, the following analysis will focus on the most extreme trends in Barents Sea ice area anomalies that are found in the tails of the distribution. Abrupt changes in sea ice area are therefore defined as follows: Over a period of at least 5 years, the trend must exceed $5 * 10^4$km²/year. Although this is a somewhat arbitrary criterion, it serves well in capturing strong events of short-term sea ice change in the area, and is of similar nature to the one used by Holland et al. (2006) for ice loss events in the Arctic. Following this approach, 140 ice growth and 141 ice loss events with a duration of 5 to 9 years were detected in the simulations (Figure 15). Most of the events occur before 2050, but there is also one ice loss event occurring as late as 2070. After 2050, events are mostly confined to those ensemble members where sea ice area is large compared to the ensemble mean (Figure A.2). There is no difference in the timing of ice growth and ice loss events. On average, each ensemble member produces 3.5 ice growth and ice loss trends each, and at least one event of each kind can be found in every member. The average ice growth event lasts for 5.6 years at $6.0 \pm 0.9 * 10^4$ km²/year, the average ice loss events last for 5.7 years at $-5.9 \pm 0.7 * 10^4$ km²/year.

Strong short-term trends are hence a common feature of internal variability in Barents Sea ice area.

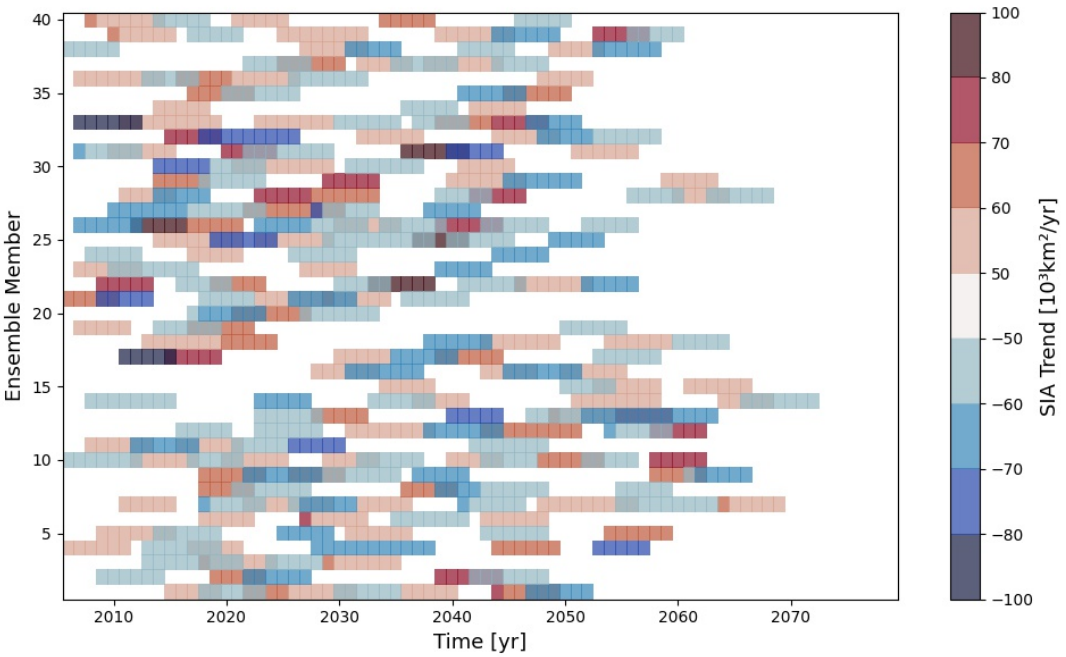

Figure 15: Identification of events of abrupt ice growth (red) and ice loss (blue). An event of abrupt change is defined when the linear trend of sea ice area exceeds the threshold of $5 * 10^4 \text{km}^2/\text{yr}$ over a duration of at least 5 years. Applying this criterion results in 140 ice growth and 141 ice loss events.

Averaging over all 140 / 141 events gives an impression of the general spatial pattern that is associated with these events. Figure 16 shows the spatial patterns for both ice growth and ice loss events. On average, the differences in the pattern between ice growth and ice loss events are very small and the patterns resemble the SIC pattern associated with the net-change-mode well (Figure 7). The strong SIC trends cover most of the Barents Sea apart from the area near the BSO in the southwest, with maximum values in the central to northeastern Barents Sea. Strong ice loss/growth events in the Barents Sea are also associated with trends in the Kara Sea and the area north of Svalbard and Franz Josef Land, and west of Svalbard. Small signals are visible in the area of southern Greenland, the Bering Strait and the Siberian and North American coast.

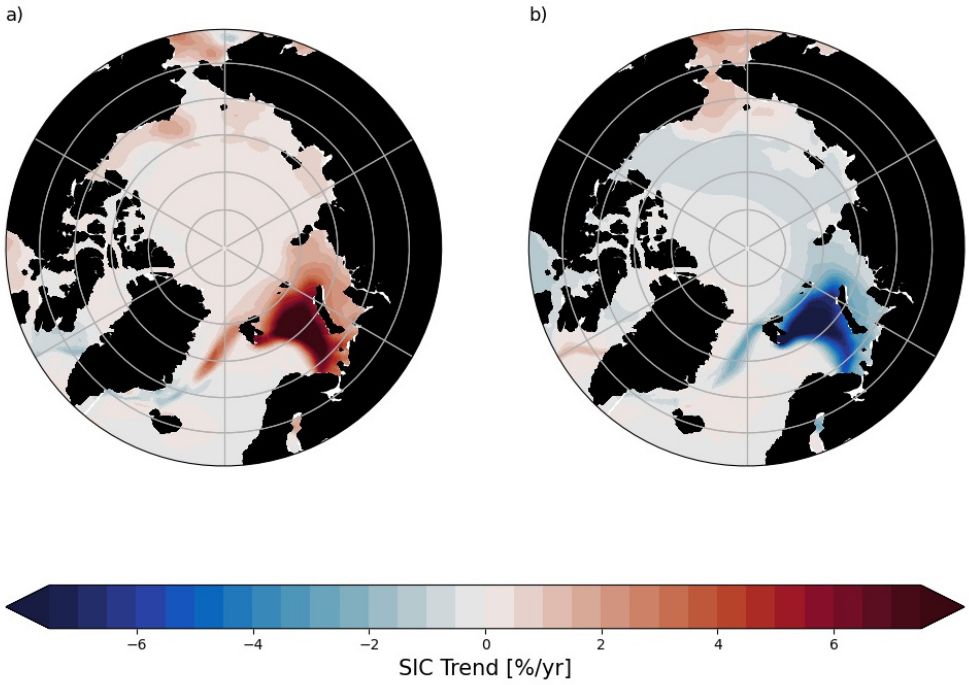

Figure 16: Spatial pattern of SIC trends for ice growth (a) and loss (b), averaged over all events identified in Figure 15.

4.5 Forcing of Abrupt Sea Ice Trends

In the following section, the driving mechanisms of the abrupt sea ice changes will be investigated, both for ice loss and ice growth events. For this purpose the events will be related to trends and means of the four potential drivers identified earlier, namely ocean heat transport, meridional winds and ice transport through the northern and eastern gateway. For each event, the trend and mean of each parameter over the duration of the respective event will be calculated, and compared to the standard deviation of all trends / means of that respective duration. Assuming a normal distribution, 68% of all trends / means would lie within the interval of one standard deviation around the mean, leaving 16% on either side. If strong trends in SIA coincide with strong trends / means of another parameter in significantly more than 16% of the cases, a physical relationship can be expected. A summary can be found in Table 2.

4.5.1 Ocean Heat Transport

Figure 17 shows the resulting scatter plots of SIA trends versus OHT trends (top) / means (bottom) for ice growth (left) and ice loss (right) events. The distribution shows a clear tendency towards opposite trends, meaning that ice growth tends to be related to a decrease in OHT and ice loss to an increase. 63% of the ice growth events and 65% of the ice loss events show a contrary trend that exceeds one standard deviation. There seem to be no clear indication that a stronger or longer ice change event is more or less likely to be influenced by trends or means in ocean heat transport. 29% of the ice growth and 18% of the ice loss events are related to anomalously low (high for ice loss events) mean OHT conditions exceeding one standard deviation over the respective

duration. There is also a few events where the mean of OHT shows a positive (negative) anomaly during ice growth (loss), and the distribution appears overall more symmetric.

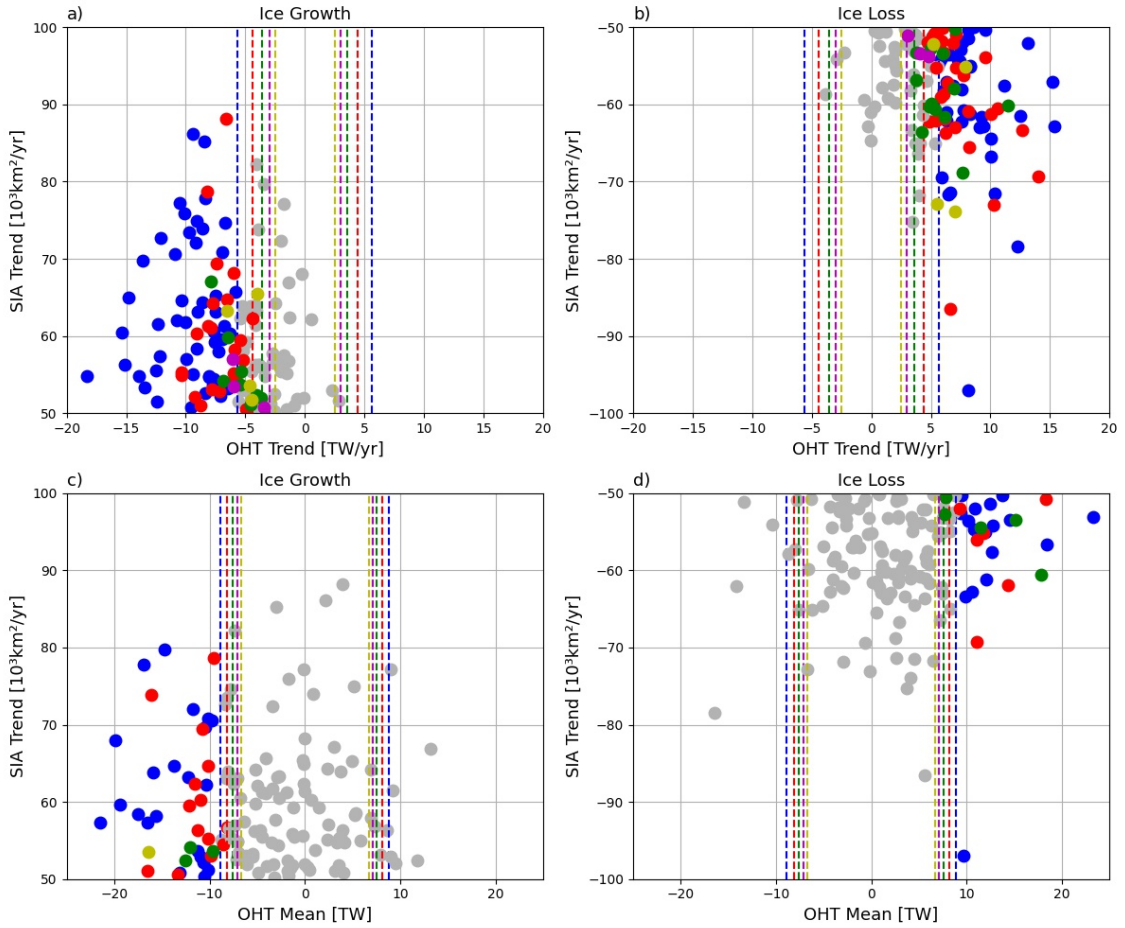

Figure 17: Trends in sea ice area (y-axis) versus trends (top) and means (bottom) of ocean heat transport (x-axis) over the duration of ice growth (left) and loss (right) events. Coloured values indicate trends / means that exceed one standard deviation of all trends / means of that particular duration which is marked by the dashed lines. The different colours indicate the duration of the trends of 5 (blue), 6 (red), 7 (green), 8 (magenta) and 9 (yellow) years.

4.5.2 Meridional Winds

The relationship between SIA trends and trends (top) and averages (bottom) of meridional winds is shown in Figure 18. Approximately half of the events can be related to opposing trends in meridional winds (52% of the ice growth events and 46% of the ice loss events). The distribution is clearly shifted, so that ice growth events can in general be related to winds with an enhanced northerly component, and ice loss events to an enhanced southerly component. Stronger events tend to be more likely associated with trends in meridional winds as can be seen by the tendency of scatter points to the top-left (bottom-right) for ice growth (loss) in panel a (b)). Some SIA trends also show a relation to wind means, but this occurs less often (23% and 20% for ice growth and loss, respectively), and the distribution of wind means seems more symmetric across all ice growth and loss events.

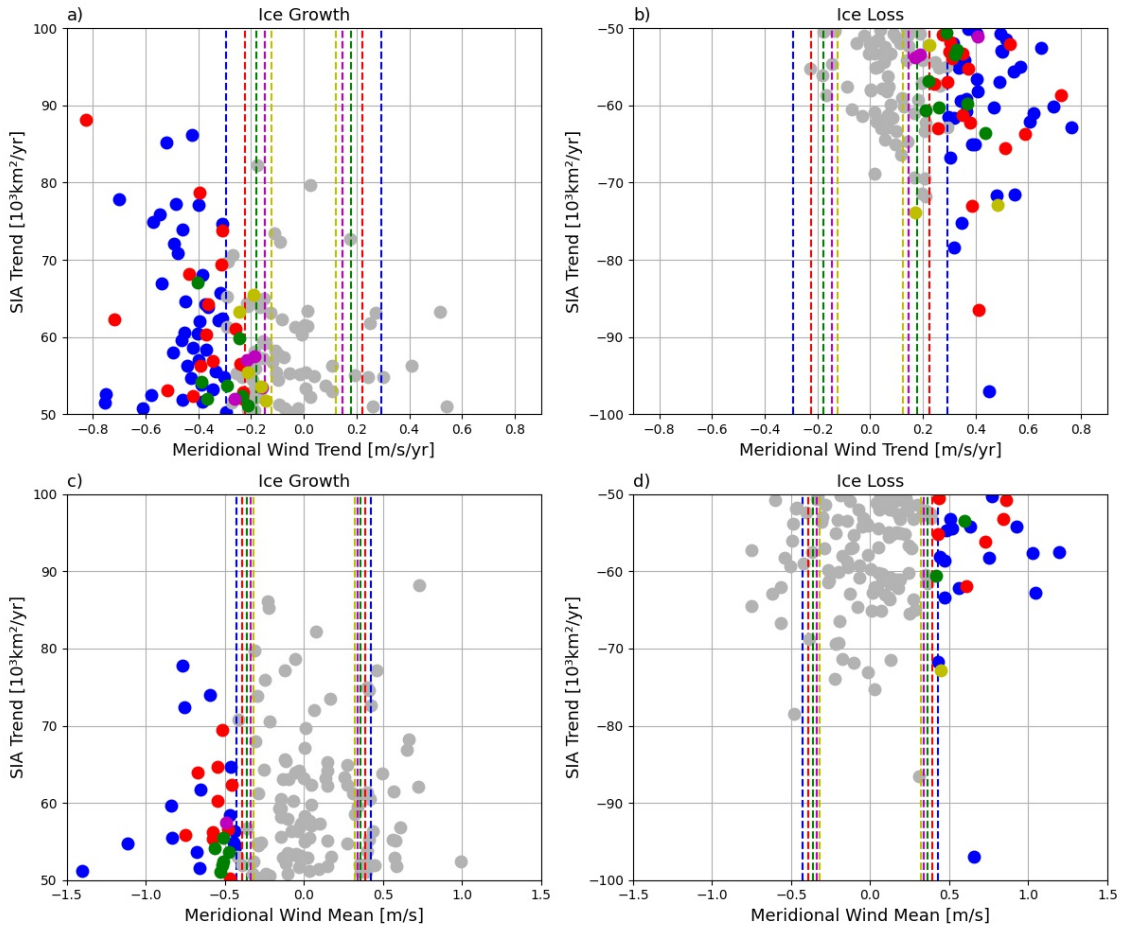

Figure 18: As in Figure 17, but for meridional winds. Northward winds are defined positive, meaning that a positive trend can indicate an increase of northward winds, or a decrease of southward winds.

4.5.3 Sea Ice Area Transport

The relation between trends in SIA and trends in ice transport through the northern gateway (between Svalbard and Franz Josef Land) is shown in Figure 19. The distribution of ice transport trends is more symmetrically distributed around 0, and only 19% of the ice growth and 17% of the ice loss events can be related to increasing ice import (for ice loss) and export (for ice growth) through the northern gateway (panel a and b), which is substantially lower than for OHT and meridional winds (Table 2), and comparable to the expected value of 16% when the parameters were completely independent. There is also a number of events where ice growth is accompanied by an increase in ice export, and ice loss by an increase in import. It is therefore possible to associate some of the ice growth events to increasing ice import, but also to increasing ice export. However, especially strong sea ice trends are more often associated with trends in ice import (Coloured dots on the top-left (bottom-right) corner of the ice growth (ice loss) panel). For these stronger events (SIA trend $> 6 * 10^4$km²/year), the distribution is more asymmetric towards decreasing (increasing) ice export during ice growth (loss). This holds especially for ice growth, but also for ice loss events. The means of ice transport (17% and 23% can be related to ice growth / loss events) show a similar behaviour with negative and positive means occurring during both growth and loss events, but they do not show the

tendency of an intensified relationship for stronger SIA trends.

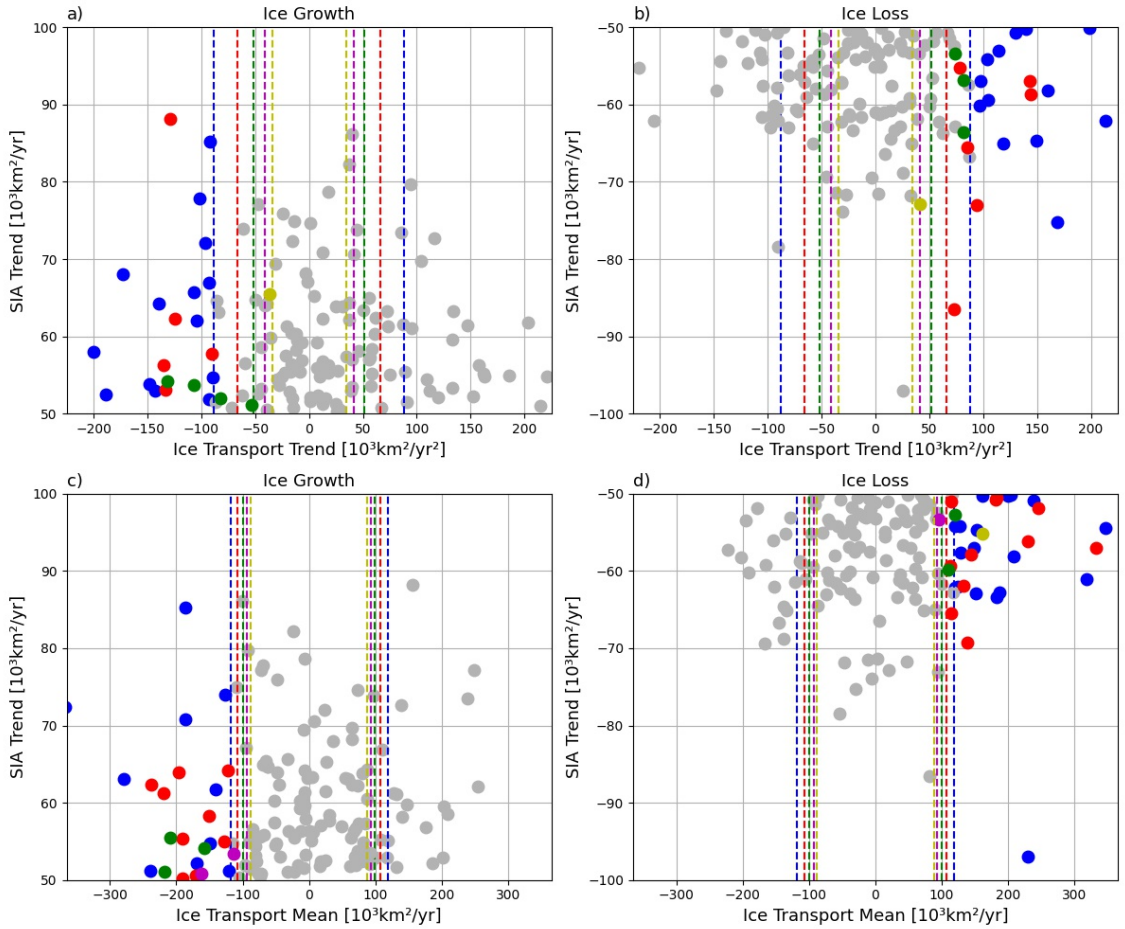

Figure 19: As in Figure 17, but for ice transport through the northern gateway. Positive ice transport is defined as ice export out of the Barents Sea, positive trends relate hence to an increase in ice export or a decrease in ice import.

Results for the ice transport through the eastern gateway (Franz Josef Land to Novaya Zemlya) indicate a slightly intensified relation to SIA trends (Figure 20). Although 26% of the ice growth and 28% of the ice loss events are clearly related to increasing (decreasing) ice import, the opposite situations can also be found, when ice growth (loss) is related to decreasing (increasing) ice import. The overall distribution is fairly symmetric, both for trends and means. 25% of the ice growth events and 18% of the ice loss events show a relation to negative / positive means of ice transport, but also the opposite occurs. No intensification of the relationship for stronger events is visible in Figure 20. These results indicate that the relationship between ice transport and SIA trends is less robust than for OHT and meridional winds, but can still be important in forcing individual events.

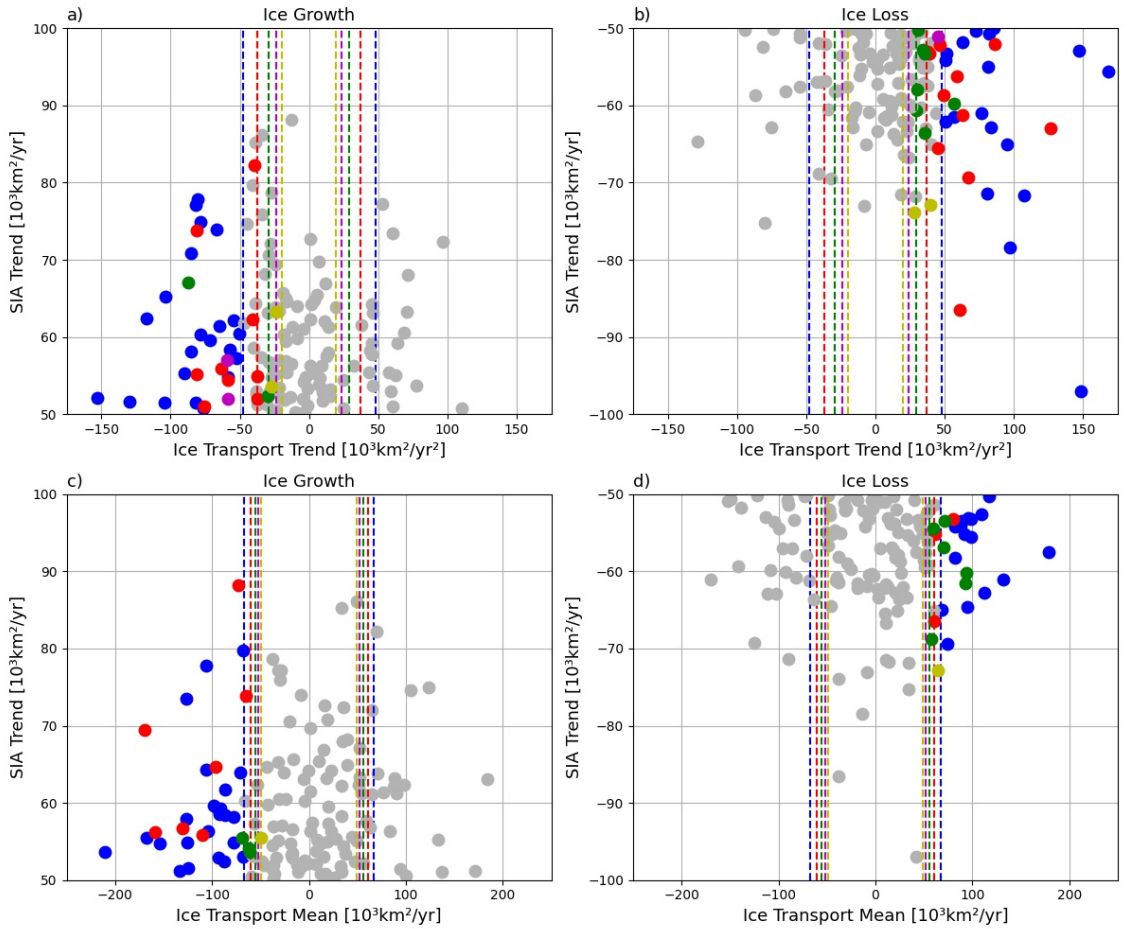

Figure 20: As in Figure 17, but for ice transport through the eastern gateway. Positive ice transport is defined as ice export out of the Barents Sea, positive trends relate hence to an increase in ice export or a decrease in ice import.

A summary of the driving mechanisms of abrupt sea ice trends is shown in Figure 21. This figure shows the fraction of ice growth (left) and ice loss (right) events that can be associated to trends of the respective driver. The combinations of ocean heat transport and meridional winds and meridional winds and NGW ice transport were included as these mechanisms show a large amount of joint forcing. The calculation of the fractions is exclusive, meaning that when an event is related to a combination of drivers, it will not be counted in the individual drivers.

OHT stands out as the most important driving mechanism, as it is related to the largest fraction of both ice growth events and especially ice loss events. A large number of events are also associated with strong trends in both wind and OHT. Although many events also show a strong trend in winds (Figure 18, Table 2), Figure 21 shows that almost all of these events are a result of a co-forcing of meridional winds together with either OHT or ice transport through the northern gateway, indicating that wind forcing acts as a driver for one of these mechanisms that then lead to ice growth/loss. This is further investigated in Section 4.7. While ice transport through the northern gateway only plays a role in coincidence with meridional winds at an early stage in the simulation run, the eastern section contributes to some more events. This is especially the case in the second half of the 21st century, where ice transport through the eastern gateway

becomes the second most-dominant driver of sub-decadal sea ice variability.

Over time, as the number of events decreases (the number of events per decade is indicated by the blue line at the top of Figure 21), the relative importance of the combination of meridional winds and northern gateway ice transport decreases, and the relative importance of ice transport through the eastern gateway increases slightly. The other forcing mechanism on the other hand seem to be rather unchanged in their relevance. There are only small differences between the forcing of ice growth and ice loss events.

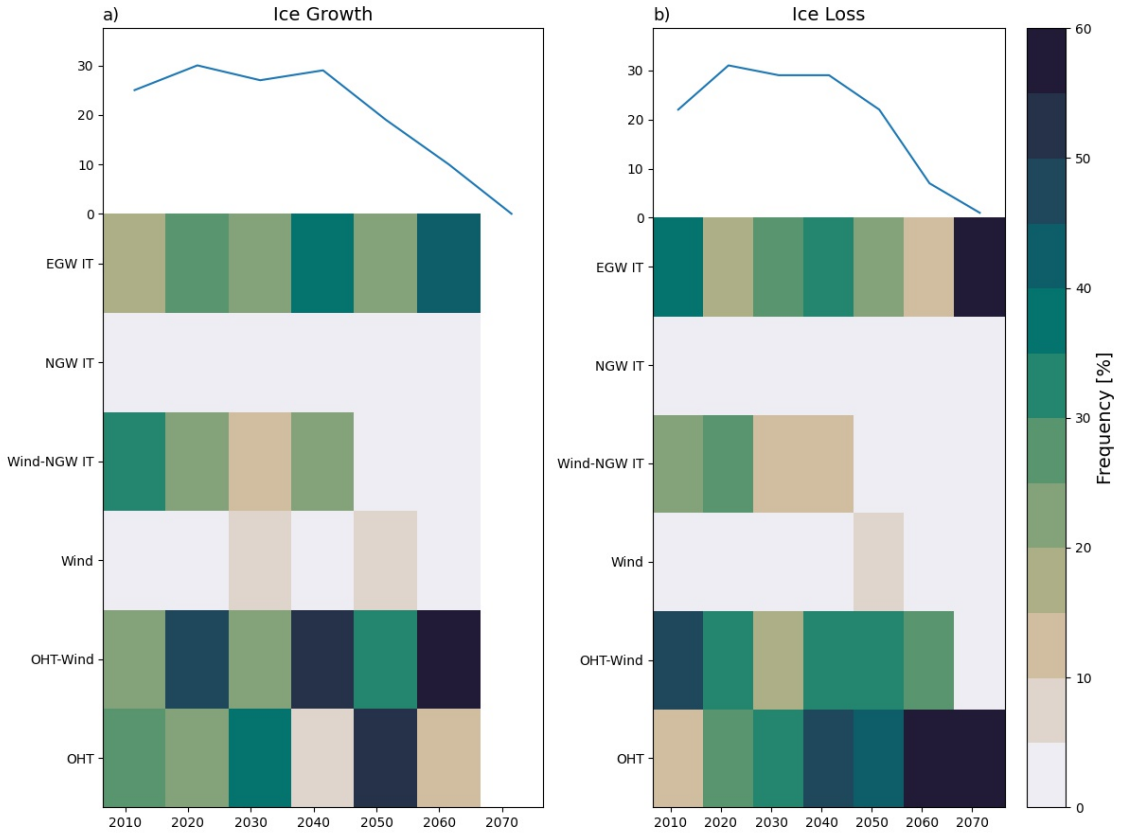

Figure 21: The colour of each field indicates the fraction of ice growth (left) and ice loss (right) events starting in the particular decade that can be associated with the respective forcing mechanism. The blue line at the top indicates the total number of events in that decade. EGW IT and NGW IT refer to ice transport through the northern and eastern gateway, respectively.

Ice Growth

Time Period	07-16	17-26	27-36	37-46	47-56	57-66	67-76	Total
Number of events	25	30	27	29	19	10	0	140
Of these:								
OHT trends	12	20	16	17	16	7	0	88
OHT means	4	4	7	12	6	7	0	40
Wind trends	11	19	11	19	7	6	0	73
Wind means	6	10	5	6	2	3	0	32
NGW IT trends	9	6	4	7	0	0	0	26
NGW IT means	8	8	2	4	1	1	0	24
EGW IT trends	4	8	6	11	4	4	0	37
EGW IT means	7	7	8	8	1	4	0	35

Ice Loss

Time Period	07-16	17-26	27-36	37-46	47-56	57-66	67-76	Total
Number of events	22	31	29	29	22	7	1	141
Of these:								
OHT trends	13	18	15	23	16	6	1	92
OHT means	3	11	6	5	3	0	0	28
Wind trends	16	14	10	13	10	2	0	65
Wind means	3	9	5	6	2	0	0	25
NGW IT trends	5	9	5	4	1	0	0	24
NGW IT means	3	7	9	8	5	1	0	33
EGW IT trends	8	6	8	10	5	1	1	39
EGW IT means	3	12	6	4	1	0	0	26

Table 2: Summary of the number of events identified in Figure 15 that can be associated with trends and means in the four different driving mechanisms. EGW IT and NGW IT refer to ice transport through the northern and eastern gateway, respectively.

4.6 Sea Ice Concentration Budget

Calculating a sea ice concentration budget gives the possibility of further investigating the forcing mechanisms of changes in sea ice conditions. As described in Section 3.2.9, the total ice change is a result of mechanical (advection and divergence) and thermodynamical (freezing and melting) processes. Model output from the CESM-LE simulations includes dynamical and thermodynamical tendency terms which enables the investigation of the contribution of these processes to the overall change of SIC.

Figure 22 shows the winter (November-April) climatology of the ice tendency term (top), and the individual dynamical (middle) and thermodynamical (bottom) contribution for different time periods during the future simulations. Winter conditions are defined by overall ice growth in the Barents Sea, that is centred in the northern and eastern Barents Sea at present. This pattern is the result of strong thermodynamical ice production in the coastal areas, mainly along Novaya Zemlya and around Franz Josef Land, and also at the coast of the Kara Sea. This ice is then transported away from the coast, leading to strong dynamical ice loss at the coast. In the ocean interior, thermodynamical ice production is

visible in the northern part of the Barents Sea, but at a much smaller amplitude than the coastal ice formation. This is also accompanied by a negative dynamical contribution. A small reversed contribution is visible in the ice-free part of the Barents Sea, with a small intensification south of Svalbard during the first half of the simulations (panel e and f). This signal represents the ice convergence and melting that takes place in the area of the marginal ice zone. It is of high importance to note here that the dynamical and thermodynamical term are strongly anti-correlated. Thermodynamical ice formation is clearly accompanied by strong dynamical ice loss (due to ice divergence), whereas dynamical ice growth is associated with thermodynamical melting. In combination, both processes result in SIC change of one order of magnitude smaller than the individual components by themselves (note the differences in colourbar spacing in Figure 22).

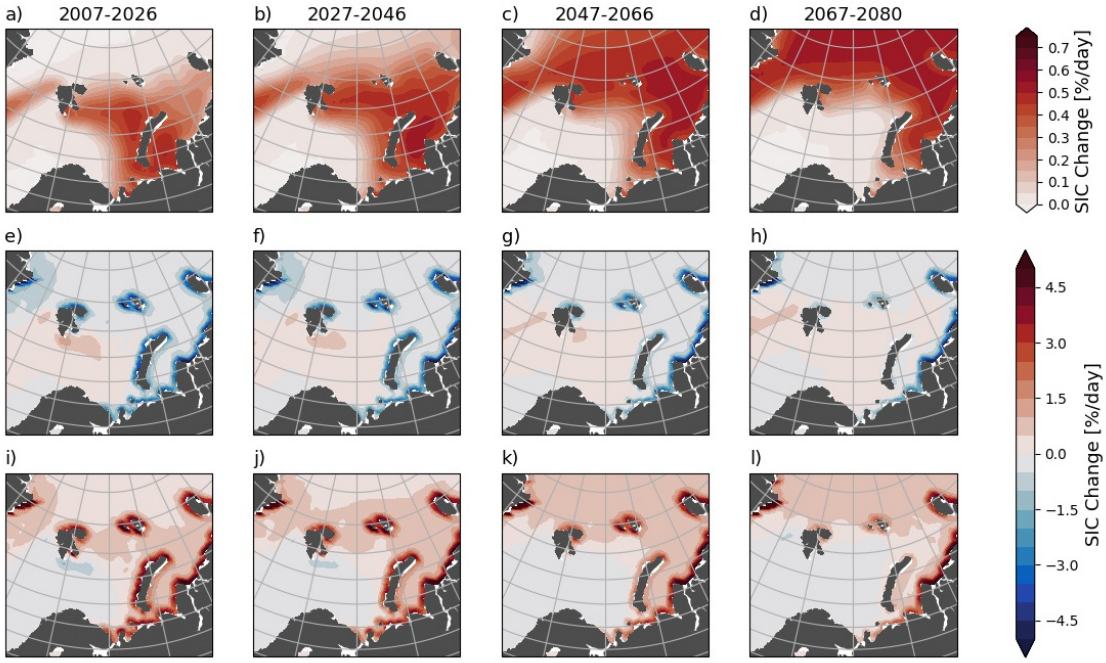

Figure 22: Winter (November - April) means of total (top), dynamical (middle) and thermodynamical (bottom) ice tendency terms during different parts of the simulation runs. The total ice tendency was calculated as the sum of dynamical and thermodynamical ice change.

Throughout the simulations, the retreat of the sea ice to the north is very well visible in the overall ice change pattern (top panels in Figure 22). Between 2067 and 2080 the area of most intense positive ice tendency has left the Barents Sea and is focused on the Kara Sea and the area north of Svalbard and Franz Josef Land. This retreat is also visible in the individual components. Thermodynamical ice production is reduced in the Barents Sea, moves northward and retreats along the coasts. In 2047-2066 (panel g and k), thermodynamical ice production and dynamical divergence in the Barents Sea is mainly focused around Franz Josef Land and in 2067-2080 (panel h and i), production has decreased in the whole Barents Sea and is much smaller than along the coast of the Kara Sea.

The summer season (May - October) is characterised by quite uniformly distributed ice loss that is mainly a result of thermodynamical melting (Figure A.4).

4.6.1 Interannual Variability

Year-to-year variability of winter sea ice is determined by the ice change throughout the year, covering the whole cycle of freezing and melting. To be able to relate the variability in winter sea ice area to the terms of the sea ice concentration budget, annual integrals from one winter to the next were calculated. The pattern of these annual integrals is represented well by the winter climatology in Figure 22. Removing the ensemble mean from these winter-to-winter values results in the anomalies that were used for the further analysis of the budget terms.

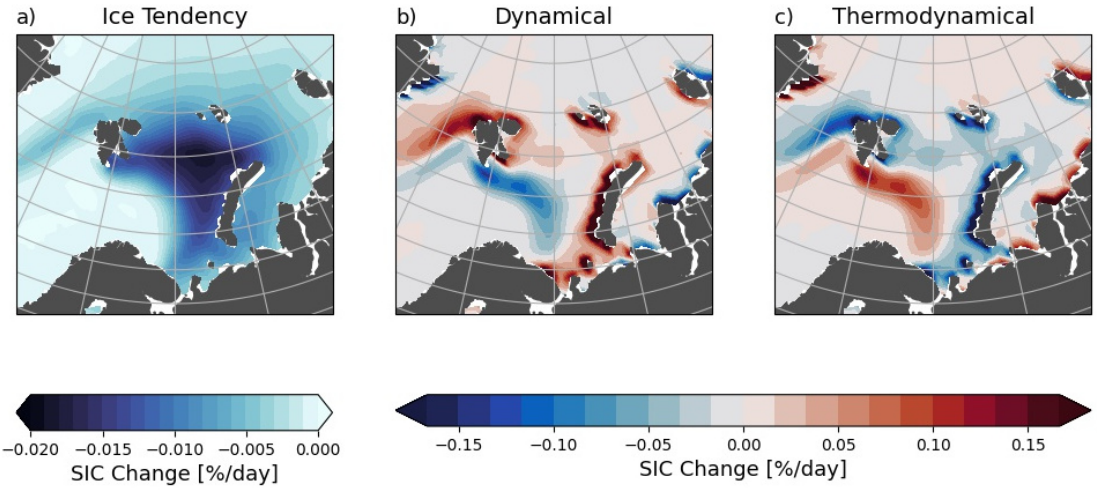

Figure 23: Regression of anomalies of the annually integrated SIC tendency terms on the PC timeseries of the first dominant mode of SIC variability as shown in Figure 6. The resulting patterns are hence associated with low sea ice conditions in the Barents Sea. The total tendency term was calculated as the sum of the dynamical and thermodynamical term. Note the difference in the colourbar of the total term compared to the individual components.

Figure 23 shows the regression of the anomalies of the SIC budget terms on the first PC timeseries. The resulting patterns can hence be related to the negative phase of the net-change-mode as it is shown in Figure 6 that represents a low sea ice state in the Barents Sea. The overall tendency exhibits an ice loss pattern that resembles the EOF1 in Figure 6 and the spatial pattern of ice loss trends in Figure 16 with a centre of action in the northeastern Barents Sea. The ice loss extends also out of the boundaries of the Barents Sea into the adjacent Kara Sea and Arctic Ocean. The patterns of the dynamical and thermodynamical contribution are more diverse. A low sea ice state in the Barents Sea is clearly related to negative thermodynamical ice change anomalies along the coastline of Svalbard (except the southern part), the southern coast of Franz Josef Land, the west coast of Novaya Zemlya, the eastern part of the Norwegian north coast and the coast of Russia (Figure 23b). Given that these coastal areas are sites of strong ice production (Figure 22b), this indicates reduced ice formation. Consequently, these areas exhibit positive anomalies in the dynamical terms, which indicates reduced divergence (Figure 22c). This suggests that changes in local ice formation in winter explain a large amount of interannual sea ice variability in the Barents Sea. Smaller contributions of this sign are also visible in the Barents interior and the eastern gateway to the Kara Sea. In the area of the ice edge from south of Svalbard towards the southeast,

a negative (positive) signal is visible in the dynamical (thermodynamical) component. Large positve anomalies in the thermodynamical components and negative anomalies in the dynamical components are visible along the coast of the Kara Sea. These are sign-reversed compared to the coastal signals within the Barents Sea.

4.6.2 Forcing of the Abrupt Changes

To shed some more light on the forcing of the events of abrupt change in ice cover identified in Figure 15, the tendency terms of the SIC budget during these events are now investigated. The spatial integrals over the Barents Sea are visualized in Figure 24, transforming the SIC tendency to a SIA tendency. As seen in panel a) and b), ice growth events are related to positive means of sea ice area change, and ice loss events to negative means. This is a trivial result, but serves as a good validation of the method. Averages of the SIA tendency are, however, smaller compared to the linear trends of SIA. The threshold of $5 * 10^4$km²/year that was used to identify abrupt changes is not reached in a large number of both, ice growth and loss events, which can be explained by the difference in calculation of linear trends and annually integrated tendency terms.

Looking at the contribution of the dynamical and thermodynamical tendency term individually shows a more variable pattern. The spread is much increased, ranging from averages of $-2 * 10^5$km²/year to $3 * 10^5$km²/year in ice growth events ($-3 * 10^5$ to $2 * 10^5$km²/year for ice loss events), which is up to four times as large as the corresponding linear trends in SIA. Using the standard deviation of short-term averages as a threshold, 26.4% of all ice growth (31.2% of loss) events show a clear relation to dynamical ice production and 17.1% of the ice growth events (13.6% of loss events) shows a relation to thermodynamical tendency. Most of the events can hence be attributed to neither clearly positive nor negative dynamical or thermodynamical contributions, emphasizing the complexity of the mechanisms that govern sea ice variability. This finding is robust across different intensities and durations of the ice growth and loss events, meaning that the strength or duration has no apparent influence on whether an event is more likely to be associated with dynamic or thermodynamic forcing.

In order to clarify the mechanisms at play in these events, all ice growth and loss events were divided into three subcategories: Those events, where the average of the dynamical SIA tendency exceeds the overall SIA tendency (which involves a reversed contribution of the thermodynamical SIA tendency) are considered dynamically-dominated and those with the thermodynamical contribution exceeding the overall tendency (hence, a sign-reversed dynamical contribution) are considered thermodynamically-dominated. The remaining events are considered a mixed result of dynamical and thermodynamical ice change. This distinction results in 67 (75) dynamically-dominated, 43 (40) thermodynamically-dominated and 30 (26) mixed ice growth (loss) events, showing a tendency towards the dynamical tendency term being dominant.

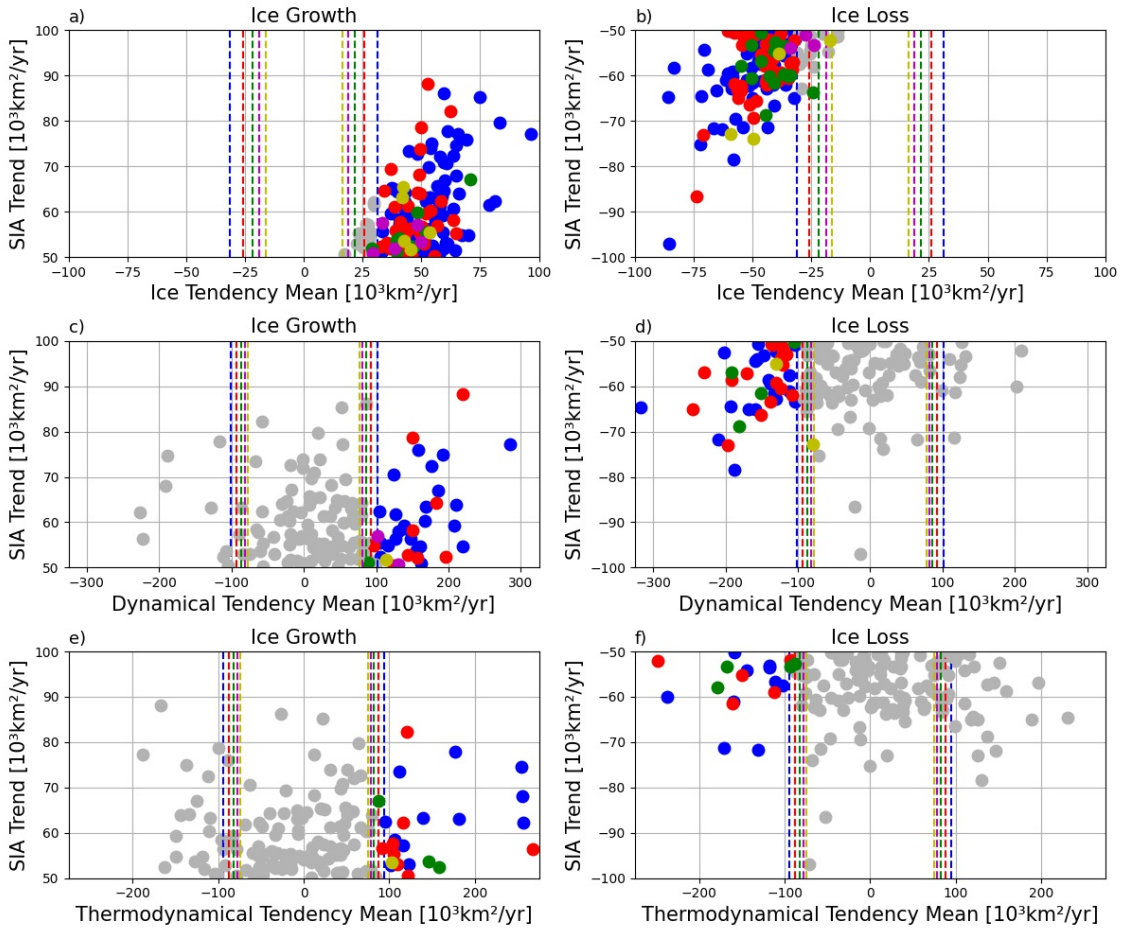

Figure 24: Top: Mean of the SIA tendency term (sum of the thermodynamical and dynamical contribution) over the duration of the ice growth (left) and ice loss (right) events identified in Figure 15. The SIA tendency terms were calculated as the area integral of the SIC tendency terms over the Barents Sea. The coloured dashed lines indicate the standard deviation of SIA tendency means over a duration of 5,6,7,8 and 9 years. Coloured dots indicate those events where the SIA tendency term exceeds this standard deviation of the respective duration. Middle: Same as at the top, but for the dynamical ice tendency. Bottom: Same as at the top, but for the thermodynamical ice tendency. Note the differences in the spacing of the x-axes.

Figure 25 shows the spatial pattern of the SIC tendency terms for the dynamically- (top) and thermodynamically-dominated (bottom) ice growth events. For both event types, the overall tendency pattern remains the same, showing the same ice growth pattern that is also visible in Figure 16a). However, strong differences can be found for the individual tendency terms. When the dynamical term dominates, the dynamical tendency shows overall positive SIC change anomalies over the ice-covered Barents Sea, with a small intensification towards the coasts and a small anomaly of opposing sign south of Svalbard. The thermodynamical tendency term shows the sign-reversed pattern. Outside of the Barents Sea, anomalies are small. This suggests a reduction in local ice formation in favor of other dynamical processes that are not well visible in the winter climatology (Figure 22).

When the thermodynamical contribution is dominant, the patterns are sign-reversed and

much more concentrated towards the coast. Strong positive anomalies in thermodynamical ice production are found along the coasts of Svalbard, Franz Josef Land and Novaya Zemlya and also to some extent in the Barents Sea interior, indicating enhanced local sea ice formation. They are accompanied by negative anomalies in the dynamical term. The opposing-sign anomaly south of Svalbard is also visible, but it is more intense compared to the dynamically-dominated trends. Outside of the Barents Sea, there are strong negative thermodynamical anomalies found along the coast of the Kara Sea. The patterns for thermodynamically-dominated trends compare well to the regression pattern in Figure 23 (with reversed sign), whereas under domination of the dynamical term, the pattern is sign-reversed and exhibits a less pronounced coastal intensification.

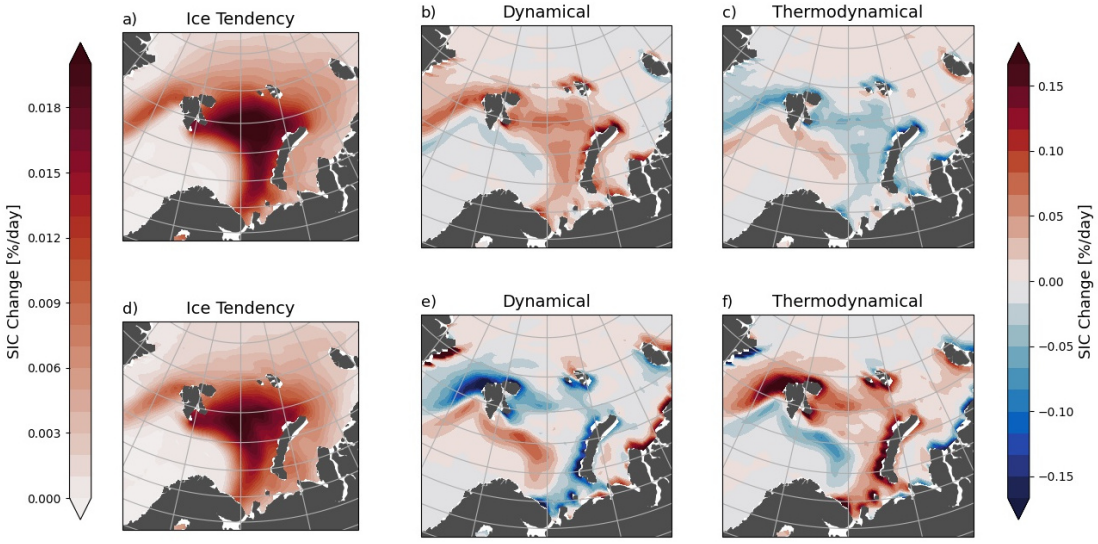

Figure 25: Spatial patterns of the SIC tendency terms averaged over all ice growth events with a dominant dynamical (top) and thermodynamical (bottom) SIA tendency term. Those events where the contribution of a single term exceeds the total tendency term, were considered dominated by the respective tendency term. The colourbar on the left refers to panel a) and d), and the colourbar on the right to panels b), c), e) and f).

The patterns for ice loss events are shown in Figure 26. Also here, the overall tendency is very similar for both categories and resembles that in Figure 16b) well. The individual patterns for dynamically- and thermodynamically-dominated ice loss events compare very well to those of ice growth events, but with the signs of the anomalies reversed: Dynamically-dominated events show negative anomalies in the dynamical component and positive anomalies in the thermodynamical component throughout the Barents Sea, with an intensification towards the coast that is stronger than for ice growth events. The reversed anomaly south of Svalbard is more clearly visible than during dynamically-dominated ice growth events. During events that are thermodynamically-dominated, the ice loss is created by negative anomalies of the thermodynamical tendency and positive anomalies of the dynamical tendency. These anomalies also show an intensification towards the coast, but it is not as pronounced as for ice growth trends and does not differ much from the intensification found for dynamically-dominated ice loss events. The anomalies of opposite sign at the coast of the Kara Sea and south of Svalbard remain present, but the latter is less pronounced compared to ice growth events where

the thermodynamical tendency term is dominant. Once more, the patterns are more similar to the regression in Figure 23, when the thermodynamical term is dominant.

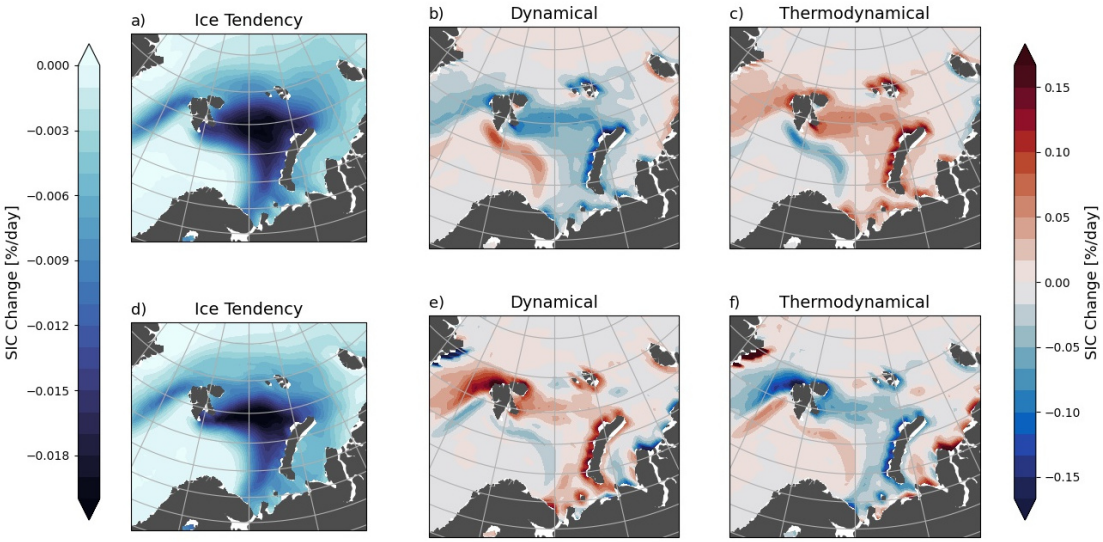

Figure 26: Spatial patterns of the SIC tendency terms averaged over all ice loss events with a dominant dynamical (top) and thermodynamical (bottom) SIA tendency term. Those events where the contribution of a single term exceeds the total tendency term, were considered dominated by the respective tendency term. The colourbar on the left refers to panel a) and d), and the colourbar on the right to panels b), c), e) and f).

4.7 Interdependency of the Drivers

Although ocean heat transport stands out as the most important driver of internal variability of Barents Sea ice area both for interannual variability in general and especially for abrupt changes with a duration of 5-9 years, surface winds also play a large role (Figure 10 and Figure 21). However, the correlation of meridional winds to both OHT (Figure 9) and ice import through the northern section (Figure 12), and its joint forcing with the other drivers of abrupt changes (Figure 21), indicate that the influence of winds is more indirect. Previous studies have also emphasized the influence of atmospheric circulation anomalies on sea ice via ocean heat transport and ice import (Herbaut et al., 2015). In order to disentangle the relationship between ocean heat transport, ice transport, meridional winds and sea ice area, linear regressions between these parameters have been calculated. These linear signals have then be removed from the individual parameters resulting in new, non-correlated timeseries for ocean heat transport (wind-related signal removed), ice transport through the northern gateway (wind-related signal removed) and meridional winds (OHT- and NGW ice transport-related signal removed).

Figure 27 shows the 21-year running correlations between the different variables. When removing the wind-related signal from OHT, the anti-correlation with SIA anomalies drops from -0.7 to -0.5, and reduces more over time to -0.45. Removing the OHT-related signal from the wind reduces its anti-correlation to SIA from -0.4 down to -0.25 at the beginning of the simulations, which decreases further to -0.15 at the end. The time evolution of these signals indicates a reduced decrease of the correlation of SIA and OHT, meaning a smaller reduction when the wind-signal is removed. In contrast, the

decrease in correlation between SIA and winds is enhanced, especially between 2045 and 2055, meaning a larger reduction after the OHT-related part has been removed. This might indicate that a larger part of the reduction in the correlation of both meridional winds and ocean heat transport is associated with meridional winds.

As seen in Figure 12, ice transport through the northern gateway is strongly related to meridional winds. Although removing this linear signal from the winds does not influence its correlation to SIA much (dotted red line in Figure 27), removing the wind-related signal from ice transport across the northern gateway increases its correlation to SIA to overall positive values of up to 0.4, meaning that large SIA is associated with ice stronger export. This suggests ice export via the northern gateway to be a superposition of at least two parts. One part reacts to the wind forcing and pushes sea ice into or out of the Barents Sea, resulting in a negative correlation between SIA and wind-induced ice import that acts as a driver of sea ice area as it was described by Herbaut et al. (2015). This correlation is not very stable since winds are also impacting SIA via the influence on OHT and possibly other processes. The other part is a positive correlation between SIA and ice transport, where the ice transport,which shows an overall export through most of the simulations (Figure 11), simply reacts to sea ice conditions in the Barents Sea, exporting more ice when SIA is large and less when it is small.

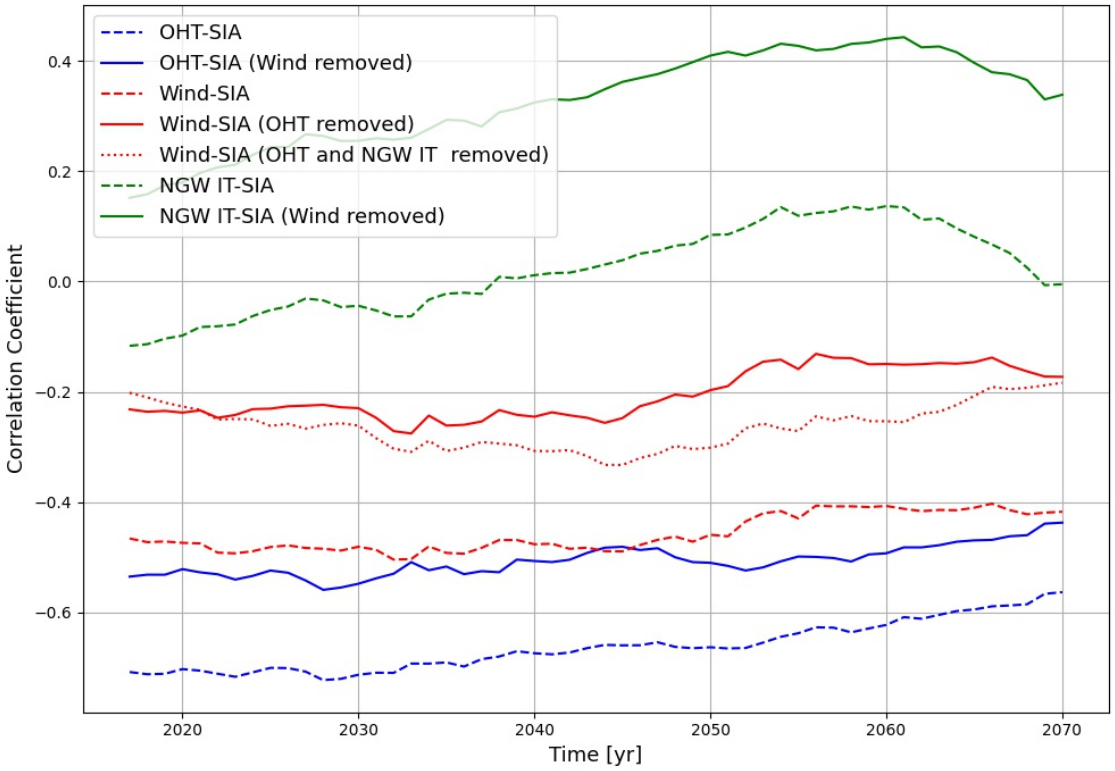

Figure 27: 21-year running correlation of OHT (blue), meridional winds (red) and ice transport (green) to SIA. The dashed lines indicate the correlation of the original time-series, and the solid lines the correlation where the linear influence of one parameter is removed. The red dotted line is the correlation of winds and SIA anomalies after the linear signal related to both, OHT and NGW ice transport has been removed from the winds.

The influence of removing these linearly related signals on the forcing of abrupt change events is shown in Figure 28 and Table 3. By construction, the occurrence of combined forcing is strongly reduced, while individual forcing is found more often. OHT stands out as the most important forcing mechanism (46% of ice growth and 46% of ice loss events can be related to trends in the adapted OHT timeseries), but also trends in the independent signal of meridional winds can still be related to 26% (26%) of the ice growth (loss) events per decade. Ice transport through the northern gateway becomes a less important mechanism, that is contributing mostly at the beginning of the simulation. Overall, removing the linear-related signals clearly decreases the fraction of events that can be related to one of the forcing mechanisms (compare Figure 28 and Table 3 to Figure 21 and Table 2, respectively). The contribution of ice transport through the northern gateway is now clearly confined to the beginning of the simulations, whereas the other forcing mechanism remain at a similar relevance over time.

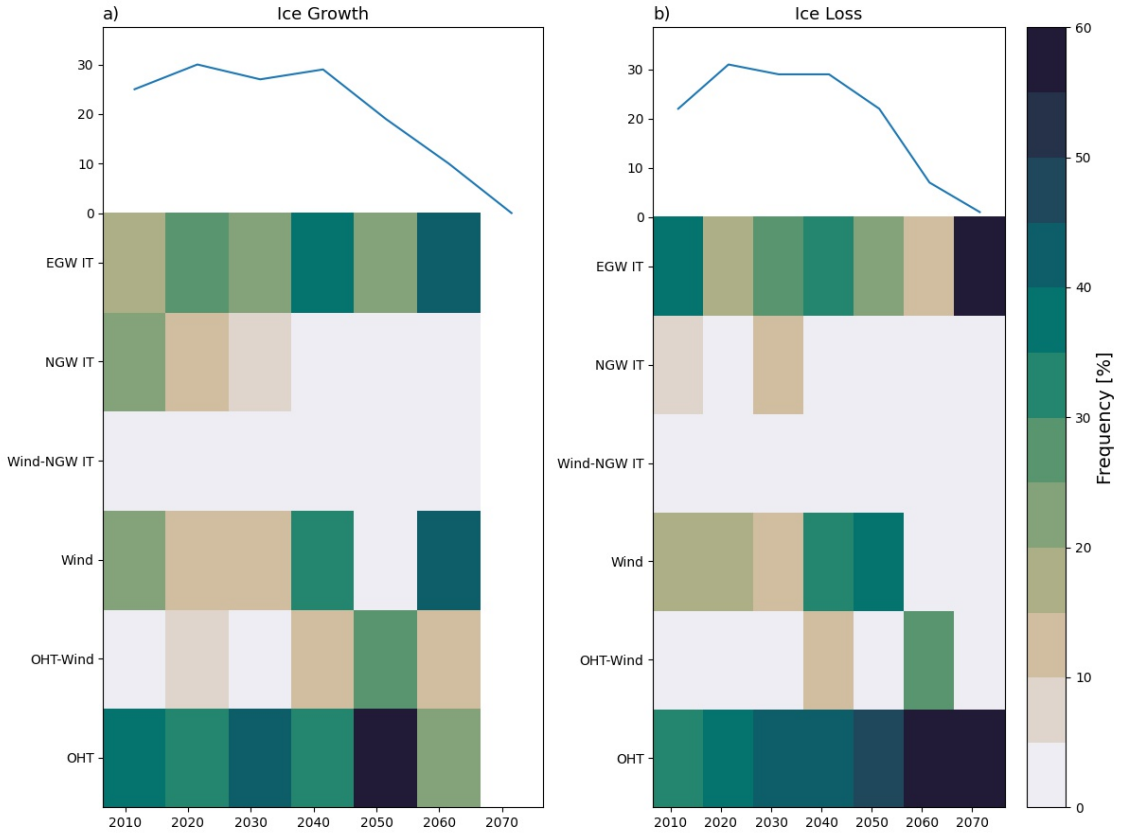

Figure 28: The colour of each field indicates the fraction of ice growth (left) and ice loss (right) events of the particular decade that can be associated with the respective forcing mechanism. The linear wind-related signal has been removed from OHT and NGW ice transport, and the linear OHT- and NGW ice transport-related signal has been removed from the meridional winds prior to analysis. The blue line at the top indicates the total number of events per decade.

Ice Growth

Time Period	07-16	17-26	27-36	37-46	47-56	57-66	67-76	Total
Number of events	25	30	27	29	19	10	0	140
Of these:								
OHT trends	9	11	12	13	17	3	0	65
OHT means	6	3	7	12	6	5	0	39
Wind trends	5	5	5	13	4	5	0	37
Wind means	2	3	4	0	2	2	0	13
NGW IT trends	5	3	2	1	0	0	0	11
NGW IT means	6	5	3	4	5	0	0	23
EGW IT trends	4	8	6	11	4	4	0	37
EGW IT means	7	7	8	8	1	4	0	35

Ice Loss

Time Period	07-16	17-26	27-36	37-46	47-56	57-66	67-76	Total
Number of events	22	31	29	29	22	7	1	141
Of these:								
OHT trends	8	12	13	15	10	6	1	65
OHT means	2	7	6	6	6	1	0	28
Wind trends	5	7	3	12	8	2	0	37
Wind means	4	6	3	6	1	0	0	20
NGW IT trends	2	2	3	0	0	0	0	7
NGW IT means	1	1	8	5	3	4	0	22
EGW IT trends	8	6	8	10	5	1	1	39
EGW IT means	3	12	6	4	1	0	0	26

Table 3: Summary of the number of events identified in Figure 15 that can be associated with trends and means in the four different driving mechanisms after the linear signals that can be related to other parameters have been removed. From OHT the wind-related signal has been removed, from winds the signals related to OHT and NGW ice transport has been removed and from NGW ice transport the wind-related signal has been removed. NGW IT and EGW IT refer to ice transport through the northern and eastern gateway, respectively.

4.8 Sea Ice Area in a Limited Warming Scenario

As the previous sections have indicated, the decrease of winter sea ice area in the Barents Sea also has an impact on the internal variability of the system. To investigate how future greenhouse gas emissions influence the mechanisms of internal variability of sea ice in the Barents Sea, a limited warming run of the CESM will be used (Section 3.1.2). This model run contains 11 simulations from 2006-2100 under the assumption of a concentration pathway that restricts global warming to 2°C compared to the pre-industrial level. This results in a continuation of the global mean temperature rise until 2050 when the increase slows and the temperature reaches a stable level of 16°C (Figure 4). Compared to this, global temperature under the RCP8.5 continues to rise steadily reaching a level of 18°C in 2080. In CESM-LE the annual mean temperature in the Barents Sea increases by

10°C from a pre-industrial -5°C to 5°C in 2080, whereas the limited warming scenario stops the warming in the Barents Sea at an annual mean temperature of 0°C after 2050, which is 5° higher than the pre-industrial value (Figure A.1).

Reducing global warming has a direct impact on the Barents sea ice area. Figure 29 shows the winter sea ice area under the limited warming scenario (blue) compared to the large ensemble under RCP8.5 (red). Under limited warming, SIA is larger from the beginning of the simulations. After a less intense decrease than in the CESM-LE simulations until 2040, the retreat slows down and a new stable level of around $4 * 10^5 \text{km}^2$ is reached in 2050 that the SIA fluctuates around. This is about half of the SIA of the pre-industrial level. The evolution is less smooth as a direct result of the reduced number of ensemble members with 11 compared to 40 in the CESM-LE. Along with this goes a larger variability in the inter-quartile range. Unlike in the CESM-LE simulations, internal variability shows no decline in the limited warming simulations, but remains quite constant at around $\pm 1 * 10^5 \text{km}^2$. The stabilisation of SIA is also visible in the position of the ice edge after 2050 (Figure 30) which is in the central Barents Sea. Adding internal variability onto this results in a large spread of outcomes ranging from an almost ice-free Barents Sea that is similar to the ensemble mean of the CESM-LE 2067-2080 (green line in Figure 30d) to a more southern location of the ice edge than the ensemble mean at the beginning of the simulations (magenta line in Figure 30c,d).

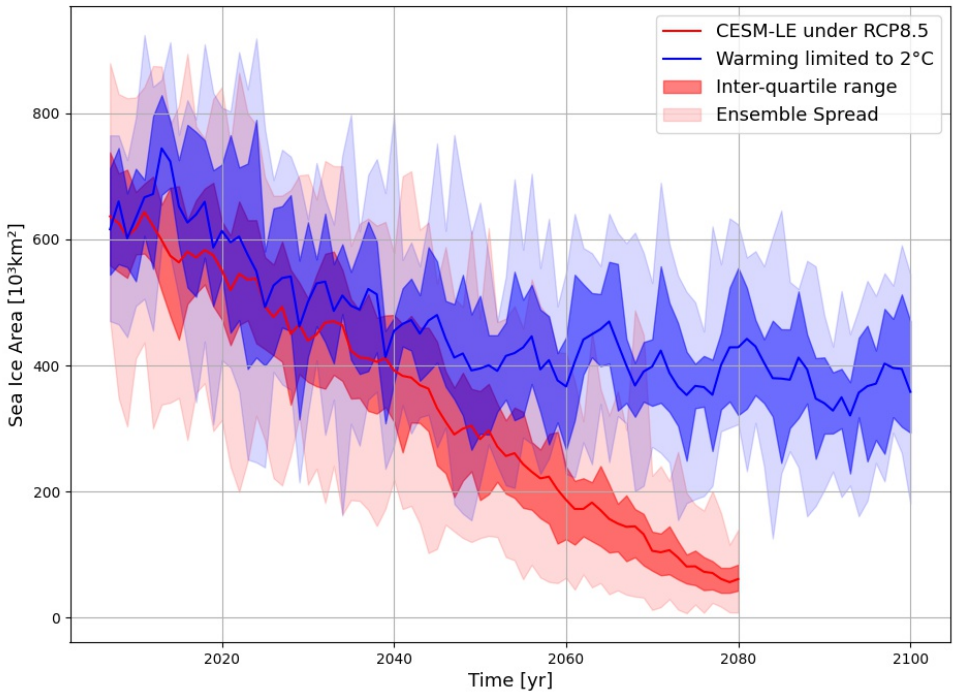

Figure 29: Winter (November-April) sea ice area in the Barents Sea under the limited warming scenario (blue) compared to the large ensemble simulations (red). The solid lines indicate the ensemble mean, the dark shading the inter-quartile range of the ensemble and the light shading the ensemble spread. Note that the amount of ensemble members differs from 40 in CESM-LE to 11 in the low warming simulations.

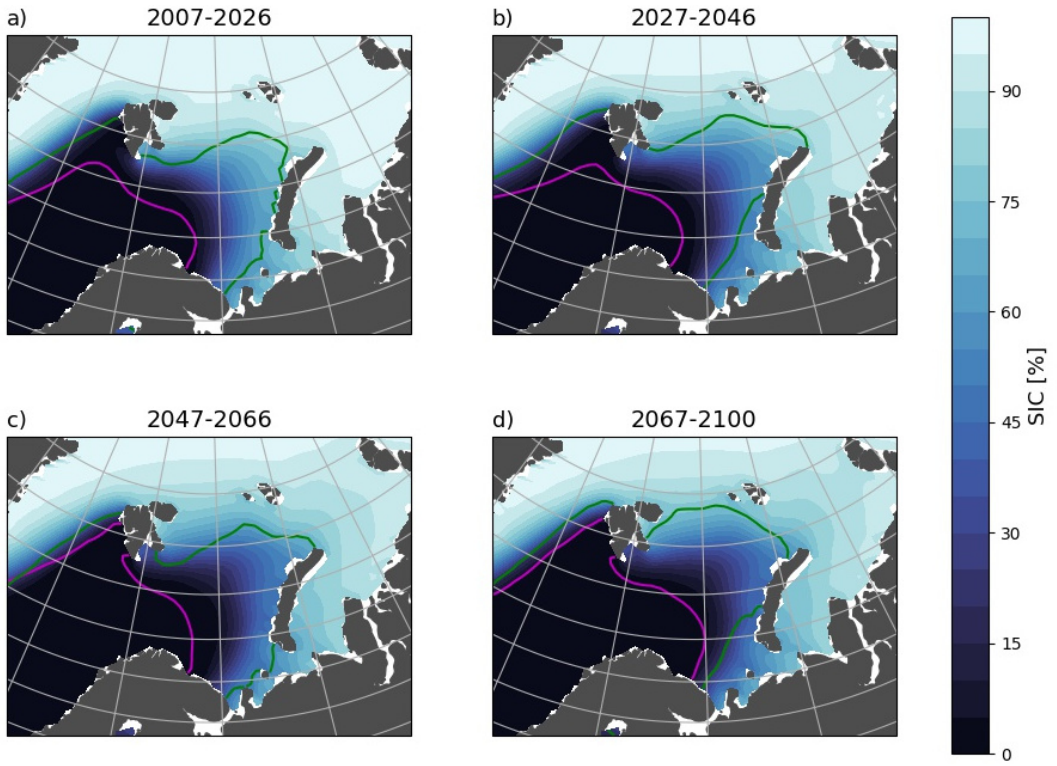

Figure 30: Ensemble mean sea ice concentration during different time periods of the limited warming run. The coloured lines indicate the ice edge (15% SIC) of the year and ensemble member with the largest (magenta) and lowest (green) sea ice area during the respective time period. The northernmost location of the ice edge (green) is given by ensemble member 3 in 2025 (a), member 10 in 2034 (b), member 1 in 2049 (c) and member 11 in 2084 (d). The southernmost location (magenta) is given by ensemble member 6 in 2011 (a), member 4 in 2040 (b), member 5 in 2047 (c) and member 11 in 2071 (d)

4.8.1 Interannual Variability

The internal sea ice variability in the limited warming scenario exhibits a very similar behaviour to the large ensemble simulations under the RCP8.5. A principal component analysis (Section 3.2.8) of sea ice concentration anomalies (Figure A.6) reveals the same modes with a similar amount of explained variability as in Figure 6.

Before looking at the running correlations of sea ice area with the different forcing mechanisms, it is important to note that ocean heat transport shows a smaller increase over time in the limited warming run from 60TW in 2006 to 75TW in 2100. Ice transport via both the eastern and northern gateway does not show the retreat to zero that is visible in CESM-LE (Figure 11), but reaches a stable level of $1.5 * 10^5$km^2/year ice export via NGW and $1.5 * 10^5$km^2/year ice import through EGW after 2050 (Figure A.5).

As in the large ensemble simulations variations in sea ice area are clearly linked to those in ocean heat transport through the Barents Sea Opening. Figure 31a) shows the 21-year running correlation of SIA and OHT anomalies (blue) and wind and OHT anomalies (red). The relation between SIA and OHT is robust amongst all members and only shows a slight drop over time from -0.7 at the beginning to -0.6 at the end. This drop occurs

quite abrupt in the 2030s. The relation to the wind is present at a quite steady level of 0.3 to 0.5, similar to the large ensemble, but with a bit more variability. Analysing the influence of meridional winds (panel b) shows very similar results to Figure 10: A robust anti-correlation among the members with some fluctuations over time, with the average ranging between -0.4 and -0.5. For individual ensemble members the anti-correlation reaches up to -0.7 in the second half of the simulation.

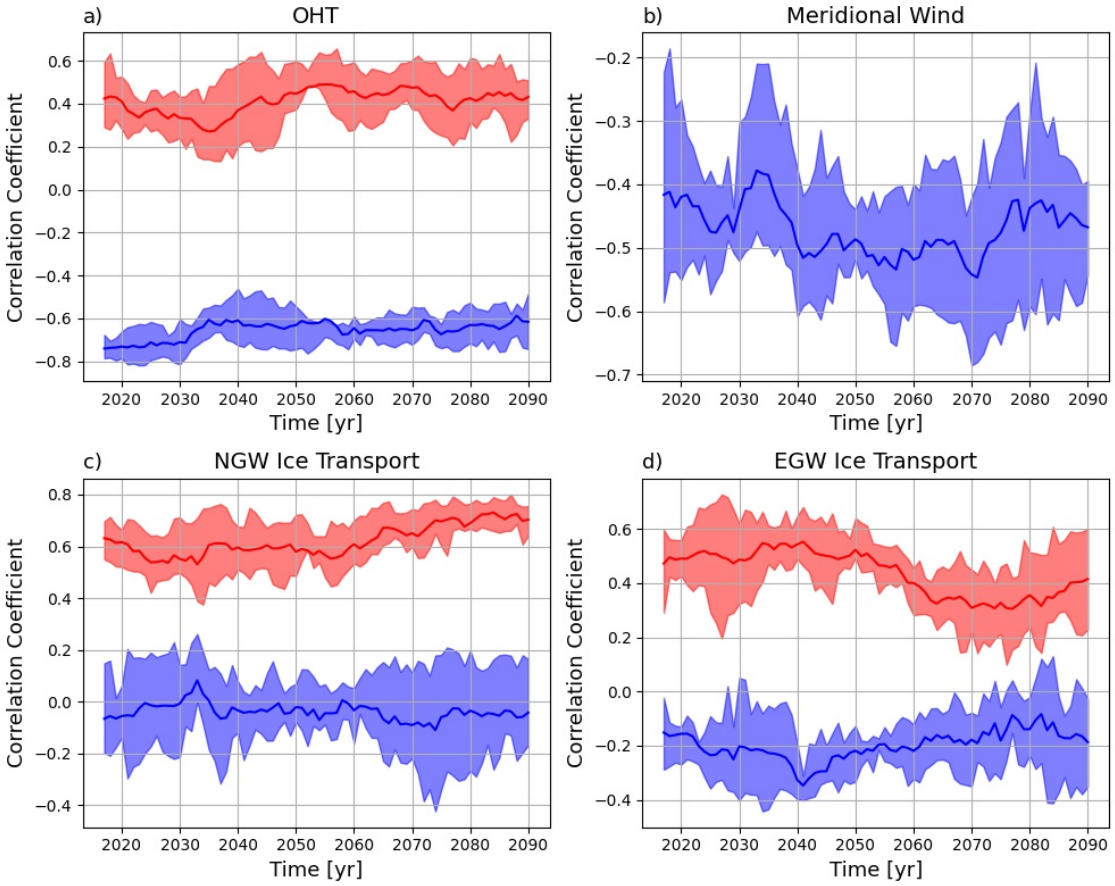

Figure 31: 21-year running correlation between anomalies of ocean heat transport (a), meridional winds (b), northern gateway ice export (c) and eastern gateway ice export (d) to sea ice area anomalies (blue) and meridional wind anomalies (red). The solid lines indicate the average across all ensemble members and the shading the inter-quartile range of the cross-member variability.

The running correlation of SIA anomalies and ice transport through the northern (panel c) and eastern (panel d) gateway exhibits no correlation for the northern gateway and a small anti-correlation of -0.2 to -0.4 for the eastern gateway. Cross-member variability is quite low for both gateways. Despite some fluctuations over time there is no trend visible, which is different from the results of the large ensemble simulations (Figure 12). Ice transport across the northern gateway shows a strong, constant and robust correlation to meridional winds at a similar level as in the large ensemble. Ice transport through the eastern gateway also shows a correlation to meridional winds, but this is dropping in the middle of the 21st century before rising again towards the end. This behaviour is mirrored by the running correlation of SIA and ice transport through EGW and is accompanied by a slight increase in cross-member variability.

4.8.2 Abrupt Changes

Figure 32 shows the distribution of 5-year trends of SIA anomalies in different time periods of the low warming run in blue compared to the large ensemble simulations in grey. For the first half of the simulation (until 2046) the histograms are very similar, with only small differences, probably resulting from the reduced sample size from 40 down to 11 ensemble members. Between 2047 and 2066 (panel c), the histogram of the low warming run remains similar, whereas the large ensemble shows a tendency towards smaller trends, which is continued at the end of the simulations. Also between 2067 and 2100 (panel d) the limited warming run shows a distribution of 5-year trends that is very close to the others, but with only a small decrease of strong trends and more weak trends. This is in clear contrast to the CESM-LE simulations that show almost no strong trends during this time period.

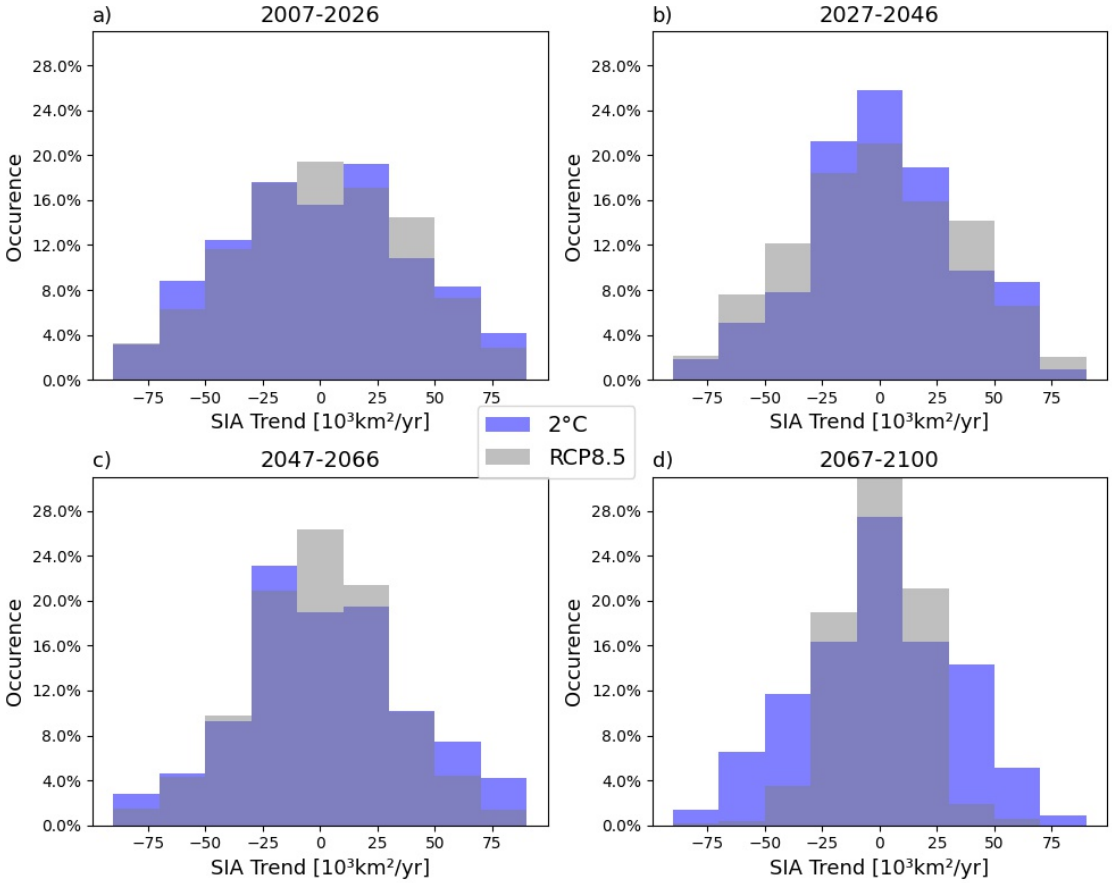

Figure 32: Histogram of 5-year trends of SIA in the low-warming run (blue) and the large ensemble simulation (RCP8.5; grey) after the ensemble mean has been removed, divided into 4 time periods. Note that the large ensemble of panel d) corresponds to the time between 2067-2080, and the largest values are out of the boundaries of the x-axis (see Figure 13 for the exact values)

Similar to the analysis of CESM-LE, events of rapid SIA change were identified in the low warming runs applying the same criterion of a linear trend of $\geq 5 * 10^4 \text{km}^2/\text{year}$ over ≥ 5 years. The results are depicted in Figure 33. A total number of 58 ice growth and 54 ice loss events are found, which gives a number of around 5 events per ensemble

member, which is more than the 3.5 events per member that were found in the large ensemble (the low warming runs also cover a time period of 20 years more than what was analysed for CESM-LE, but this is not enough to explain the full difference in the number of events). These events are almost equally distributed over time (Figure 33). Both ice growth and loss events still occur in the late 21st century, which is in contrast to the large ensemble simulation (Figure 15). The average duration of 6.0 (5.8) years of ice growth (loss) trends and intensity of $5.8 * 10^4$ ($-5.9 * 10^4$) km²/year are very similar to those produced by the large ensemble.

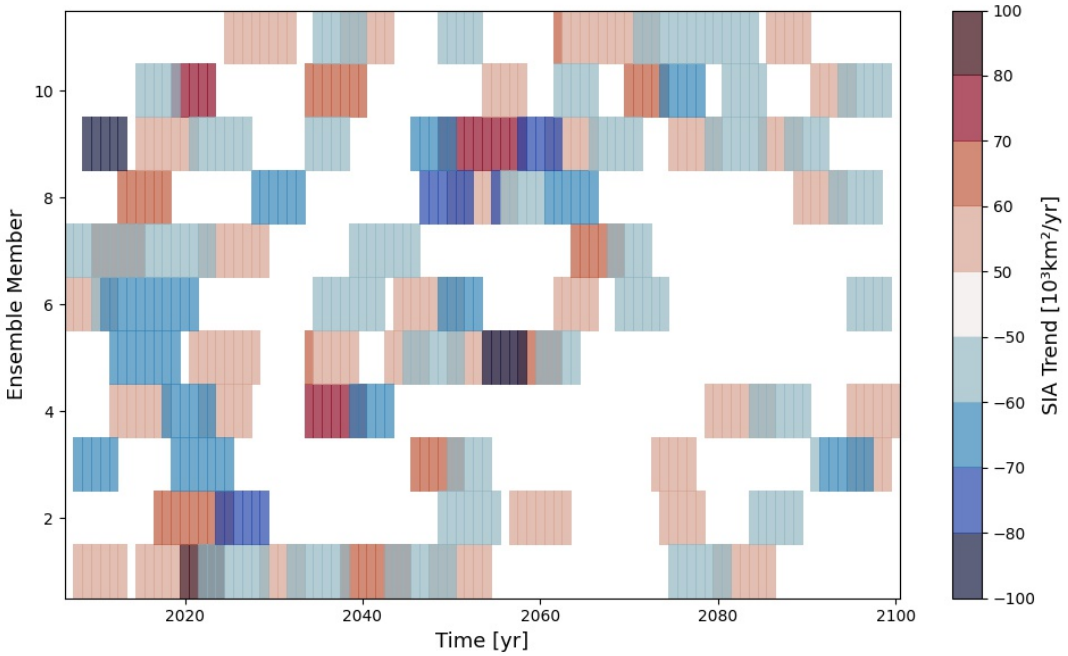

Figure 33: Identification of events of abrupt change in BS SIA in the limited warming runs. As for the large ensemble a criterion of a linear trend of more than $5 * 10^4$km²/year over a duration of at least 5 years was applied, resulting in 58 ice growth and 54 ice loss trends.

Investigating the forcing mechanisms of these events leads to only small differences from the large ensemble simulations. The relative importance of the different driving mechanisms can be seen in Figure 34 and in Table 4 (the individual scatter plots can be found in the appendix from Figure A.7 onwards). Ocean heat transport stands out as the dominant driver of the abrupt changes for both ice loss and ice growth, alone and in combination with meridional winds. Winds also contribute in combination with ice transport through the northern gateway, but not on their own. The same holds for ice transport through the northern gateway. Ice transport through the eastern gateway also has a significant influence, slightly more so for ice growth events. There are no outstanding differences over time and between growth and loss events visible. All these results are very similar to those obtained from the CESM-LE simulations. The largest difference to the large ensemble results is that the number of events remains rather constant over time.

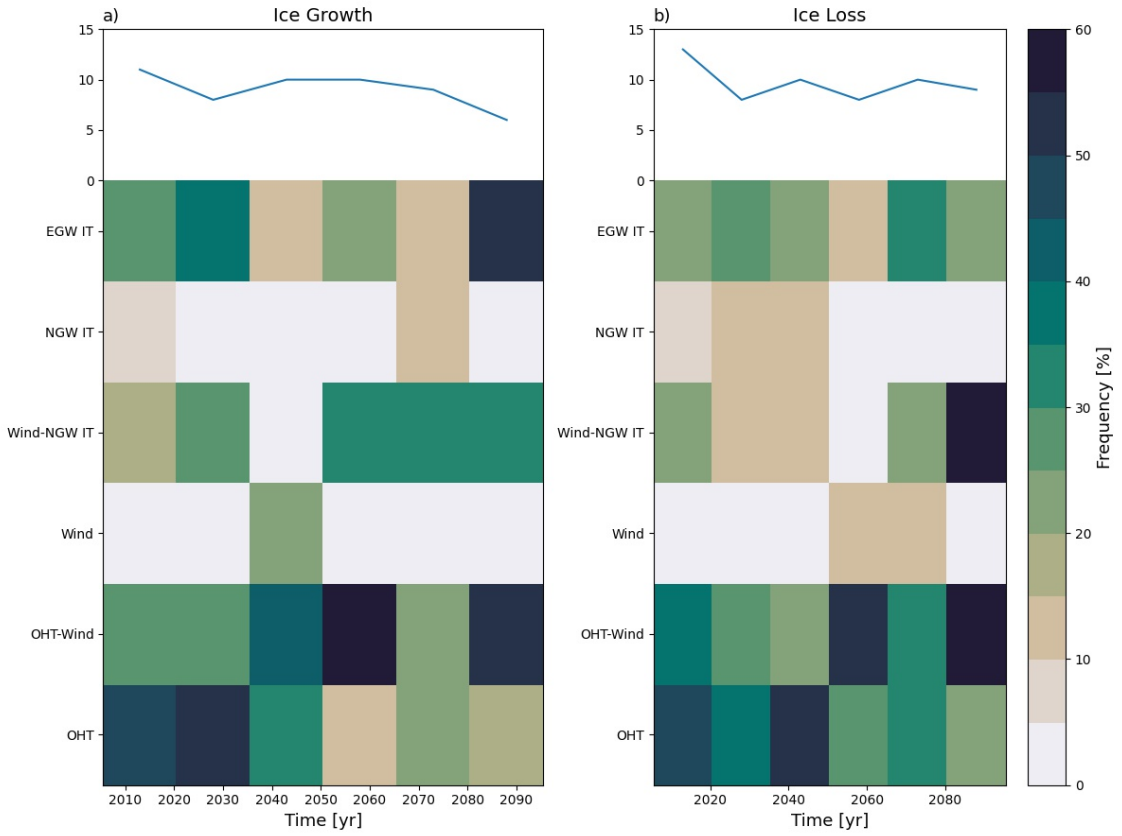

Figure 34: The colour of each field indicates the fraction of ice growth (left) and ice loss (right) events of the particular time period of 15 years that can be associated with the respective forcing mechanism. The blue line at the top indicates the total number of events in each 15-year period.

Ice Growth

Time Period	07-21	22-36	37-51	52-66	67-81	82-00	Total
Number of events	11	8	10	10	9	6	56
Of these:							
OHT trends	8	6	7	7	4	4	36
OHT means	5	1	4	2	3	3	18
Wind trends	4	4	6	8	4	4	30
Wind means	2	3	4	1	6	0	16
NGW IT trends	3	2	0	3	4	2	14
NGW IT means	4	4	2	0	2	0	12
EGW IT trends	3	3	1	2	1	3	13
EGW IT means	4	2	1	3	2	0	12

Ice Loss

Time Period	07-21	22-36	37-51	52-66	67-81	82-00	Total
Number of events	13	8	10	8	10	9	58
Of these:							
OHT trends	11	5	7	6	6	7	42
OHT means	6	0	2	0	2	2	12
Wind trends	6	3	3	5	6	6	29
Wind means	3	3	2	0	1	1	10
NGW IT trends	4	2	2	0	2	5	15
NGW IT means	3	3	2	4	0	0	12
EGW IT trends	3	2	2	1	3	2	13
EGW IT means	0	2	0	2	1	3	8

Table 4: Summary of the number of events identified in Figure 33 that can be associated with trends and means of the four different driving mechanisms. NGW IT and EGW IT refer to ice transport through the northern and eastern gateway, respectively.

5 Discussion

5.1 Sea Ice Conditions in the Barents Sea

Sea ice area (SIA) in the Arctic is declining (Notz and Community, 2020; Årthun et al., 2021). Although this ice loss is most pronounced in summer, large changes also occur in winter, and studies suggest that this will soon take over as the main season of Arctic sea ice loss (Onarheim et al., 2018). A large fraction of the winter sea ice loss can be attributed to the Barents Sea that is ice-free in summer and partly ice-covered in winter (Figure 1). Observations show some variability in sea ice area throughout the 20th century until 1980 that was followed by a strong decline (Figure 2). This decline accelerated after 2004 leading to a minimum sea ice area of $4 * 10^5 \text{km}^2$ in 2017 that is only half of the sea ice area in 1980. Although observational data sources before 1980 are limited and datasets extending back to that time should therefore be treated carefully, the main feature of the evolution of Barents Sea ice area remains reliable as data after 1979 is obtained via satellite remote sensing (Cavalieri et al., 2012). This study uses outputs from the Community Earth System Model Large Ensemble (CESM-LE) to investigate the future evolution of sea ice in the Barents Sea. Historical simulations of the CESM-LE from 1920-2005 show a winter sea ice area that resembles the observations well, which is supportive of its applicability to Barents Sea ice conditions (Figure 2). The model has previously been used to analyse sea ice conditions in the Arctic and the Barents Sea and has been found to perform well (Årthun et al., 2019; England et al., 2019; Labe et al., 2018). Figure 2 shows a slight tendency of the model to simulate a delayed ice loss in the Barents Sea compared to the observations. This is likely due to the cold bias of the CESM (Wang et al., 2014), resulting in too cold conditions in the North Atlantic that leads to a delayed warming. Influences on Barents Sea ice variability should be limited apart from the fact that time evolutions can be expected to take place earlier than the model simulations suggest.

Climate models are in large agreement that this decline in Barents Sea winter sea ice will continue under the current greenhouse gas emissions (in agreement with Onarheim and Årthun, 2017). Using simulations from the CESM-LE, Figure 2 shows a constant decline of sea ice throughout the 21st century leading towards year-round ice-free conditions in the Barents Sea by the end of this century (Onarheim and Årthun, 2017). Although the 40 simulations agree on this decline, the spread of the individual simulations is large (Figure 2). Whereas the common feature of ice loss is related to anthropogenic forcing, the model spread represents internal variability of the climate system (Deser et al., 2014) and demonstrates, both for historical and future simulations, the importance of internal variability for the sea ice conditions in the Barents Sea. This can also be seen in Figure 5: Although a clear retreat of the ice-covered area is visible throughout the simulations, differences between single ensemble members (indicated by the coloured lines that show the ice edge of individual simulations) are large. This variability can enhance or mask the common trend of sea ice loss due to anthropogenic forcing. Whereas some simulations indicate a retreat of the winter ice edge beyond the limits of the Barents Sea by 2080 (green line in Figure 5d), others show an ice edge that is rather close to present day conditions (magenta line in Figure 5d). The focus of this work has thus been to investigate this internal variability and its driving mechanisms under future climate conditions.

5.2 Interannual Variability

An investigation of the interannual variability in the future simulations of the CESM-LE exhibits similar variability patterns to what Efstathiou et al. (2021) found in observations, suggesting that the internal variability remains rather unaffected by the anthropogenic sea ice loss. While the most dominant pattern of variability (Figure 6) represents overall ice changes in the Barents Sea well, also EOF2 and EOF3 (Figure 6) that represent local redistribution of sea ice in the Barents Sea compare well to the findings of Efstathiou et al. (2021). The identification of a net-change-mode that represents total ice change in the Barents Sea is in contrast to the findings of Herbaut et al. (2015) who found the total variability of sea ice area to be split into a northern and an eastern mode who are not significantly correlated. Their findings are based on the observational record between 1979 and 2004, which is likely the reason for these differences. They have argued that a regime change following a rapid decline of sea ice after 2004 could have altered processes in the Barents Sea.

Previous studies suggested a broad range of possible forcing mechanism for sea ice changes in the Barents Sea, including atmospheric circulation (Herbaut et al., 2015), ocean heat transport (Årthun et al., 2012), ocean temperature (Efstathiou et al., 2021) and ice import (Kwok, 2009) that are possible sources of predictability of the ice cover (Schlichtholz, 2011; Nakanowatari et al., 2014) .

Also in the CESM-LE future simulations we find several processes involved in Barents Sea winter sea ice variability. Regressions of sea surface temperature (SST) and sea level pressure (Figure 7) indicate a strong influence of sea surface temperature and atmospheric circulation on sea ice area. The regression of SST on the net-change-mode (Figure 7) suggests a strong relationship between warm temperatures and low ice conditions, consistent with the results of Årthun et al. (2012) and Efstathiou et al. (2021). The SST signal extends into the Nordic Seas which resembles the pathway of the inflowing Atlantic Water, indicating a strong influence of ocean heat transport through the Barents Sea Opening (BSO). The regression of sea level pressure (Figure 7) exhibits a circulation anomaly related to meridional winds over the Barents Sea, consistent with findings from Herbaut et al. (2015). We therefore chose to further analyse the relationship between sea ice area anomalies and ocean heat transport (representing the SST pattern), meridional winds (representing the circulation anomalies) and ice transport through the northern and eastern gateway (Figure 11) as possible driving mechanisms.

Ocean heat transport through BSO has previously been identified by Årthun et al. (2012) to contribute to the location of the ice edge and therefore to be an important driver of interannual variability of sea ice area in observational data. A similar finding is made in this study based on CESM-LE future simulations. Anomalies of ocean heat transport through BSO and Barents Sea SIA are highly anti-correlated at -0.7 (Figure 9), which is in agreement to -0.63 that Årthun et al. (2012) found between 1948 and 2007. Over time, the correlation reduces to -0.6, possibly due to the retreat of the ice edge further away from BSO. Herbaut et al. (2015) have argued that the simultaneous relationship of ocean heat transport and sea ice area likely comes from the atmospheric circulation as a common driver of both processes as distance between BSO and the ice edge corresponds to a travel time of several months. Instead, they suggest that ocean heat transport is more likely to have a lagged influence on sea ice. In this study, we do find a consistent correlation between ocean heat transport and sea ice area anomalies, both simultaneously

and when OHT is leading SIA by one year (Figure A.3). Winter OHT is strongest during the seasonal cycle and represents the interannual variability well, resulting in the large correlation without lag. Towards the end of the simulation, ice decreases and the simultaneous correlation of OHT and SIA reduces slightly. This reduction can also be found when OHT leads by one year, indicating that the increased travel time is not enough to explain this reduction (Figure A.3). To what extent this decrease supports the suggestion of Smedsrud et al. (2013) that other processes might gain relative importance compared to ocean heat transport when it comes to influencing sea ice area under smaller ice conditions, remains speculative and cannot be answered here.

Another governing parameter of sea ice variability is ice transport (Kwok, 2009). As Figure 11 indicates, ice is exported out of the Barents Sea through the northern gateway and imported via the eastern gateway with quite large variability. Whereas results from the eastern gateway are in good agreement to what Lind et al. (2018) found in observational data, strong discrepancies between model and observations are found for the northern gateway. Model results indicate a rather robust export of up to $2*10^5$km^2/year in the ensemble mean for the first half of the 21st century, whereas Lind et al. (2018) found varying ice transport that shows both, ice import and export of a rather small amplitude of $\pm 5 * 10^4$km^2/year between 1979 and 2015.

The eastern gateway shows a small anti-correlation of around -0.2 to SIA that increases towards the end of the simulations up to -0.4 (Figure 12b) which is possibly due to the reduced ice cover being more sensitive to import from the Kara Sea, where ice cover is projected to be larger at the end of the century (Årthun et al., 2021). Ice import acts as a driver here, with larger import leading to larger ice cover in the Barents Sea. These findings are in agreement to what Efstathiou et al. (2021) found in observations and what Herbaut et al. (2015) found for the eastern mode of Barents Sea ice variability.

The northern gateway to the central Arctic exhibits more variability. After a small anti-correlation in the beginning, the correlation changes sign at around 2040 to positive values before returning to zero in 2060 (Figure 12a). Although all correlations are small, this behaviour is quite robust throughout the ensemble members. A change at the same time from average ice export to ice import in the timeseries indicates the underlying reasons being not only coincidence (Figure 11). In fact, ice transport through the northern gateway could be more of a response to ice conditions in the Barents Sea when the correlation is positive (2040-2060) before becoming a driver of ice conditions by importing ice into the Barents Sea with a larger impact on the ice conditions there when the ice cover is low at the end of the simulations. An important role in this process is given to the meridional wind, who is strongly correlated to ice transport through the northern gateway by pushing ice into and out of the Barents Sea, but at the same time being related to other processes in the area that determine the state of the Barents Sea ice cover. This process has been found particularly important in driving the northern mode of sea ice variability that Herbaut et al. (2015) found. A change in atmospheric circulation over the Barents Sea in the future could also contribute to the variable relation between SIA and ice transport (Dörr et al., 2021). However, given that the correlations between ice transport and SIA are low compared to the other drivers, and the overall ice transport differs strongly from observations, ice transport through the northern gateway should be considered of secondary importance in driving SIA variability in the Barents Sea.

The atmospheric pattern that is most directly connected to a net-change of Barents Sea ice area is a dipole in sea level pressure between the Arctic and Russia (Figure 7g) that is associated with southerly winds in the northern Barents Sea and southwesterly winds in the southern Barents Sea during low ice conditions. Correlation between Barents Sea averaged meridional wind anomalies and sea ice area anomalies is robust at -0.4 to -0.5, with some variability throughout the simulations, but lower than the correlation between sea ice area and OHT (Figure 10). A strong influence of surface winds on the sea ice variability in the Barents Sea was previously suggested by Herbaut et al. (2015) who investigated observational data and output from a coupled ocean-sea ice model between 1979 and 2012. They emphasized the influence of surface winds on ice changes in the northern Barents Sea by controlling ice import through the northern gateway, and on ice changes in the eastern Barents Sea by influencing coastal ice production. The pattern of atmospheric circulation that is related to ice import through the northern gateway is accompanied by northeasterly wind anomalies in BSO that would reduce the inflow of Atlantic Water (Ingvaldsen et al., 2004), and could therefore explain the simultaneous correlation between OHT and SIA. An influence of meridional winds via the advection of air temperature anomalies was furthermore suggested by Nakanowatari et al. (2014).

This study supports the finding of meridional winds to be contributing to sea ice variability in several ways. Running correlations show that meridional wind anomalies are not only related to sea ice area anomalies (Figure 10), but also to ocean heat transport (red line in Figure 9) and ice transport (red lines in Figure 12). Whereas the correlation between winds and ice transport reduces, possibly due to a shift in atmospheric circulation (Dörr et al., 2021) or due to amplitude reduction of ice transport, the correlation between winds and sea ice area and ocean heat transport shows little variability over time.

To further disentangle these processes, the linear regressions between the different parameters have been removed and the correlation analysis has been repeated. The results in Figure 27 suggest that a joint forcing of several mechanisms is an important feature of Barents Sea ice variability, as removing the linear relationship to other parameters decreases the correlations. Removing the linear relationship to winds from ocean heat transport decreases the correlation down to -0.5, which is still larger than any other correlation, suggesting that although a part of the correlation between OHT and SIA is related to a wind contribution, OHT stands out as the most important driver of interannual variability of Barents Sea ice area. Without the OHT-related component the correlation of meridional surface winds to SIA drops to -0.2, which leaves only a small contribution of surface winds via ice transport, ice formation and temperature advection. The correlation of NGW ice transport to SIA increases to overall positive values after the linear wind-related signal has been removed. This suggests that ice transport across the northern gateway is a superposition of a wind-driven component and a response to sea ice conditions in the Barents Sea where larger ice cover lead to larger ice export.

Our results are in overall good agreement to the findings of Årthun et al. (2012) and Efstathiou et al. (2021). Ocean heat transport seems to be the most important driver of interannual variability of sea ice that has also a large impact in combination with meridional wind anomalies. The wind anomalies likely also play a role via advection of air as was suggested by Nakanowatari et al. (2014). The strong influence of surface winds via controlling ice transport through the northern gateway that was found by Herbaut et al. (2015) could not be found for future simulations in this study, which is

most likely the result of their distinction between northern and eastern sea ice variability in the Barents Sea that we and Efstathiou et al. (2021) do not find. It should also be kept in mind here that the discrepancy of the simulated ice transport to the observations (Lind et al., 2018) demonstrates a possible source of error when it comes to analysing ice transport through the northern gateway.

Results from the sea ice concentration budget indicate that the most important mechanism of interannual variability of Barents Sea ice area is a reduction or an enhancement of local ice production in winter (Figure 23). Low ice conditions are associated with strong reduced coastal thermodynamical ice formation and ice divergence, whereas the signal in the interior is lower. This change in local ice formation at the coast can be a result of the processes discussed earlier. Several studies have emphasized the importance of ocean heat transport (Årthun et al., 2012) and temperature and salinity of the inflowing Atlantic Water (Efstathiou et al., 2021) in determining the sea ice conditions via the wintertime freezing. Herbaut et al. (2015) also pointed out the influence of surface winds in pushing ice offshore which enhances coastal ice formation for the eastern mode of sea ice variability that they find. The regression of the tendency terms shows no clear signal that could be associated with ice import, indicating that it is rather a secondary process as also the smaller correlations indicate. It remains a future task to more clearly investigate the relationship between thermodynamical and dynamical ice change and the governing parameters for sea ice area variability in the Barents Sea presented in this study.

Using a simple conceptual model, Smedsrud et al. (2013) suggested that a future retreat of the ice cover in the Barents Sea could lead to a gain in relative importance of atmospheric forcing mechanisms compared to ocean heat transport. Although we do find a small reduction in correlation of OHT and SIA (however, possibly for the reason of increased distance between BSO and the ice edge), the correlation of OHT to meridional winds shows a similar decline. A process that does seem to gain importance is import from the Kara Sea via the eastern gateway, but this might be due to the simple reason of reduced ice cover being more sensitive to changes. It is, however, speculative to argue about causes for these reductions as they are fairly small and occur in a time where the Barents Sea is close to what Onarheim and Årthun (2017) define as ice-free, and therefore more sensitive to small changes. Instead, our results rather suggest that up to the point when ice area is so small that the correlations become less reliable, interannual variability and its driving mechanisms are rather unaffected by the overall ice loss.

5.3 Abrupt Changes

Observational data shows a rapid decline in Barents Sea winter sea ice area between 2004 and 2009 (Figure 2). This decline has been assumed to introduce a regime shift in the Barents Sea (Herbaut et al., 2015), and was strong enough to reduce the ice area by almost 50%. Similar events also lead to several years of ice growth in the Barents Sea. Previous work by Holland et al. (2006) investigated Arctic sea ice cover and found that abrupt declines are a common feature of future simulations and often related to rapidly increasing ocean heat transport. A similar finding was made by Auclair and Tremblay (2018). Motivated by this and the peak in the power spectrum (Figure 6b), an analysis of sub-decadal variability in the Barents Sea was conducted in this study. The distribution of 5-year linear trends of sea ice area shows a normal distribution that

narrows over time as the ice decreases (Figure 13). Along with this goes a retreat of the area of largest variability towards the northeast (Figure 14). The tails of the distribution include a substantial frequency of strong trends of more than $5 * 10^4$km²/year during the first three quarters of the simulation period, which is of comparable size to the ice loss event of 2004-2009. This indicates that abrupt changes are also a common feature of sea ice variability in the Barents Sea. The distributions compare well to the one that arises from observational data. The small differences can, in part, be attributed to the limited length of the observational record (97 years compared to 40 times 74 years for the model simulations) and differences in the computation of SIA anomalies (in the simulations that is deviations from the ensemble mean, in the observations it is deviations from a 4th-order polynomial fit following Bonan et al., 2021).

Introducing a criterion (a linear trend of more than $5 * 10^4$km²/year over ≥ 5 years) to identify the most extreme events of abrupt changes in SIA yields 140 ice growth and 141 ice loss events amongst the 40 ensemble members, which translates to 3.5 growth and loss events per member. The strength of these events ($5 - 9 * 10^4$km²/year) is of comparable magnitude to the event between 2004 and 2009 and the duration of 5-9 years compares well to the abrupt ice declines in Arctic sea ice area that were found in future simulations by Holland et al. (2006) and Auclair and Tremblay (2018). Although the sea ice area constantly reduces over time (Figure 2), the distribution of trends changes only slightly until 2065 (Figure 13), and a large amount of abrupt change events can be identified in the middle of the 21st century (Figure 15). This suggests that short-term sea ice variability in the Barents Sea remains nearly as strong as today until a very low ice state is reached, and strong, abrupt changes can occur as late as 2070, even under the RCP8.5 emission pathway when the sea ice area is large compared to the ensemble mean. Using a different climate scenario that limits global warming results in a nearly unchanged distribution of sea ice trends with a duration of a few years (Section 5.4).

Based on the analysis of interannual variability, several driving mechanisms were expected to be at work in forcing the abrupt changes. The analyses of Holland et al. (2006) and Auclair and Tremblay (2018) found most rapid ice declines in the Arctic to be thermodynamically driven, which seems also a likely outcome for the Barents Sea given the dominance of OHT in forcing the overall ice loss (Årthun et al., 2012) and interannual variability (Figure 9). The comparison of the SIA trends with trends in ocean heat transport in Figure 17 does indeed show a strong tendency towards ice growth (loss) being accompanied by a reduction (increase) in OHT. Slightly less robust, but very supportive results are also found for meridional winds (Figure 18), where the anti-correlation that was found in interannual variability also applies to abrupt events. The relationships of SIA trends to trends in ice transport are less clear (Figures 19, 20). Here, the relationship shows both, positive and negative trends of very large amplitudes, exceeding the negative standard deviation at times and the positive standard deviation at others. A possible explanation of this could be the previously discussed switch of ice transport between a forcing and responsive mechanism to ice conditions in the Barents Sea and also its high correlation to the wind. Strong ice import could so lead to an increase in sea ice area in the Barents Sea, but at other times large ice area in the Barents Sea can mean increased ice export out of the Barents Sea. Whereas the investigation of interannual variability mainly suggested this for ice transport through the northern gateway, short-term variability also shows a broad range of relations for the eastern gateway.

The combination of these results (Figure 21) confirms what the analysis of interan-

nual variability in general suggests: A clear distinction into changes forced by ocean, atmosphere and ice import is not reasonable. Instead it is the interaction of different mechanisms that is important for both rapid ice growth and ice loss events. Although OHT stands out as the most important mechanism in governing the abrupt changes, a substantial amount of forcing results from a combination with wind forcing. Winds are of little importance as a direct driver of variability (Figure 28), but contribute significantly in combination with ocean heat transport and ice transport. The importance of the northern gateway is rather small, whereas ice transport through the eastern gateway can be strong enough to result in abrupt changes at times. The indication of a decline in the importance of ocean heat transport that the analysis of interannual variability suggests, is not visible for abrupt changes.

There is little to no difference between ice growth and ice loss events. The frequency, intensity, spatial pattern and forcing mechanisms of both types exhibit only small differences which are more likely to be of statistical rather than physical nature. Changes over the duration of the simulation are also small - except from the decrease of importance of NGW ice transport (Figure 28) - and mostly confined to the last part of the simulations where the number of occurring events decreases due to the reduced ice cover, and the statistical reliability is therefore reduced.

This leads to the conclusion that the driving mechanisms of interannual variability in general and sub-decadal abrupt changes compare well. Ocean heat transport is the most important contributor, and meridional winds play an accompanying role by influencing OHT itself and ice transport. The role of the latter seems not so important for interannual variability, but may contribute significantly for events with a duration limited to a few years. This holds mainly for the eastern gateway, where ice is imported into the Barents Sea, but the influence of the northern gateway might be underestimated due to the biased simulation compared to observations.

To further analyse the driving mechanisms of abrupt sea ice trends, a sea ice concentration budget was calculated. Although the overall ice tendency captures the trends in sea ice area very well (Figure 24), which can be seen as a validation of the method (discrepancies here are mostly due to the linear trend being the result of a least-square fit and the ice tendency term being simple summations), the split into the individual components of dynamical and thermodynamical ice change shows a more complex picture. This supports the previous finding that the short-term events and interannual variability in general cannot be easily distinguished into different forcing mechanisms, but are a result of a combination of the drivers. Unlike Holland et al. (2006) who identified all future abrupt Arctic sea ice declines to be thermodynamically driven, the analysis presented here suggests both dynamical and thermodynamical forcing to be important, with high interdependency of one another. A distinction between events with more dynamically- and thermodynamically-dominated forcing is, however, able to give some further insight. Both types produce patterns that are almost fully sign-reversed, already indicating that these short-term trends can be of very different nature in their mechanisms (Figures 25, 26). Figure 25 suggests that ice growth events with a more dominant thermodynamical (43 (40) ice growth (loss) events) term are based on an intensification of the coastal ice production that is already visible in the climatology (Figure 22). This is the result that also shows up in the regression on PC1 (Figure 23), indicating that this type of ice growth event is a manifestation of the dominant mechanisms of interannual variability - possibly related to OHT and meridional winds - on short timescales. Events

with a dominant dynamical term (67 (75) ice growth (loss) events) on the other hand show a broader intensification of ice convergence throughout the Barents Sea, which might be a result of ice import or more large-scale mechanisms. Those events that are dominated by the dynamical term clearly account for the majority of events. This is a surprising result given that the associated patterns of the individual components are very different (nearly sign-reversed) from the regression patterns in Figure 23. It is even more surprising when one tries to relate these events to ice import that clearly plays a secondary role in overall interannual variability, and might only gain little relevance for abrupt changes in SIA. This emphasizes the need for a more detailed investigation of how the different driving mechanisms investigated earlier manifest in dynamical and thermodynamical ice tendency, and what this means for the abrupt changes that can be dominated by either of the tendency terms.

This analysis shows that abrupt changes are limited to conditions when there is still a certain amount of sea ice left in the Barents Sea (Figure A.2). When sea ice is reduced to very low conditions after 2060 in the large ensemble simulation under RCP8.5, abrupt changes do no longer occur (Figure 15), and if they do they are limited to ensemble members where the sea ice area is large compared to the ensemble mean at that time (Figure A.2). Consequently, the investigation of the forcing mechanisms is also restricted to events when SIA is still large. This can be seen as the reason, why the decrease in the relevance of ocean heat transport that we see towards the end of the large ensemble simulations in Figure 9 and the increase in the relevance of ice transport through the eastern gateway (Figure 12) are not clearly reproduced for the abrupt events.

5.4 Influence of External Forcing

The influence of external forcing on the sea ice variability has been tested by analysing outputs from a simulation of the same model that limits global warming to 2°C. The experiment consists of 11 members and is run from 2006-2100. Although 11 members give a very good amount of data, and hence a good confidence in the distinction between external forcing and internal variability, it is substantially less than the 40 members of the large ensemble. In direct comparison, this will result in more flucutations in the ensemble mean and possibly more variability between the members, which should be kept in mind when interpreting the results and comparing to the large ensemble simulations.

The applied forcing in the limited warming scenario results in a stable global mean temperature from 2050 onwards (Figure 4) and is also reflected in the sea ice area in the Barents Sea that shows a slowing retreat towards a stable level of around $4 * 10^5$km² after 2050 (Figure 29). This indicates that a limitation of global warming results in an immediate limitation of Barents Sea ice loss without time lag or undershoot effects. As a result of this new stable level, variability does not decrease as it is seen when the Barents Sea moves towards ice-free conditions in the large ensemble simulations (Figure 2). It is this stability in the mean sea ice area and the consequently high amplitude of the SIA variability that is responsible for the largest differences from the CESM-LE simulations. Ice transport is also more stable over time than in the CESM-LE simulation, showing a constant import through the eastern and export through the northern gateway (Figure A.5). Ocean heat transport through BSO increases slower (Figure A.5).

Although a reduction in greenhouse gas emissions is able to slow down and eventually

stop the retreat of winter sea ice in the Barents Sea, its influence on internal variability seems small. The identified patterns of internal variability (Figure A.6) remain the same as under RCP8.5, and investigation of the driving mechanisms show once more ocean heat transport to be the most dominant driver (Figure 31). Larger differences regarding the influence of ice transport can be associated directly with the different evolution of these parameters in the two scenarios: Under the RCP8.5 scenario the sea ice retreat is accompanied by a decline in both, northern and eastern gateway ice transport, whereas both remain at a stable level in the limited warming scenario. The fluctuation in relevance of ice transport through NGW, and the increase in relevance of ice transport through EGW in the end of the large ensemble simulations under RCP8.5 (Figure 12) indicate an increase in sensitivity of the Barents Sea ice cover to ice transport. The fact that this is not visible under the limited warming scenario (Figure 31) suggests that the reduction in ice cover is the important mechanism that makes the Barents Sea more sensitive to the surrounding areas and the resulting import of ice from the Central Arctic or Kara Sea, where the ice cover is larger.

Concerning the sub-decadal variability, the histograms of 5-year trends (Figure 32) clearly show the difference that a limitation of greenhouse gas emission has on the Barents Sea: Limiting the sea ice retreat ensures a stable level of variability that enables the occurrence of abrupt change events over the full duration of the simulation. After 2050, when the sea ice area under limited warming fluctuates around $4 * 10^5 \text{km}^2$, the abrupt events identified in Figure 33 can lead to production or loss of more than half of this sea ice, emphasizing the importance of internal variability for the system under a limited warming scenario.

The underlying mechanisms for the abrupt events seem to remain unaffected by the external forcing. It is, however, important to note that this analysis is based on abrupt change events that are limited to conditions when there is still a certain amount of sea ice left in the Barents Sea (Figure A.2). The fact that there is no change in the driving mechanism of these events visible under different climate scenarios is hence not supporting that there are no changes underlying sub-decadal sea ice variability in the system, but rather that those strong events do no longer occur when the sea ice area is too small.

Results from analysing a limited warming run clearly indicate that limiting global warming to 2°C compared to the pre-industrial level not only prevents the Barents Sea from entering ice-free conditions, but it also sustains a substantial amount of internal variability on a level that is very comparable to present. Under such a scenario, internal variability remains strong enough to produce ice conditions where the ice edge is located at similar locations as it is found today, even late in the 21st century. This is an important result that should be kept in mind when planning future activity and exploration of oil in the Barents Sea.

6 Conclusion

Sea ice area in the Barents Sea in winter has experienced an accelerated decline in recent years and is projected to decline further under current greenhouse gas emissions, approaching ice-free conditions by the end of this century. This anthropogenic ice loss is superimposed by strong internal variability on interannual to multidecadal timescales that can enhance or counteract the externally-forced trend. In this study, we analysed future simulations from the Community Earth System Model Large Ensemble to investigate the occurrence, strength and forcing mechanisms of internal sea ice variability in a warming world, with a focus on rapid ice change on sub-decadal timescales.

Ocean heat transport stands out as the most dominant driver of interannual variability, being correlated at -0.7 to sea ice area anomalies. Meridional winds also show a strong correlation to sea ice area (-0.5), but part of this comes from an indirect influence via ocean heat transport and ice import through the northern gateway (between Svalbard and Franz Josef Land). Further influence comes from the import of sea ice from the Kara Sea between Franz Josef Land and Novaya Zemlya (eastern gateway). This influence seems to increase as the sea ice in the Barents Sea retreats to the northeast, increasing the distance from the Barents Sea Opening and reducing the ice formation at the coasts of Novaya Zemlya and Svalbard.

A substantial part of internal variability can be related to abrupt changes in ice cover with a duration of 5-9 years. These events are a common feature of the future climate simulations and can lead to a doubling or 50% reduction of the sea ice area within only a few years. Many of the abrupt events show anomalous trends in ocean heat transport, to some extent combined with trends in meridional winds. Meridional winds also account for a large amount of events in combination with ice transport through the northern gateway, but their direct impact is very low. Another important contribution comes from ice import via the eastern gateway. Results from a sea ice concentration budget indicate that many trends can be related to changes in coastal ice formation, whereas others show changes in the dynamical ice tendency to be dominant. It remains the subject of future work to investigate, how this relates to the different drivers of interannual variability.

Internal sea ice variability remains largely unaffected by the gradual sea ice retreat, in terms of both intensity and driving mechanisms until late in the simulations when sea ice area reaches a very low level. At this point, interannual variability reduces, abrupt ice change events become rare and there is a slight shift in the driving mechanisms, reducing the relevance of ocean heat transport and meridional winds in favour of ice import.

Analysis of a limited warming run of the same model reveals that a reduction of greenhouse gas emissions is capable of stopping the retreat of Barents Sea ice cover. A new stable level of roughly half of the 20th century mean sea ice area would be established which is enough to sustain the internal variability and the occurrence of abrupt sea ice trends at a level close to present climate. In the limited warming simulation the internal variability remains strong enough to produce ice conditions comparable to today. Understanding the occurrence and drivers of future sea ice trends is thus important to achieve skillful predictions of the Barents Sea ice cover under global warming, and for the sustainable management of the Barents Sea and its resources.

References

Aksenov, Y., Bacon, S., Coward, A. C., and Nurser, A. G. (2010). The North Atlantic inflow to the Arctic Ocean: High-resolution model study. *Journal of Marine Systems*, 79(1):1–22.

Arrigo, K. R. and van Dijken, G. L. (2011). Secular trends in Arctic Ocean net primary production. *Journal of Geophysical Research: Oceans*, 116(C9).

Auclair, G. and Tremblay, L. B. (2018). The Role of Ocean Heat Transport in Rapid Sea Ice Declines in the Community Earth System Model Large Ensemble. *Journal of Geophysical Research: Oceans*, 123(12):8941–8957.

Bonan, D. B., Lehner, F., and Holland, M. M. (2021). Partitioning uncertainty in projections of Arctic sea ice. *Environmental Research Letters*, 16(4).

Cavalieri, D. J., Parkinson, C. L., DiGirolamo, N., and Ivanoff, A. (2012). Intersensor Calibration Between F13 SSMI and F17 SSMIS for Global Sea Ice Data Records. *IEEE Geoscience and Remote Sensing Letters*, 9(2):233–236.

Cohen, J., Zhang, X., Francis, J., Jung, T., Kwok, R., Overland, J., Ballinger, T. J., Bhatt, U. S., Chen, H. W., Coumou, D., Feldstein, S., Gu, H., Handorf, D., Henderson, G., Ionita, M., Kretschmer, M., Laliberte, F., Lee, S., Linderholm, H. W., Maslowski, W., Peings, Y., Pfeiffer, K., Rigor, I., Semmler, T., Stroeve, J., Taylor, P. C., Vavrus, S., Vihma, T., Wang, S., Wendisch, M., Wu, Y., and Yoon, J. (2020). Divergent consensuses on Arctic amplification influence on midlatitude severe winter weather. *Nature Climate Change*, 10:20–29.

Craig, A. P., Vertenstein, M., and Jacob, R. (2012). A new flexible coupler for earth system modeling developed for CCSM4 and CESM1. *The International Journal of High Performance Computing Applications*, 26(1):31–42.

Deser, C., Lehner, F., Rodgers, K. B., Ault, T., Delworth, T. L., DiNezio, P. N., Fiore, A., Frankignoul, C., Fyfe, J. C., Horton, D. E., Kay, J. E., Knutti, R., Lovenduski, N. S., Marotzke, J., McKinnon, K. A., Minobe, S., Randerson, J., Screen, J. A., Simpson, I. R., and Ting, M. (2020). Insights from Earth system model initial-condition large ensembles and future prospects. *Nature Climate Change*, 10:277–286.

Deser, C., Phillips, A., Bourdette, V., and Teng, H. (2012). Uncertainty in climate change projections: the role of internal variability. *Climate Dynamics*, 38:527–546.

Deser, C., Phillips, A. S., Alexander, M. A., and Smoliak, B. V. (15 Mar. 2014). Projecting North American Climate over the Next 50 Years: Uncertainty due to Internal Variability. *Journal of Climate*, 27(6):2271 – 2296.

Dommenget, D. and Latif, M. (15 Jan. 2002). A Cautionary Note on the Interpretation of EOFs. *Journal of Climate*, 15(2):216 – 225.

Dörr, J. S., Årthun, M., Eldevik, T., and Madonna, E. (2021). Mechanisms of regional winter sea-ice variability in a warming Arctic. *Journal of Climate. In review.*

Efstathiou, E., Eldevik, T., Årthun, M., and Lind, S. (2021). Spatial patterns, mechanisms and predictability of Barents Sea ice change. *Journal of Climate. In review.*

England, M., Jahn, A., and Polvani, L. (2019). Nonuniform Contribution of Internal Variability to Recent Arctic Sea Ice Loss. *Journal of Climate*, 32(13):4039 – 4053.

Gammelsrød, T., Leikvin, Ø., Lien, V., Budgell, W., Loeng, H., and Maslowski, W. (2009). Mass and heat transports in the NE Barents Sea: Observations and models. *Journal of Marine Systems*, 75:56–69.

Herbaut, C., Houssais, M.-N., Close, S., and Blaizot, A.-C. (2015). Two wind-driven modes of winter sea ice variability in the Barents Sea. *Deep Sea Research Part I: Oceanographic Research Papers*, 106:97 – 115.

Hersbach, H., Bell, B., Berrisford, P., Biavati, G., Horányi, A., Muñoz Sabater, J., Nicolas, J., Peubey, C., Radu, R., Rozum, I., Schepers, D., Simmons, A., Soci, C., Dee, D., and Thépaut, J.-N. (2019). ERA5 monthly averaged data on pressure levels from 1979 to present. *Copernicus Climate Change Service (C3S) Climate Data Store (CDS)*.

Holland, M. M., Bitz, C. M., and Tremblay, B. (2006). Future abrupt reductions in the summer Arctic sea ice. *Geophysical Research Letters*, 33(23).

Holland, P. R. and Kimura, N. (2016). Observed Concentration Budgets of Arctic and Antarctic Sea Ice. *Journal of Climate*, 29(14):5241 – 5249.

Hunke, E. C. and Lipscomb, W. H. (2008). CICE: The Los Alamos sea ice model, documentation and software, version 4.0. *Los Alamos National Laboratory Tech. Rep. LA- CC-06-012*, page 76 pp.

Hurrell, J. W., Holland, M. M., Gent, P. R., Ghan, S., Kay, J. E., Kushner, P. J., Lamarque, J.-F., Large, W. G., Lawrence, D., Lindsay, K., Lipscomb, W. H., Long, M. C., Mahowald, N., Marsh, D. R., Neale, R. B., Rasch, P., Vavrus, S., Vertenstein, M., Bader, D., Collins, W. D., Hack, J. J., Kiehl, J., and Marshall, S. (2013). The Community Earth System Model: A Framework for Collaborative Research. *Bulletin of the American Meteorological Society*, 94(9):1339 – 1360.

Ingvaldsen, R. B., Asplin, L., and Loeng, H. (2004). The seasonal cycle in the Atlantic transport to the Barents Sea during the years 1997–2001. *Continental Shelf Research*, 24(9):1015–1032.

Ivanov, B. V., Gerland, S., Winther, J.-G., and Goodwin, H. (2003). Energy exchange processes in the marginal ice zone of the Barents Sea, Arctic Ocean, during spring 1999. *Journal of Glaciology*, 49(166):415–419.

Jahn, A., Kay, J. E., Holland, M. M., and Hall, D. M. (2016). How predictable is the timing of a summer ice-free Arctic? *Geophysical Research Letters*, 43(17):9113–9120.

Kay, J. E., Deser, C., Phillips, A., Mai, A., Hannay, C., Strand, G., Arblaster, J. M., Bates, S. C., Danabasoglu, G., Edwards, J., Holland, M., Kushner, P., Lamarque, J.-F., Lawrence, D., Lindsay, K., Middleton, A., Munoz, E., Neale, R., Oleson, K., Polvani, L., and Vertenstein, M. (2015). The Community Earth System Model (CESM) Large Ensemble Project: A Community Resource for Studying Climate Change in the Presence of Internal Climate Variability. *Bulletin of the American Meteorological Society*, 96(8):1333 – 1349.

Kwok, R. (2009). Outflow of Arctic Ocean Sea Ice into the Greenland and Barents Seas: 1979–2007. *Journal of Climate*, 22(9):2438 – 2457.

Labe, Z., Magnusdottir, G., and Stern, H. (2018). Variability of Arctic sea ice thickness using PIOMAS and the CESM large ensemble. *Journal of Climate*, 31:3233–3247.

Lamarque, J.-F., Bond, T. C., Eyring, V., Granier, C., Heil, A., Klimont, Z., Lee, D., Liousse, C., Mieville, A., Owen, B., Schultz, M. G., Shindell, D., Smith, S. J., Stehfest, E., Van Aardenne, J., Cooper, O. R., Kainuma, M., Mahowald, N., McConnell, J. R., Naik, V., Riahi, K., and van Vuuren, D. P. (2010). Historical (1850–2000) gridded anthropogenic and biomass burning emissions of reactive gases and aerosols: methodology and application. *Atmospheric Chemistry and Physics*, 10(15):7017–7039.

Laudrum, L. and Holland, M. M. (2020). Extremes become routine in an emerging new Arctic. *Nature Climate Change*, 10:1108–1115.

Lind, S. and Ingvaldsen, R. B. (2012). Variability and impacts of Atlantic Water entering the Barents Sea from the north. *Deep Sea Research Part I: Oceanographic Research Papers*, 62:70–88.

Lind, S., Ingvaldsen, R. B., and Furevik, T. (2018). Arctic warming hotspot in the northern Barents Sea linked to declining sea-ice import. *Nature Climate Change*, 8:634–639.

Liptak, J. and Strong, C. (2014). The Winter Atmospheric Response to Sea Ice Anomalies in the Barents Sea. *Journal of Climate*, 27(2):914 – 924.

Mahajan, S., Zhang, R., and Delworth, T. L. (2011). Impact of the Atlantic Meridional Overturning Circulation (AMOC) on Arctic Surface Air Temperature and Sea Ice Variability. *Journal of Climate*, 24(24):6573–6581.

Mauritzen, C. (1996). Production of dense overflow waters feeding the North Atlantic across the Greenland-Scotland Ridge. Part 1: Evidence for a revised circulation scheme. *Deep Sea Research Part I: Oceanographic Research Papers*, 43(6):769–806.

Mioduszewski, J. R., Vavrus, S., Wang, M., Holland, M., and Landrum, L. (2019). Past and future interannual variability in Arctic sea ice in coupled climate models. *The Cryosphere*, 13(1):113–124.

Nakanowatari, T., Sato, K., and Inoue, J. (2014). Predictability of the Barents Sea Ice in Early Winter: Remote Effects of Oceanic and Atmospheric Thermal Conditions from the North Atlantic. *Journal of Climate*, 27(23):8884 – 8901.

Neale, R. B., Gettelman, A., Park, S., Chen, C.-C., Lauritzen, P. H., Williamson, D. L., Conley, A. J., Kinnison, D., Marsh, D., Smith, A. K., Vitt, F., Garcia, R., Lamarque, J.-F., Mills, M., Tilmes, S., Morrison, H., Cameron-Smith, P., Collins, W. D., Iacono, M. J., Easter, R. C., Liu, X., and Taylor, M. A. (2012). Description of the NCAR Community Atmosphere Model (CAM 5.0). *NCAR Tech. Note TN-486*, page 274 pp.

North, G. R., Bell, T. L., Cahalan, R. F., and Moeng, F. J. (01 Jul. 1982). Sampling Errors in the Estimation of Empirical Orthogonal Functions. *Monthly Weather Review*, 110(7):699 – 706.

Notz, D. and Community, S. (2020). Arctic Sea Ice in CMIP6. *Geophysical Research Letters*, 47(10):e2019GL086749.

Ogawa, F., Keenlyside, N., Gao, Y., Koenigk, T., Yang, S., Suo, L., Wang, T., Gastineau, G., Nakamura, T., Cheung, H. N., Omrani, N.-E., Ukita, J., and Semenov, V. (2018). Evaluating Impacts of Recent Arctic Sea Ice Loss on the Northern Hemisphere Winter Climate Change. *Geophysical Research Letters*, 45(7):3255–3263.

Oleson, K. W., Lawrence, D. M., Bonan, G. B., Flanner, M. G., Kluzek, E., Lawrence, P. J., and Zeng, X. (2010). Technical Description of version 4.0 of the Community Land Model (CLM). *University Corporation for Atmospheric Research.*

Olonscheck, D., Mauritsen, T., and Notz, D. (2019). Arctic sea-ice variability is primarily driven by atmospheric temperature fluctuations. *Nature Geoscience*, 12:430–434.

Onarheim, I. H., Eldevik, T., Smedsrud, L. H., and Stroeve, J. C. (2018). Seasonal and Regional Manifestation of Arctic Sea Ice Loss. *Journal of Climate*, 31(12):4917–4932.

Onarheim, I. H. and Årthun, M. (2017). Toward an ice-free Barents Sea. *Geophysical Research Letters*, 44(16):8387–8395.

Overland, J. E., Hanna, E., Hanssen-Bauer, I., Kim, S. J., Walsh, J. E., Wang, M., Bhatt, U. S., and Thoman, R. L. (2018). Surface Air Temperature [in Arctic Report Card 2018]. https://www.arctic.noaa.gov/Report-Card/Report-Card-2018/ArtMID/7878/ArticleID/783/Surface-Air-Temperature. Accessed: 2021-05-21.

Sanderson, B. M., Xu, Y., Tebaldi, C., Wehner, M., O'Neill, B., Jahn, A., Pendergrass, A. G., Lehner, F., Strand, W. G., Lin, L., Knutti, R., and Lamarque, J. F. (2017). Community climate simulations to assess avoided impacts in 1.5 and 2C futures. *Earth System Dynamics*, 8(3):827–847.

Sandø, A. B., Melsom, A., and Budgell, W. P. (2014). Downscaling IPCC control run and future scenario with focus on the Barents Sea. *Ocean Dynamics*, 64:927–949.

Schlichtholz, P. (2011). Influence of oceanic heat variability on sea ice anomalies in the Nordic Seas. *Geophysical Research Letters*, 38(5).

Serreze, M. C. and Barry, R. G. (2011). Processes and impacts of Arctic amplification: A research synthesis. *Global and Planetary Change*, 77(1):85 – 96.

Skagseth, Ø., Eldevik, T., Årthun, M., Asbjørnsen, H., Lien, V. S., and Smedsrud, L. H. (2020). Reduced efficiency of the Barents Sea cooling machine. *Nature Climate Change*, 10:661–666.

Skagseth, Ø., Furevik, T., Ingvaldsen, R., Loeng, H., Mork, K. A., Orvik, K. A., and Ozhigin, V. (2008). *Volume and Heat Transports to the Arctic Ocean Via the Norwegian and Barents Seas*, pages 45–64. Springer Netherlands, Dordrecht.

Smedsrud, L. H., Esau, I., Ingvaldsen, R. B., Eldevik, T., Haugan, P. M., Li, C., Lien, V. S., Olsen, A., Omar, A. M., Otterå, O. H., Risebrobakken, B., Sandø, A. B., Semenov, V. A., and Sorokina, S. A. (2013). THE ROLE OF THE BARENTS SEA IN THE ARCTIC CLIMATE SYSTEM. *Reviews of Geophysics*, 51(3):415–449.

Smedsrud, L. H., Ingvaldsen, R., Nilsen, J. E. Ø., and Skagseth, Ø. (2010). Heat in the Barents Sea: transport, storage, and surface fluxes. *Ocean Science*, 6(1):219–234.

Smith, R., Jones, P., Briegleb, B., Bryan, F., Danabasoglu, G., Dennis, J., Dukowicz, J., Eden, C., Fox-Kemper, B., Gent, P., Hecht, M., Jayne, S., Jochum, M., Large, W., Lindsay, K., Maltrud, M., Norton, N., Peacock, S., Vertenstein, M., and Yeager, S. (2010). The Parallel Ocean Program (POP) Reference Manual. *Los Alamos National Laboratory Tech. Rep. LAUR-10-01853*, page 141 pp.

Sorokina, S. A. and Esau, I. N. (2011). Meridional energy flux in the Arctic from data of the radiosonde archive IGRA. *Izvestiya, Atmospheric and Oceanic Physics*, 47:572.

Swart, N. C., Fyfe, J. C., Hawkins, E., Kay, J. E., and Jahn, A. (2015). Influence of internal variability on Arctic sea-ice trends. *Nature Climate Change*, 5:86–89.

Sévellec, F., Fedorov, A. V., and Liu, W. (2017). Arctic sea-ice decline weakens the Atlantic Meridional Overturning Circulation. *Nature Climate Change*, 7:604–610.

Taylor, K. E., Stouffer, R. J., and Meehl, G. A. (2012). An Overview of CMIP5 and the Experiment Design. *Bulletin of the American Meteorological Society*, 93(4):485 – 498.

Uotila, P., Holland, P., Vihma, T., Marsland, S., and Kimura, N. (2014). Is realistic Antarctic sea-ice extent in climate models the result of excessive ice drift? *Ocean Modelling*, 79:33–42.

Walsh, J. E., Fetterer, F., Scott Stewart, J., and Chapman, W. L. (2017). A database for depicting Arctic sea ice variations back to 1850. *Geographical Review*, 107(1):89–107.

Wang, C., Zhang, L., Lee, S.-K., Wu, L., and Mechoso, C. R. (2014). A global perspective on CMIP5 climate model biases. *Nature Climate Change*, 4:201–205.

Wang, M. and Overland, J. E. (2009). A sea ice free summer Arctic within 30 years? *Geophysical Research Letters*, 36(7).

Welch, P. (1967). The use of fast Fourier transform for the estimation of power spectra: A method based on time averaging over short, modified periodograms. *IEEE Transactions on Audio and Electroacoustics*, 15(2):70–73.

Woods, C. and Caballero, R. (2016). The Role of Moist Intrusions in Winter Arctic Warming and Sea Ice Decline. *Journal of Climate*, 29(12):4473 – 4485.

Zhang, R. (2015). Mechanisms for low-frequency variability of summer Arctic sea ice extent. *Proceedings of the National Academy of Sciences*, 112(15):4570–4575.

Årthun, M., Eldevik, T., and Smedsrud, L. H. (2019). The Role of Atlantic Heat Transport in Future Arctic Winter Sea Ice Loss. *Journal of Climate*, 32(11):3327–3341.

Årthun, M., Eldevik, T., Smedsrud, L. H., Skagseth, Ø., and Ingvaldsen, R. B. (2012). Quantifying the Influence of Atlantic Heat on Barents Sea Ice Variability and Retreat. *Journal of Climate*, 25:4736–4743.

Årthun, M., Ingvaldsen, R., Smedsrud, L., and Schrum, C. (2011). Dense water formation and circulation in the Barents Sea. *Deep Sea Research Part I: Oceanographic Research Papers*, 58(8):801–817.

Årthun, M., Onarheim, I. H., Dörr, J., and Eldevik, T. (2021). The Seasonal and Regional Transition to an Ice-Free Arctic. *Geophysical Research Letters*, 48(1):e2020GL090825.

Appendices

A Supporting Figures

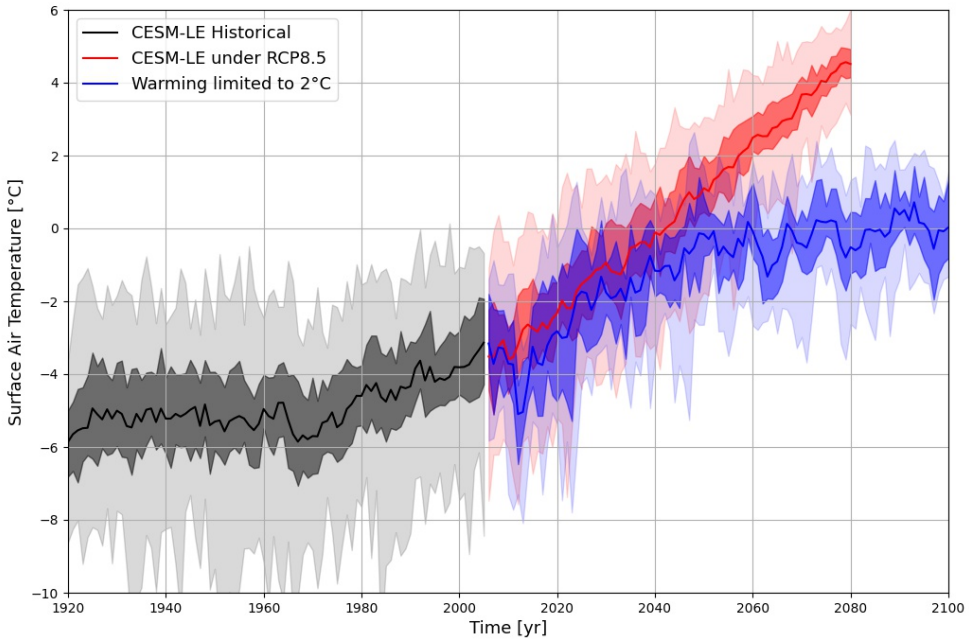

Figure A.1: Mean surface air temperature in the CESM simulations in the Barents Sea. Results for the large ensemble simulation are shown in black (historical) and red (future simulations under RCP8.5). Results from the limited warming simulations are shown in blue. The solid lines indicate the ensemble mean, the dark shading the inter-quartile range of the ensemble and the light shading the ensemble spread. Note that the amount of ensemble members differs from 40 in CESM-LE to 11 in the low warming simulations.

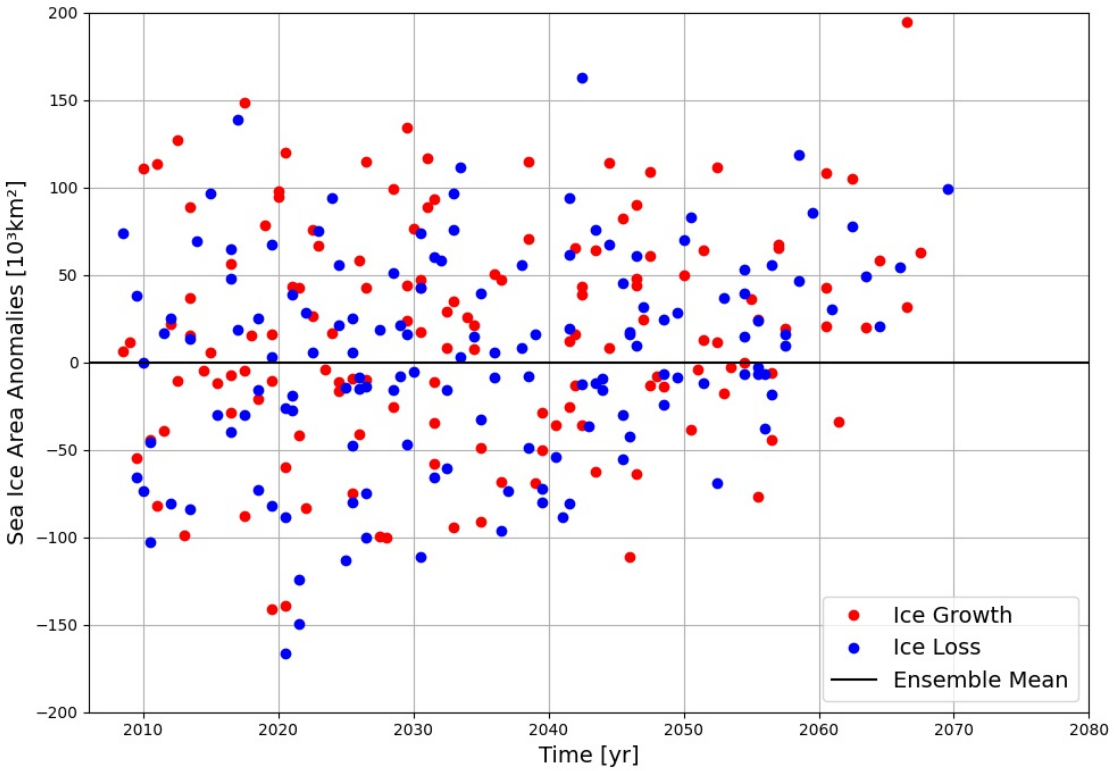

Figure A.2: Average sea ice area anomalies during the events of abrupt ice growth (red) and ice loss (blue) identified in Figure 15. The timing corresponds to the middle of the events.

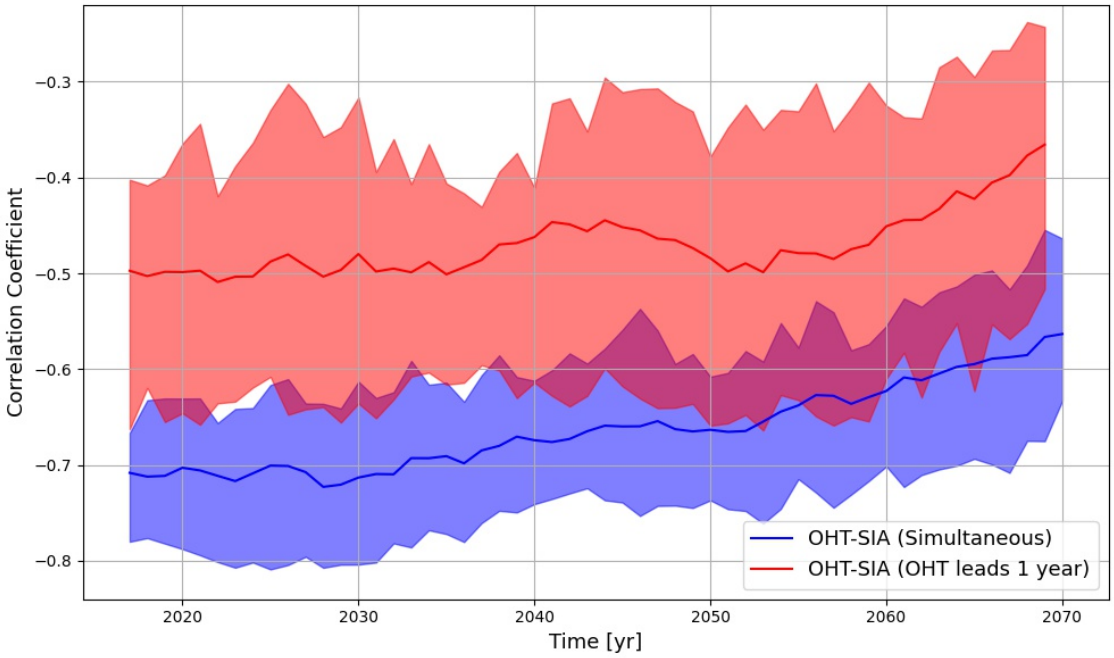

Figure A.3: 21-year running correlation between winter ocean heat transport anomalies and sea ice area anomalies, simultaneously (blue) and when ocean heat transport leads by one year (red). The solid lines indicate the average over all ensemble members and the shading the inter-quartile range.

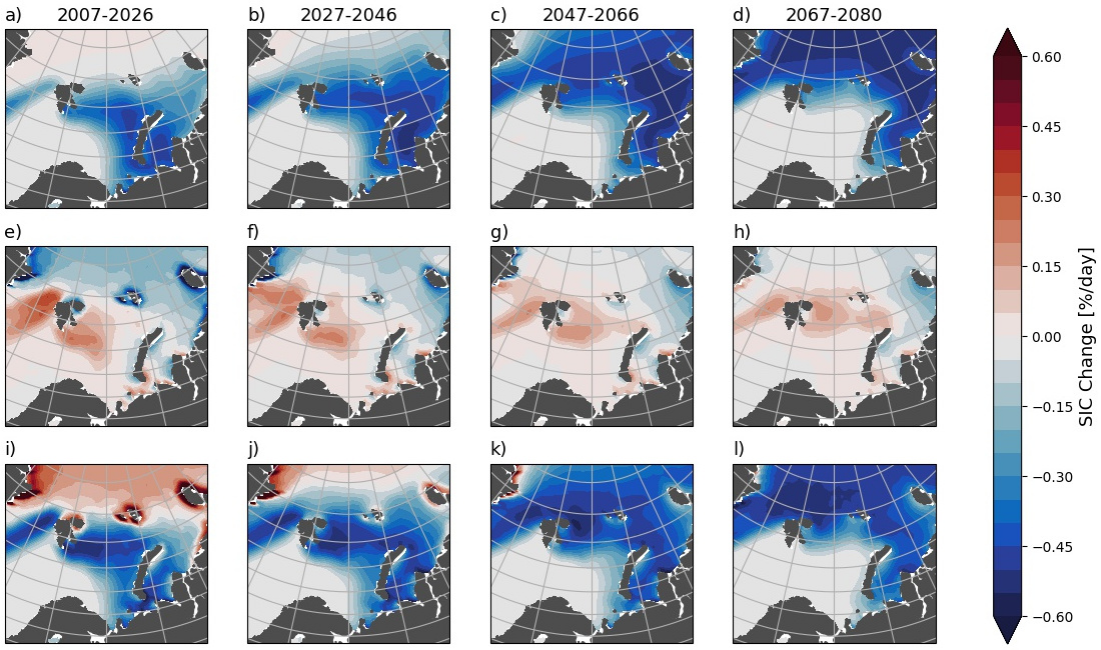

Figure A.4: Summer (May - October) means of total (top), dynamical (middle) and thermodynamical (bottom) ice tendency terms during different parts of the simulation runs. The total ice tendency was calculated as the sum of dynamical and thermodynamical ice change.

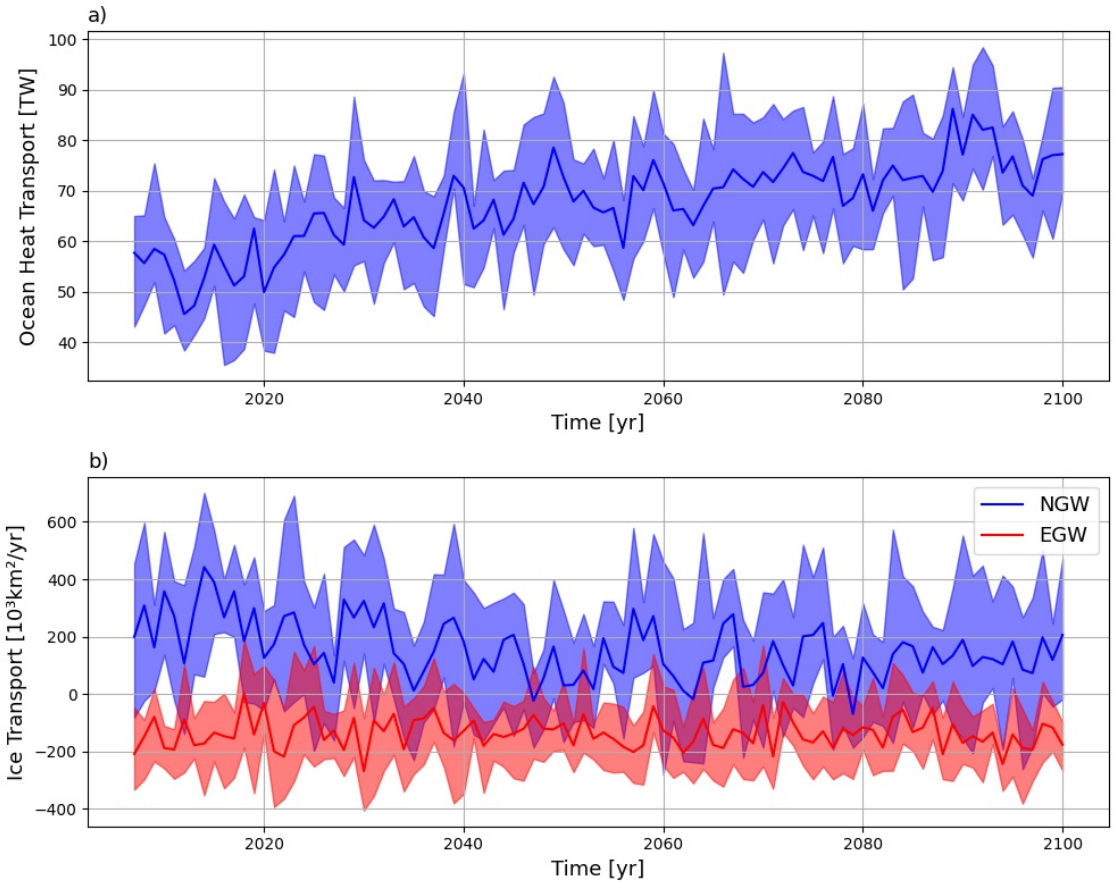

Figure A.5: a): Timeseries of ocean heat transport during the limited warming simulations. The solid line indicates the ensemble mean and the shading the inter-quartile range of the cross-member variability. b): Timeseries of ice transport across the northern (blue) and eastern (red) gateway during the limited warming simulations. Positive values indicate export out of the Barents Sea. The solid line indicates the ensemble mean and the shading the inter-quartile range of the cross-member variability.

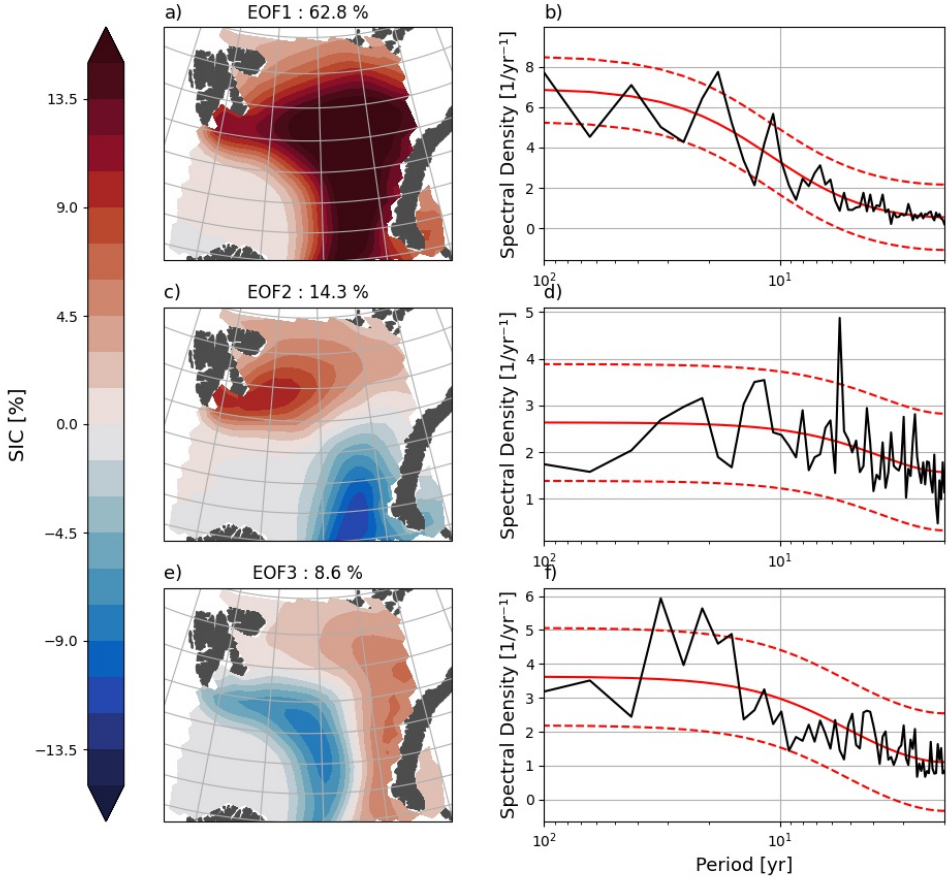

Figure A.6: PCA of SIC anomalies from the limited warming run. The left column shows the 3 most dominant patterns of variability and the right column the corresponding frequency analysis. The red solid line indicates a red spectrum, and the dashed lines the confidence interval of the same. The numbers on top of panel a), c) and e) refer to the amount of interannual variance that is explained by the respective pattern.

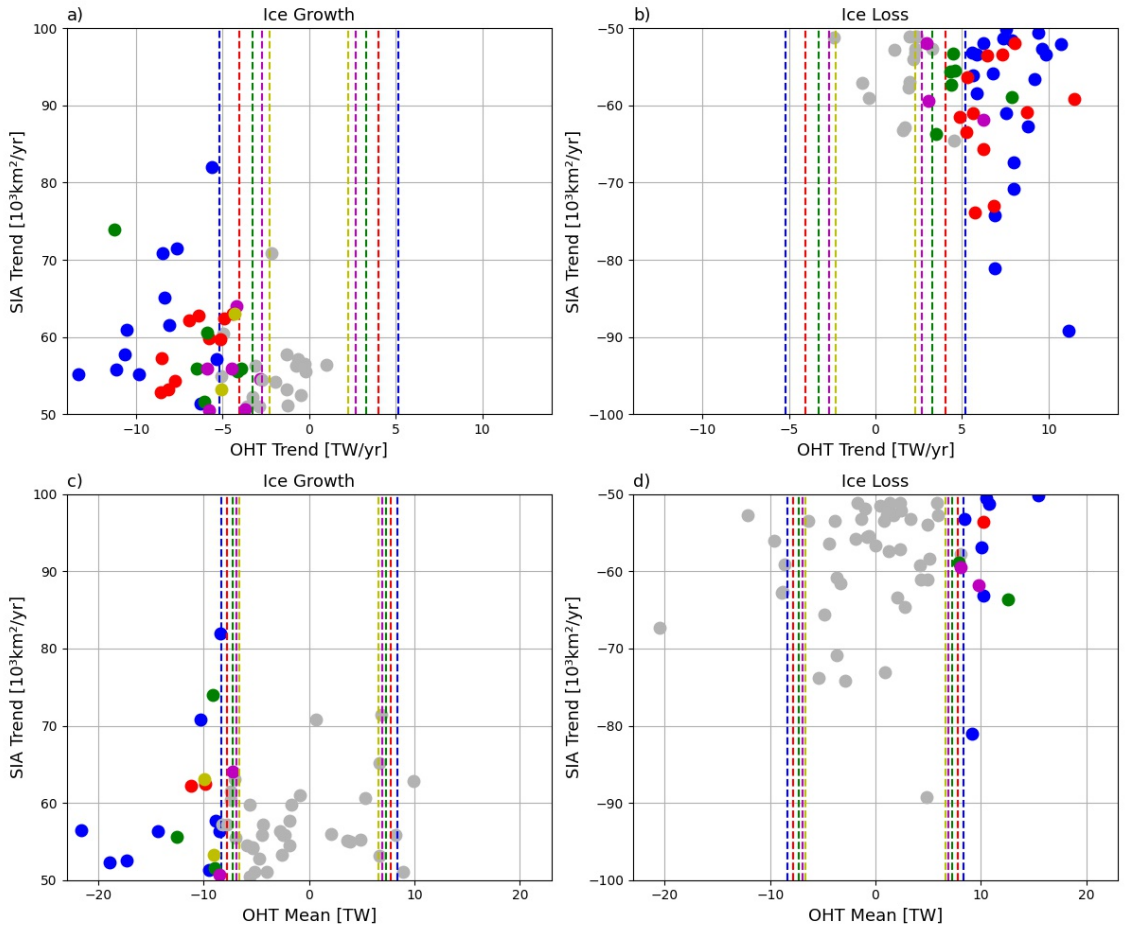

Figure A.7: Trends (top) and means (bottom) of ocean heat transport anomalies during the strong ice growth (left) and ice loss (right) events of SIA anomalies as identified in Figure 33. The dashed lines indicate hereby the standard deviation of trends or means for the respective duration of the events of 5-9 years. Coloured dots indicate trends exceeding this standard deviation, grey dots indicate those that are not exceeding it. The colours correspond to a duration of an event of 5 (blue), 6 (red), 7 (green), 8 (purple) and 9 (yellow) years.

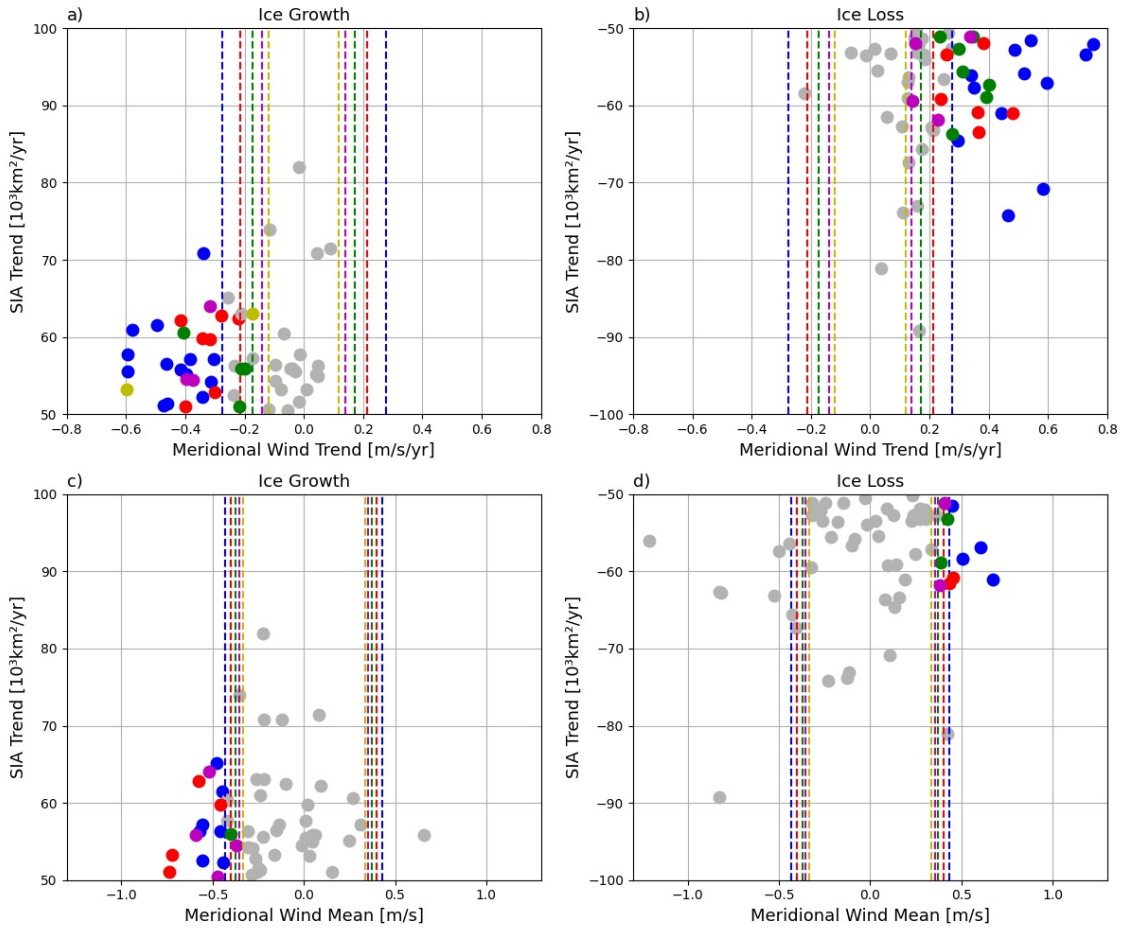

Figure A.8: Trends (top) and means (bottom) of meridional wind anomalies during the strong ice growth (left) and ice loss (right) events of SIA anomalies as identified in Figure 33. The dashed lines indicate hereby the standard deviation of trends or means for the respective duration of the events of 5-9 years. Coloured dots indicate trends exceeding this standard deviation, grey dots indicate those that are not exceeding it. The colours correspond to a duration of an event of 5 (blue), 6 (red), 7 (green), 8 (purple) and 9 (yellow) years.

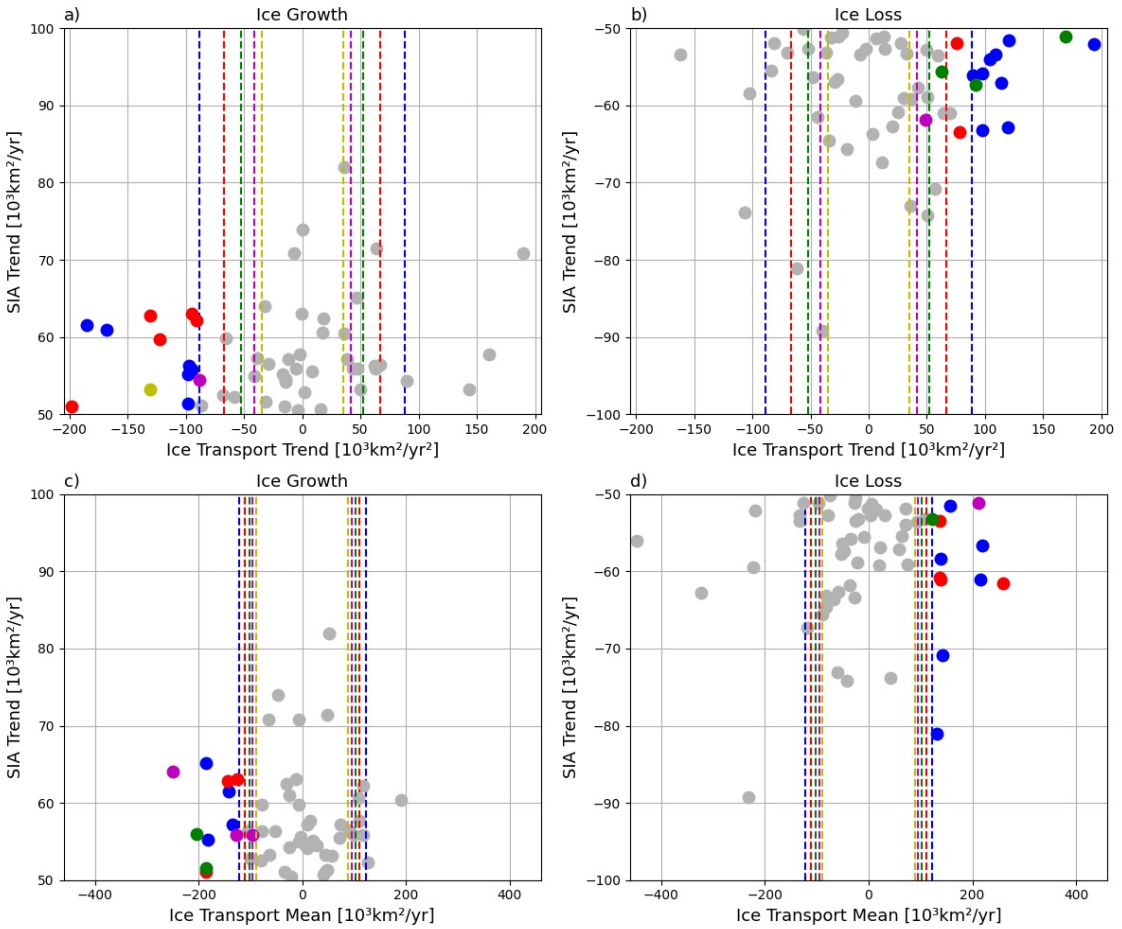

Figure A.9: Trends (top) and means (bottom) of northern gateway ice transport anomalies during the strong ice growth (left) and ice loss (right) events of SIA anomalies as identified in Figure 33. The dashed lines indicate hereby the standard deviation of trends or means for the respective duration of the events of 5-9 years. Coloured dots indicate trends exceeding this standard deviation, grey dots indicate those that are not exceeding it. The colours correspond to a duration of an event of 5 (blue), 6 (red), 7 (green), 8 (purple) and 9 (yellow) years.

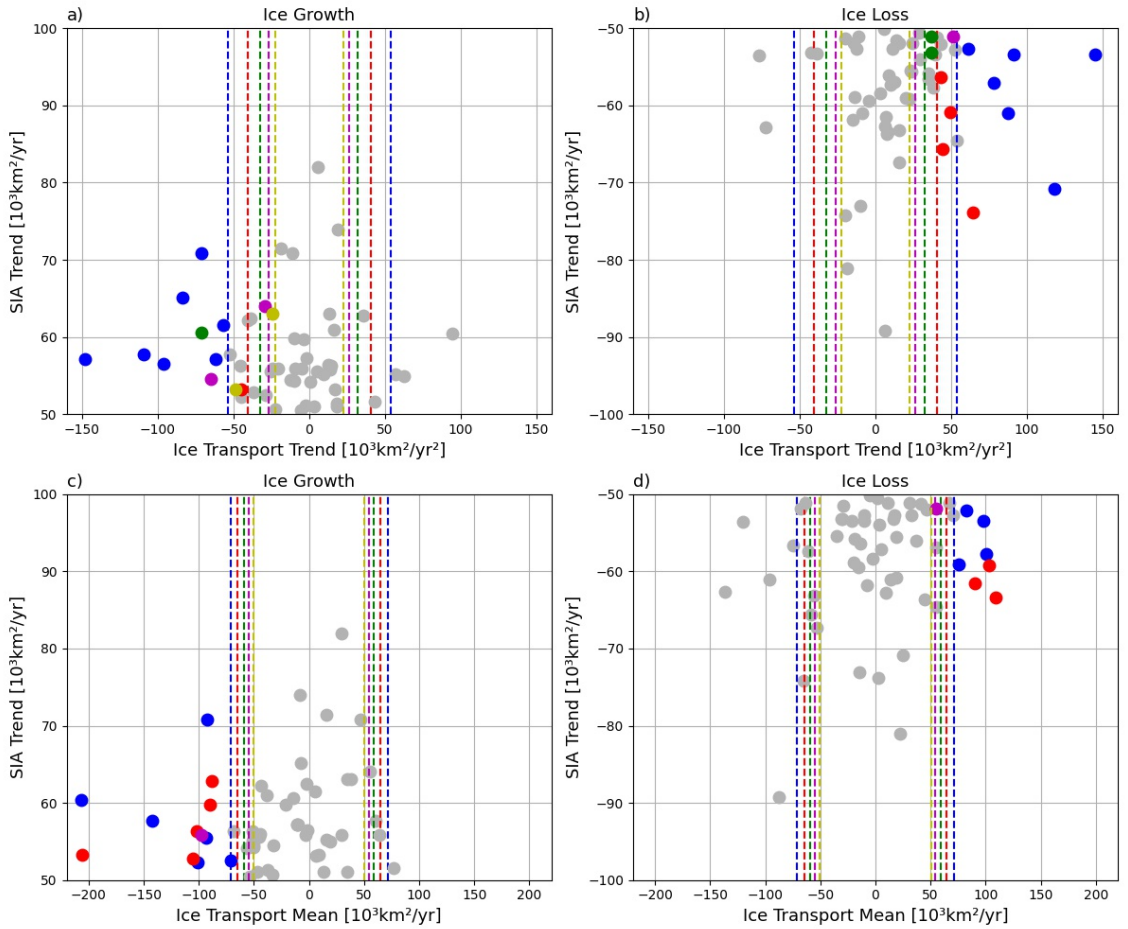

Figure A.10: Trends (top) and means (bottom) of eastern gateway ice transport anomalies during the strong ice growth (left) and ice loss (right) events of SIA anomalies as identified in Figure 33. The dashed lines indicate hereby the standard deviation of trends or means for the respective duration of the events of 5-9 years. Coloured dots indicate trends exceeding this standard deviation, grey dots indicate those that are not exceeding it. The colours correspond to a duration of an event of 5 (blue), 6 (red), 7 (green), 8 (purple) and 9 (yellow) years.

B List of Abbreviations

BS	Barents Sea
BSO	Barents Sea Opening
CESM	Community Earth System Model
CMIP5	Coupled Model Intercomparison Project phase 5
EGW	Eastern Gateway
EOF	Empirical Orthogonal Function
IT	Ice Transport
LE	Large Ensemble
NGW	Northern Gateway
OHT	Ocean Heat Transport
PC	Principal Component
PCA	Principal Component Analysis
RCP	Representative Concentration Pathway
SAT	Surface Air Temperature
SIA	Sea Ice Area
SIC	Sea Ice Concentration
SST	Sea Surface Temperature